Explainable El Niño predictability from climate mode interactions

Sen Zhao[1], Fei-Fei Jin[1,2,*], Malte F. Stuecker[3,2], Philip R. Thompson[3], Jong-Seong Kug[4], Michael J. McPhaden[5], Mark A. Cane[6], Andrew T. Wittenberg[7], Wenju Cai[8,9,10,11]

[1] *Department of Atmospheric Sciences, School of Ocean and Earth Science and Technology (SOEST), University of Hawai'i at Mānoa, HI, USA*

[2] *International Pacific Research Center, SOEST, University of Hawai'i at Mānoa, Honolulu, HI, USA*

[3] *Department of Oceanography, SOEST, University of Hawai'i at Mānoa, Honolulu, HI, USA*

[4] *School of Earth and Environmental Sciences, Seoul National University, Seoul, South Korea*

[5] *National Oceanic and Atmospheric Administration (NOAA)/Pacific Marine Environmental Laboratory, Seattle, WA, USA*

[6] *Lamont Doherty Earth Observatory of Columbia University, Palisades, NY, USA*

[7] *NOAA/OAR/Geophysical Fluid Dynamics Laboratory, Princeton, NJ, USA*

[8] *Frontiers Science Center for Deep Ocean Multispheres and Earth System, Physical Oceanography Laboratory, and Sanya Oceanographic Institution, Ocean University of China, Qingdao, China*

[9] *Laoshan Laboratory, Qingdao, China*

[10] *State Key Laboratory of Loess and Quaternary Geology, Institute of Earth Environment, Chinese Academy of Sciences, Xi'an, China*

[11] *State Key Laboratory of Marine Environmental Science & College of Ocean and Earth Sciences, Xiamen University, Xiamen, China*

*Corresponding author: jff@hawaii.edu

Revised to Nature (04/09/2024)

Summary Paragraph

The El Niño-Southern Oscillation (ENSO) provides most of the global seasonal climate forecast skill[1–3], yet, quantifying the sources of skilful predictions is a long-standing challenge[4–7]. Different sources of predictability affect ENSO evolution, leading to distinct global impacts. Artificial Intelligence (AI) forecasts offer promising advancements but linking their skill to specific physical processes is not yet possible[8–10], limiting our understanding of the dynamics underpinning the advancements. Here we show that an extended nonlinear recharge oscillator (XRO) model exhibits skilful ENSO forecasts at lead-times up to 16-18 months, better than global climate models and comparable to the most skilful AI forecasts. The XRO parsimoniously incorporates the core ENSO dynamics and ENSO's seasonally modulated interactions with other modes of variability in the global oceans. The intrinsic enhancement of ENSO's long-range forecast skill is traceable to the initial conditions of other climate modes via their memory and interactions with ENSO and is quantifiable in terms of these modes' contributions to ENSO amplitude. Reforecasts using the XRO trained on climate model output show that reduced biases in both model ENSO dynamics and in climate mode interactions can lead to more skilful ENSO forecasts. The XRO framework's holistic treatment of ENSO's global multi-timescale interactions highlights promising targets for improving ENSO simulations and forecasts.

Main

The El Niño-Southern Oscillation (ENSO) exerts global environmental and socioeconomic impacts via teleconnections[1–3]. Since the first successful prediction of El Niño in 1986 (ref[4]), decades of progress on the understanding and modelling of ENSO has improved prediction skill[5–7]. However, skilful prediction of ENSO at a lead-time longer than a year remains a challenge.

While ENSO originates from coupled ocean-atmosphere interactions in the tropical Pacific, recent studies highlight that interactions with other ocean basins could potentially improve ENSO prediction[11]. For instance, many other climate modes have been shown to interact with ENSO (Fig. 1a), including the North and South Pacific Meridional Modes (NPMM and SPMM)[12,13]; the Indian Ocean Basin (IOB) mode[14], the Indian Ocean Dipole (IOD) mode[15], and the Southern Indian Ocean Dipole (SIOD) mode[16] in the Indian Ocean; as well as Tropical North Atlantic (TNA) variability[17], the Atlantic Niño (ATL3)[18], and the South Atlantic Subtropical Dipole (SASD) mode[19] in the Atlantic Ocean. Although multiple previous studies designed forecast experiments to illustrate the roles of other ocean basins in ENSO predictability, using simple coupled models[20,21,14], atmosphere-ocean coupled general circulation models (CGCMs)[22–26] or linear inverse models[27,28], it remains a challenge quantifying the relative contributions of other ocean basins to ENSO predictability. The employed CGCMs typically exhibit pronounced biases in simulating both the climate mean state and ENSO dynamics, thus hindering skill in predicting ENSO and complicating quantification of the other ocean basins impact on ENSO predictability. Current linear inverse models are by construction not able to fully capture ENSO's nonlinear dynamics and seasonality[27,28]. Quantifying the sources of skilful predictions from these specific physical processes has been elusive[11,15,17,29,30].

Different sources of ENSO predictability can lead to substantial event-to-event differences in ENSO evolution and associated global impacts. For example, while both the 1997/98 and 2015/16 extreme El Niño events had similar amplitudes of Niño3.4 SST anomalies (SSTAs), they had distinct precursor patterns (Fig. 1b). The 1997/98 event exhibited strong preconditioning via recharged warm water volume (WWV) in the equatorial Pacific, large SST anomaly precursors in the Indian Ocean (including a negative IOD during 1996 September-November (SON)), but only weak SST anomalies in the extratropical Pacific. In contrast, the 2015/16 event was characterized by a weaker build-up of WWV, less pronounced precursor SST anomalies in the Indian Ocean, and instead large amplitude NPMM warming in 2015 March-April-May (MAM). The Atlantic Ocean SST signals are largely similar for the two events, except that the MAM TNA was anomalously warm in 1997 but cold in 2015. In turn, these two events evolved differently in the various basins (Supplementary Fig. 1), which lead to distinct global impacts (Fig. 1c,d, Supplementary Fig. 2, ref[31,32]). These two different evolutions and impacts, affected by varied precursor patterns, underscore the need to quantify the sources of prediction skill and their role in the manifestation of different SST patterns more accurately.

Recent advances have demonstrated the value of AI in predicting ENSO with skilful forecasts at long lead-time of 18-24 months[8–10]. Despite emerging explainable AI methodologies[10], linking the forecast skill of the AI model to specific physical processes is not yet possible, limiting our understanding of the dynamics and physical robustness underpinning the enhanced AI skill. Here we develop a low-order extended nonlinear Recharge Oscillator (XRO) model – which couples the ENSO recharge oscillator with autoregressive model representations for the other modes (see "*Extended Nonlinear Recharge-Oscillator Model (XRO)*" *in Methods*) – to both predict ENSO events and quantify the various sources of ENSO predictability from climate mode interactions. We find that our model provides skilful and, most importantly, explainable forecasts at lead-times up to 16-18 months, better than global climate models and comparable to the most skilful AI ENSO forecast model.

Efficacy boosted by climate interactions

We evaluate the XRO in simulating ENSO through a 43,000 yearlong stochastically forced simulation (See *"Stochastically forced XRO simulations" in Methods*) with parameter estimates derived from 1979-2022 observations (black curves in Extended Data Fig. 1). The XRO accurately simulates the fundamental observed characteristics of ENSO including its seasonal synchronization, Niño3.4 positive skewness, its interannual spectral peak, the 6-9 months lead of WWV over ENSO SST, its irregular interannual oscillations, and the spring persistence barrier (Fig. 2a-d, Supplementary Text 1 and Figs. 3-4). The XRO also accurately reproduces the observed seasonal characteristics of the other climate modes including their seasonal synchronizations and autocorrelations (Supplementary Figs. 5-6). In addition, the XRO realistically simulates the observed lead-lag relationships between ENSO and all the other climate modes with the range of XRO realization cross-correlations encompassing the observations (Fig. 2e-l). Simulating these observed relationships is a major challenge for climate models (Supplementary Fig. 7).

Next, we perform out-of-sample XRO reforecasts by fitting the model for 1950-1999 (50 years) and verifying it independently for the 2002-2022 period (See *"Out-of-sample reforecasts" in Methods*). The correlation skills of the Niño3.4 reforecasts are compared with a nonlinear RO model (nRO), the real-time International Research Institute for Climate and Society (IRI) operational models, and the most skilful AI ENSO forecast model[8,9] (Fig. 2m). Interestingly, the skill of the simple nRO is comparable with the ensemble mean of the IRI statistical models. With mode interactions considered, the XRO outperforms the ensemble mean of the IRI dynamical models at long lead-time (>9 months) with skill scores comparable to the AI model. We also test the model by verifying the early period (1950-1970) and the middle period (1972-1992) independently. The XRO outperforms the nRO regardless which of the verification periods is used to assess the skill (Extended Data Fig. 2), suggesting the importance of mode interactions for ENSO forecast skill regardless of the intrinsic decadal changes in ENSO predictability[33,34].

To get sufficient sample sizes of ENSO events, we next focus on the satellite era (1979-2022) and perform in-sample control reforecasts using the XRO and nRO (denoted as XRO and nRO in the figures, respectively, see *"Control XRO and nRO reforecasts" in Methods*). The nRO ranks in the middle of the skill range for the existing state-of-the-art dynamical prediction systems (Fig.

2n). The XRO systematically outperforms the individual dynamical models and multi-model ensemble mean. The correlation skill of XRO is still above 0.5 at a lead-time of 18 months, which is again comparable to the most skilful AI model (Fig. 2n). We also employ two additional approaches to confirm the robustness of the XRO parameter fitting and reforecasting performance during 1979-2022 (See *"Cross-validated reforecasts" and "Large ensemble simulations and perfect model reforecasting experiments" in Methods,* Supplementary Fig. 8). First, the XRO cross-validated by sequentially leaving *n*-year data out still provides skilful prediction of Niño3.4 SSTA up to 17 months in advance and is insensitive to the exclusion of a range between 2 to 7 years of data (Supplementary Fig. 8a). Second, the XRO was repeatedly trained using each member of large ensemble CGCM simulations (LENS) and forecasted on the same member ("Same-Member" experiment) and an independent realization ("Cross-Member" experiment), respectively. All four LENS models' perfect experiments using the same observational record length (43-year) demonstrate the uncertainty in parameter estimation leads to XRO reforecasting correlation skill error of less than 0.1 within 21 lead months (Supplementary Fig. 8b-d).

We further assess the seasonality of the Niño3.4 forecast correlation skill during 1979-2022 in Fig. 2o-p and Supplementary Fig. 9. Like most of the dynamical models, the nRO exhibits a pronounced spring predictability barrier (SPB) in May-June-July, when the forecast skill decreases rapidly (vertical blue lines in Fig. 2o). The SPB is much less pronounced in the XRO model, which maintains a 0.5 correlation skill up to 16 months for all different initial times (Fig. 2p). The superior efficacy of XRO in ENSO forecasting is further illustrated by the root mean square error metric (Supplementary Fig. 10).

Sources outside the tropical Pacific

The XRO formulation allows us to explicitly isolate and quantify the roles of different mode interactions in ENSO's dynamical behaviour and predictability. Three previous approaches have been employed to assess the impact of climate variability in various ocean basins on ENSO predictability, using CGCMs, intermediate complexity models, and/or conceptual models. They include: (i) *partial initialization* experiments, which set the ocean initial conditions for a specific basin to the model climatology, while using the observed initial conditions everywhere else[21,28]; (ii) *partially coupled* experiments, which apply strong SST restoring toward the model climatology in a specific region during the model integration, while keeping the atmosphere and ocean fully coupled elsewhere[22,24,28]; (iii) *relaxing towards observations* experiments, in which model SSTAs are strongly nudged towards observations in a specific region, while elsewhere the model is fully coupled[23,26]. We apply these strategies to our XRO model in corresponding sets of ENSO reforecasting sensitivity experiments: (i) uninitialized experiments (referred to as U_j), (ii) decoupled experiments (D_j), and (iii) relaxation towards observations experiments (R_j), (see *"Quantitative reforecasting experiments" in Methods* and Extended Data Table 1). We further investigate the total contribution of *all* the modes in each ocean basin to ENSO's predictability by grouping modes together: the extratropical Pacific Ocean (ExPO) includes NPMM and SPMM; the Indian Ocean (IO) IOB, IOD, and SIOD; and the Atlantic Ocean (AO) TNA, ATL3, and SASD. The ExPO+IO+AO experiments demonstrate the combined effects of all the non-ENSO modes.

All the sensitivity experiments qualitatively indicate that coupling information from the ExPO, IO, and AO basins enhances ENSO forecast skill (Fig. 3a), consistent with previous findings[23,24,26,28,35]. However, only the uninitialized experiment framework is a suitable approach to quantify the nearly additive relative contributions of each basin to ENSO forecast skill (Extended Data Fig. 3a,d,e) without artificially overestimating the contribution of climate variability in other basins to ENSO predictability (Extended Data Fig. 3b,c,d,e). Therefore, hereafter we use the uninitialized experiment framework to quantify the impact of each individual basin's or mode's initial condition on subsequent ENSO forecast skill.

Allowing for climate mode interactions enhances ENSO forecast skill, and significantly weakens the SPB with an improvement of correlation skill up to 0.2 ($P<0.08$, Fig. 3b). The enhancement of ENSO forecast skill from climate mode interactions is primarily through the initial condition memory of the different climate modes, demonstrated by the large difference between control and the uninitialized ExPO+IO+AO experiment (Fig. 3c, Supplementary Fig. 11a). The initial states of the other modes can persist for a few months and effectively impact ENSO in specific seasons. In contrast, as evidenced by the minor differences between uninitialized ExPO+IO+AO experiment and decoupled ExPO+IO+AO experiment, the coupled feedbacks with these modes induced by ENSO's initial state only slightly reinforce and accelerate phase-transition of ENSO events (Supplementary Fig. 11b). This results in an increase in forecast skill during the ENSO transition phase (Jun^{+1}-Sep^{+1} targets, Fig. 3d) but a decrease in forecast skill during the ENSO peak phases (Nov^{+1}-Mar^{+1} targets, Fig. 3d). Additional reforecasting experiments (See *"Losing memory experiments" in Methods*, Extended Data Fig. 4) confirm that gradually preserving the initial condition memory of climate modes outside the equatorial Pacific incrementally improves ENSO forecast skill from that of the nRO to that of the XRO.

We further illuminate the roles of individual basins in ENSO predictability by comparing the difference between the control and uninitialized experiments for the ExPO, IO, and AO basin experiments (Figs. 3e-g). The contributions of each basin have strong seasonality. For instance, the effect of ExPO initialization is most pronounced when forecasts start from November-June, and target December-March when the ENSO signal is large (Fig. 3e). This effect is dominated by the NPMM initialization, whereas the SPMM initialization is less impactful (Extended Data Fig. 5a-b). In contrast, the effect of IO initialization is most pronounced when forecasts start from July-November, the time of the year when the IOD develops and peaks (Fig. 3f). The IO effect is dominated by the IOD, with a secondary contribution from the IOB, and the SIOD playing only a minor role (Extended Data Fig. 5c-e). This result is in contrast with the previous finding based on the decoupled linear inverse model experiments[14] which suggested that the IOB plays a more significant role than the IOD in weakening the ENSO SPB. The discrepancy may stem from the lack of seasonality and nonlinearity in their model, along with potential overestimations arising from their decoupled model experiment strategy. The AO also results in a weakening of the ENSO SPB when forecasts are initialized from December-April (Fig. 3g), with major contributions from the TNA and SASD, while Atlantic Niño initialization has a negligible effect (Extended Data Fig. 5f-h). These contributions of mode interactions to ENSO forecast skill are further supported by the root mean square error metric (Supplementary Fig. 12).

ENSO intensification from remote sources

Next, we quantify the roles of mode interactions on the individual ENSO event reforecasts, illustrated by the time series of predicted Niño3.4 SSTAs for the XRO, decoupled ExPO+IO+AO ($D_{\mathrm{ExPO+IO+AO}}$), and uninitialized ExPO+IO+AO ($U_{\mathrm{ExPO+IO+AO}}$) experiments at lead-time of 0-21 months (Fig. 4a-c). The zero lead-time refers to the observed values. The Niño3.4 forecasts in the $U_{\mathrm{ExPO+IO+AO}}$ experiment closely resemble those of the $D_{\mathrm{ExPO+IO+AO}}$ experiment, again indicating that the skill improvement in the control XRO arises from the memory of the other climate mode initializations. These two sensitivity reforecasts can predict the El Niño and La Niña event occurrences at lead-time of 3-9 months and usually underestimate the amplitude of Niño3.4 SSTAs. The XRO systematically outperforms the uninitialized/decoupled ExPO+IO+AO experiments with more accurate amplitude prediction of Niño3.4 SSTAs and extended skilful prediction of El Niño and La Niña event occurrences at longer lead-time of 6-18 months (Fig. 4a). For instance, the 1986/1987 El Niño event could be predicted 18 months in advance with XRO in our hindcast, as opposed to only 6 months in advance with uninitialized/decoupled ExPO+IO+AO experiments.

To better understand the influence of a specific climate mode on individual ENSO events, we examined the differences in ENSO SSTAs and WWV anomalies between control and uninitialized experiments for the 1997/98 El Niño and 1998/99/00 triple La Niña episodes (Fig. 4d-k) as well as for the full period (Extended Data Fig. 6). The ENSO forecast differences due to the initialization of other modes are pronounced when those SSTAs have sufficiently large amplitudes and during the season in which their interaction with ENSO is relatively strong. These effects of the non-ENSO modes usually last longer than their own SSTA persistence, indicating the activation of ENSO coupled recharge-discharge feedbacks as shown by the ENSO SSTA and WWV anomalies alternating with a few months lag.

In the extratropical Pacific, positive SSTAs for both the NPMM and SPMM in boreal spring can enhance ENSO SST warming 6-9 months later (Fig. 4d,h). However, the underlying mechanisms differ for the two different hemispheres. The NPMM warming leads to recharged WWV anomalies and subsequent ENSO SST warming, highlighting the important role of the trade wind charging mechanism[36]. In contrast, the SPMM warming directly generates SST warming on the equator, followed by sequential WWV discharge, which aligns with the finding that ENSO is thermally driven by the SPMM[37](Extended Data Fig. 6a-b).

We also find that coupling with the NPMM tends to favour multi-year ENSO events, such as the 1998/99/00 La Niña. The first year La Niña in 1998/99 set the stage for a strong spring NPMM cooling in 1999 (consistent with the strong nearly-instantaneous feedback mechanism[38]), which in turn reinforced WWV discharge and colder SSTAs (by ~0.3 °C) in the second year. This strong WWV discharged state persisted and re-intensified into the third year, causing SSTA to decrease (~0.4 °C) in the winter of the third year (Fig. 4d). Similar patterns are evident in multi-year La Niña events in 2007/08, 2010/11, and 2020/21/22 (blue shadings in Extended Data Fig. 6a). We emphasize that this contribution is also evident for the opposite ENSO phase, as seen in multi-year

El Niño events in 1986/87, 2014/15, and 2018/19 (Extended Data Fig. 6a). These results support the hypothesis that the coupling between NPMM and ENSO favours the existence of multi-year ENSO events[39–41].

In the Indian Ocean, the 1996 boreal autumn negative IOD event was found to induce a ~0.4 °C Niño3.4 SSTA increase ~15 months later, thus contributing to the 1997/98 super El Niño (Fig. 4f). Conversely, the 1997 boreal autumn positive IOD event led to a ~0.5 °C Niño3.4 SSTA decrease ~15 months later, thus playing a role in the 1998/99 La Niña (Fig. 4f). This aligns with previous finding[15] that negative IOD event favours the build-up of WWV (i.e., recharge) and contributes to the development of El Niño in the following year via the Bjerknes feedback. The SIOD mode, characterized by an SST east-west dipole over the southern IO, tends to induce ~0.2 °C Niño3.4 SSTA increase/decrease ~12-16 months later, often offsetting the IOD's effect (Fig. 4g). The IOB, although largely forced by ENSO, helps to accelerate the phase-transition of ENSO events[42]. For example, the IOB warming in 1998 contributed to a ~0.2 °C Niño3.4 SSTA decrease during the 1998/99 La Niña, about half the magnitude of the IOD-induced change (Fig. 4e). These results corroborate the findings in Fig. 3e that the Indian Ocean's influence on ENSO predictability is predominantly governed by the IOD.

In the Atlantic Ocean, the TNA warming favours Niño3.4 SSTA decrease 6-12 months later by about ~0.3 °C (Fig. 4i), consistent with a previous finding[17]. The 1997 boreal summer Atlantic Niña (ATL3 cold anomalies) was found to weakly favour Niño3.4 SSTA increase 6-12 months later by about ~0.15 °C (Fig. 4j). The positive phase of the SASD in 1997 contributed to a ~0.3 °C Niño3.4 SSTA increase 9-12 months later (Fig. 4k), in line with previous findings[19]. The Atlantic Ocean's influence is predominantly governed by the TNA and secondly by the SASD and ATL3.

For the 20/21/22 triple La Niña events, the strong positive IOD in 2019 autumn is among the most important contributors to the first year SSTA cooling (Extended Data Fig. 6d), and the

NPMM cooling is among the most important sources in amplifying the second year SSTA decrease (Extended Data Fig. 6a), consistent with previous findings[43,44]. The ongoing 2023/2024 El Niño occurrence can be predicted up to 18 months in advance in the decoupled ExPO+IO+AO experiment (Fig. 4b), largely due to the highly recharged WWV state caused by the preceding "triple-dip" La Niña events. The XRO refines the amplitude prediction for the 2023/2024 El Niño at longer lead-time of 9-18 months (Fig. 4a), with positive contributions from the preceding IOD and IOB conditions (Extended Data Fig. 6c,d).

Composites of the uninitialized experiments for the peak phase of El Niño/La Niña years (Fig. 4l) support that climate mode interactions contribute to the observed Niño3.4 SSTA anomalies, in addition to the generally stronger contribution from the equatorial Pacific recharge/discharge dynamics intrinsic to ENSO. The additional contributions are mainly from the NPMM, IOD, and TNA with large inter-event spread, with other modes playing secondary roles. The impacts are asymmetric (i.e., different impacts for El Niño and La Niña events) from some modes such as the IOB, SPMM, and SASD. The impact from the IOB on La Niña SSTA is much more pronounced than on El Niño SSTA, consistent with previous findings[14].

Predictability reduced by model biases

Next, we turn to the impacts of biases in comprehensive climate models on ENSO forecast skill. We conducted additional XRO model forecast experiments by using the operator parameters trained using the 91 historical simulation outputs from the Coupled Model Intercomparison Project (CMIP) phase 5 and 6 (see *"The XRO reforecasting experiments based on CMIP model outputs" in Methods*, Extended Data Table 2, red curves in Extended Data Fig. 1). Figure 5a reveals that the forecast skill of XRO^m, when trained solely on each CMIP CGCM, shows a wide inter-CGCM spread at lead-time from 7 to 17 months. Importantly, the forecast skill when the model is trained on CMIP output is consistently lower than for the model trained on observational data (Extended

Data Fig. 7a). This suggests that biases in all climate models reduce the ability of these CGCMs to forecast ENSO correctly.

We modified each XRO^{m} to remove these dynamical biases, by individually substituting the parameters obtained from the observations into three key components of the model: ENSO's internal dynamics ($\boldsymbol{L}_{\text{ENSO}}$), the remote climate mode feedbacks onto ENSO ($\boldsymbol{C}_1$), and the ENSO teleconnections to the remote modes ($\boldsymbol{C}_2$). Correcting the ENSO dynamics ($\boldsymbol{L}_{\text{ENSO}}$) generally enhances forecast skill at all lead-times (red curve in Fig. 5b, Extended Data Fig. 7b). This indicates that the way ENSO's core dynamics are biased in climate models is a major factor in lower ENSO forecast skill. Correcting the remote climate mode feedbacks onto ENSO ($\boldsymbol{C}_1$) also improves the ENSO forecasts for lead-time up to 16 months (magenta curve in Fig. 5b, Extended Data Fig. 7c). Thus, mode coupling is critical for ENSO development, as another source of bias. Correcting the ENSO teleconnections ($\boldsymbol{C}_2$) yields reduced ENSO skill (blue curve in Fig. 5b, Extended Data Fig. 7d), but greatly improves the forecast skill for other modes, such as the IOD (Extended Data Fig. 8). These results suggest that reduced biases in model ENSO dynamics and in climate mode interactions lead to more skilful ENSO forecasts.

Pantropical SST predictability

Lastly, we demonstrate that ENSO-climate mode interactions also enhance the SST predictability of other climate modes. For instance, the lead-time of skilful IOB forecast extends from 5 months in the uninitialized ENSO experiment to 19 months in the XRO control experiment (Supplementary Fig. 13c,j). The all-month IOD forecast skill extends to 5 months (the SON forecast to 8 months), supporting earlier findings that long lead IOD predictability arises from ENSO and is impacted by the signal-to-noise ratio[45]. The improvement is also evident for SSTA modes in the Atlantic Ocean (about 1 month, Supplementary Fig. 13f,g,h). Interestingly, there is no skill improvement to NPMM and SPMM, possibly because their initial state already includes ENSO information given the strong nearly-instantaneous feedback with ENSO (Fig. 2e,f, ref [38]).

In addition to ENSO amplitude, our XRO model can be expanded to also consider ENSO spatiotemporal diversity by using two ENSO SST indices (e.g. the Niño3 and Niño4 indices, as in the model XRO2, *see "The XRO2 ENSO types and pantropical SSTA forecasts" in Methods*). The XRO2 is able successfully predict the EP-type characteristic of the 1997/98 El Niño, and the mixed-type characteristic of the 2015/16 El Niño, up to 9 months in advance (Supplementary Table 3). In contrast, the NMME dynamical models fail to predict the correct type for the 1997/98 event, possibly due to long-standing model biases of westward-displaced ENSO SST anomalies[46]. The successful prediction of ENSO spatial diversity in the XRO has important implications for predicting global climate impacts that differ strongly for contrasting ENSO SSTA patterns. Furthermore, the skill of forecasted pantropical SSTA at 9-month lead using the regression model of ten forecasted SST indices outperforms the operational dynamical models in most regions except the Caribbean Sea (Supplementary Fig. 14). The successful forecasts of ENSO types and pantropical SSTA within the XRO framework highlight the essential importance of accurately representing ENSO-climate mode interactions in climate models for effective seasonal forecasting.

Discussion

The XRO model constitutes a parsimonious representation of the climate system in a reduced variable and parameter space that still captures the essential dynamics of interconnected global climate variability. We emphasize that the improvement of ENSO predictability in the XRO relative to that in the nRO ultimately all resides in the initial condition memory of the other climate modes, which is propagated forward by the unbiased operator. Thus, to improve ENSO predictions, climate models must correctly capture the recharge oscillator dynamics of ENSO and additionally, three compounding aspects of other climate modes: (i) the initial conditions of each mode, (ii) the seasonally modulated damping rate (i.e., the memory) of each mode, and (iii) the seasonally modulated teleconnection to ENSO from each mode. Tracing biases from the SSTA budget at the process level with the XRO framework can be used to inform climate model development. Moreover, the explainable predictability of pantropical climate variability as encapsulated by the XRO may be further enhanced by including multi-timescale interactions associated with the Madden-Julian Oscillation and westerly wind bursts at higher frequencies. The XRO framework can also provide a pathway for better understanding observed decadal and long-term changes in ENSO variability[33,34] and ENSO predictability[47–50].

References

1. McPhaden, M. J., Zebiak, S. E. & Glantz, M. H. ENSO as an Integrating Concept in Earth Science. *Science* **314**, 1740–1745 (2006).
2. Timmermann, A. *et al.* El Niño–Southern Oscillation complexity. *Nature* **559**, 535–545 (2018).
3. Cai, W. *et al.* Changing El Niño–Southern Oscillation in a warming climate. *Nat Rev Earth Environ* 1–17 (2021) doi:10.1038/s43017-021-00199-z.
4. Cane, M. A., Zebiak, S. E. & Dolan, S. C. Experimental forecasts of El Niño. *Nature* **321**, 827–832 (1986).
5. Barnston, A. G., Tippett, M. K., L'Heureux, M. L., Li, S. & DeWitt, D. G. Skill of Real-Time Seasonal ENSO Model Predictions during 2002–11: Is Our Capability Increasing? *Bull. Amer. Meteor. Soc.* **93**, 631–651 (2012).
6. Tang, Y. *et al.* Progress in ENSO prediction and predictability study. *Natl Sci Rev* **5**, 826–839 (2018).
7. L'Heureux, M. L. *et al.* ENSO Prediction. in *El Niño Southern Oscillation in a Changing Climate* 227–246 (American Geophysical Union (AGU), 2020). doi:10.1002/9781119548164.ch10.
8. Ham, Y.-G., Kim, J.-H. & Luo, J.-J. Deep learning for multi-year ENSO forecasts. *Nature* **573**, 568–572 (2019).
9. Zhou, L. & Zhang, R.-H. A self-attention–based neural network for three-dimensional multivariate modeling and its skillful ENSO predictions. *Science Advances* **9**, eadf2827 (2023).
10. Wang, H., Hu, S. & Li, X. An Interpretable Deep Learning ENSO Forecasting Model. *Ocean-Land-Atmosphere Research* **2**, 0012 (2023).
11. Cai, W. *et al.* Pantropical climate interactions. *Science* **363**, eaav4236 (2019).

12. Chiang, J. C. H. & Vimont, D. J. Analogous Pacific and Atlantic Meridional Modes of Tropical Atmosphere–Ocean Variability. *Journal of Climate* **17**, 4143–4158 (2004).

13. Zhang, H., Clement, A. & Nezio, P. D. The South Pacific Meridional Mode: A Mechanism for ENSO-like Variability. *Journal of Climate* **27**, 769–783 (2014).

14. Jin, Y. *et al.* The Indian Ocean weakens ENSO Spring Predictability Barrier: Role of the Indian Ocean Basin and Dipole modes. *Journal of Climate* **36**, 8331–8345 (2023).

15. Izumo, T., Vialard, J. & Lengaigne, M. Influence of the state of the Indian Ocean Dipole on the following year's El Niño. *Nat. Geosci.* 168–172 (2010) doi:10.1038/NGEO760.

16. Jo, H.-S. *et al.* Southern Indian Ocean Dipole as a trigger for Central Pacific El Niño since the 2000s. *Nat Commun* **13**, 6965 (2022).

17. Ham, Y.-G., Kug, J.-S., Park, J.-Y. & Jin, F.-F. Sea surface temperature in the north tropical Atlantic as a trigger for El Niño/Southern Oscillation events. *Nature Geosci* **6**, 112–116 (2013).

18. Ham, Y.-G., Kug, J.-S. & Park, J.-Y. Two distinct roles of Atlantic SSTs in ENSO variability: North Tropical Atlantic SST and Atlantic Niño. *Geophysical Research Letters* **40**, 4012–4017 (2013).

19. Ham, Y.-G. *et al.* Inter-Basin Interaction Between Variability in the South Atlantic Ocean and the El Niño/Southern Oscillation. *Geophysical Research Letters* **48**, e2021GL093338 (2021).

20. Jansen, M. F., Dommenget, D. & Keenlyside, N. Tropical Atmosphere–Ocean Interactions in a Conceptual Framework. *J. Climate* **22**, 550–567 (2009).

21. Frauen, C. & Dommenget, D. Influences of the tropical Indian and Atlantic Oceans on the predictability of ENSO. *Geophys. Res. Lett.* **39**, L02706 (2012).

22. Luo, J.-J. *et al.* Interaction between El Niño and Extreme Indian Ocean Dipole. *J. Climate* **23**, 726–742 (2010).

23. Keenlyside, N. S., Ding, H. & Latif, M. Potential of equatorial Atlantic variability to enhance El Nino prediction. *Geophys. Res. Lett.* **40**, 2278–2283 (2013).

24. Luo, J.-J., Liu, G., Hendon, H., Alves, O. & Yamagata, T. Inter-basin sources for two-year predictability of the multi-year La Nina event in 2010-2012. *Sci Rep* **7**, 2276 (2017).

25. Keenlyside, N. *et al.* Basin Interactions and Predictability. in *Interacting Climates of Ocean Basins: Observations, Mechanisms, Predictability, and Impacts* (ed. Mechoso, C. R.) 258–292 (Cambridge University Press, Cambridge, 2020). doi:10.1017/9781108610995.009.

26. Exarchou, E. *et al.* Impact of equatorial Atlantic variability on ENSO predictive skill. *Nature Communications* **12**, 1612 (2021).

27. Alexander, M. A., Shin, S.-I. & Battisti, D. S. The Influence of the Trend, Basin Interactions, and Ocean Dynamics on Tropical Ocean Prediction. *Geophysical Research Letters* **49**, e2021GL096120 (2022).

28. Kido, S., Richter, I., Tozuka, T. & Chang, P. Understanding the interplay between ENSO and related tropical SST variability using linear inverse models. *Clim Dyn* **61**, (2023).

29. Stuecker, M. F. *et al.* Revisiting ENSO/Indian Ocean Dipole phase relationships. *Geophys. Res. Lett.* **44**, 2016GL072308 (2017).

30. Zhang, W., Jiang, F., Stuecker, M. F., Jin, F.-F. & Timmermann, A. Spurious North Tropical Atlantic precursors to El Niño. *Nature Communications* **12**, 3096 (2021).

31. Lee, S.-K. *et al.* On the Fragile Relationship Between El Niño and California Rainfall. *Geophysical Research Letters* **45**, 907–915 (2018).

32. Jeong, H., Park, H.-S., Stuecker, M. F. & Yeh, S.-W. Distinct impacts of major El Niño events on Arctic temperatures due to differences in eastern tropical Pacific sea surface temperatures. *Science Advances* **8**, eabl8278 (2022).

33. McPhaden, M. J. A 21st century shift in the relationship between ENSO SST and warm water volume anomalies. *Geophysical Research Letters* **39**, (2012).

34. Choi, J., An, S.-I. & Yeh, S.-W. Decadal amplitude modulation of two types of ENSO and its relationship with the mean state. *Clim Dyn* **38**, 2631–2644 (2012).

35. Zhao, Y., Jin, Y., Capotondi, A., Li, J. & Sun, D. The Role of Tropical Atlantic in ENSO Predictability Barrier. *Geophysical Research Letters* **50**, e2022GL101853 (2023).

36. Anderson, B. T. On the Joint Role of Subtropical Atmospheric Variability and Equatorial Subsurface Heat Content Anomalies in Initiating the Onset of ENSO Events. *Journal of Climate* **20**, 1593–1599 (2007).

37. Larson, S. M., Pegion, K. V. & Kirtman, B. P. The South Pacific Meridional Mode as a Thermally Driven Source of ENSO Amplitude Modulation and Uncertainty. *Journal of Climate* **31**, 5127–5145 (2018).

38. Stuecker, M. F. Revisiting the Pacific Meridional Mode. *Scientific Reports* **8**, 3216 (2018).

39. Park, J.-H. *et al.* Mid-latitude leading double-dip La Niña. *International Journal of Climatology* **41**, E1353–E1370 (2021).

40. Ding, R. *et al.* Multi-year El Niño events tied to the North Pacific Oscillation. *Nat Commun* **13**, 3871 (2022).

41. Geng, T. *et al.* Increased occurrences of consecutive La Niña events under global warming. *Nature* **619**, 774–781 (2023).

42. Kug, J.-S. & Kang, I.-S. Interactive Feedback between ENSO and the Indian Ocean. *J. Climate* **19**, 1784–1801 (2006).

43. Hasan, N. A., Chikamoto, Y. & McPhaden, M. J. The influence of tropical basin interactions on the 2020–2022 double-dip La Niña. *Frontiers in Climate* **4**, (2022).

44. Iwakiri, T. *et al.* Triple-Dip La Niña in 2020–23: North Pacific Atmosphere Drives 2nd Year La Niña. *Geophysical Research Letters* **50**, e2023GL105763 (2023).

45. Zhao, S. *et al.* Improved Predictability of the Indian Ocean Dipole Using a Stochastic Dynamical Model Compared to the North American Multimodel Ensemble Forecast. *Wea. Forecasting* **35**, 379–399 (2020).

46. Chen, H.-C., Jin, F.-F., Zhao, S., Wittenberg, A. T. & Xie, S. ENSO Dynamics in the E3SM-1-0, CESM2, and GFDL-CM4 Climate Models. *Journal of Climate* **34**, 9365–9384 (2021).

47. Chen, D., Cane, M. A., Kaplan, A., Zebiak, S. E. & Huang, D. Predictability of El Niño over the past 148 years. *Nature* **428**, 733–736 (2004).

48. Liu, T., Song, X., Tang, Y., Shen, Z. & Tan, X. ENSO Predictability over the Past 137 Years Based on a CESM Ensemble Prediction System. *Journal of Climate* **35**, 763–777 (2022).

49. Weisheimer, A. *et al.* Variability of ENSO Forecast Skill in 2-Year Global Reforecasts Over the 20th Century. *Geophysical Research Letters* **49**, e2022GL097885 (2022).

50. Lou, J., Newman, M. & Hoell, A. Multi-decadal variation of ENSO forecast skill since the late 1800s. *npj Clim Atmos Sci* **6**, 1–14 (2023).

Figure Legends

Figure 1. Different sources of ENSO predictability and associated different global impacts. **a**, Observed SSTA standard deviation pattern calculated from the detrended ORAS5 reanalysis during 1979-2022. The different coloured boxes represent area-averaged SSTA index regions for ENSO and other selected climate modes (Supplementary Table 1). **b**, Observed standardized Niño3.4 index and various potential precursor indices for the 1997/98 and 2015/16 El Niño events, with the numbers in the parentheses indicating the preceding (-1), current (0), and subsequent (1) years. The error bars show the spread (one standard deviation) among different observational products (Supplementary Table 2). The lead correlation of various indices with regard to the NDJ Niño3.4 index is indicated near the bottom of the plot. **c-d**, Observed precipitation anomalies (percentage) relative to climatology (shading) during (c) 1997/98 December-March (DJFM) and (d) 2015/16 DJFM. Contours denote the significant positive (green) and negative (brown) correlations between DJFM precipitation anomalies and the DJFM Niño3.4 SSTA index that exceed the 95% confidence level, based on Student's *t*-test. The observed 1997/98 and 2015/16 El Niño events were associated with different precursor patterns and global climate impacts, despite similar Niño3.4 index amplitude.

Figure 2. Superior Efficacy of the XRO in simulating and reforecasting ENSO. a-c, Seasonally varying standard deviation (a), skewness (b), and power spectrum (c), respectively, of Niño3.4 using ORAS5 (*black*) and the XRO stochastic simulation (*red*). **d-l**, monthly cross-correlations between Niño3.4 and different indices indicated in the titles; Dashed grey curves show the auto-correlation of Niño3.4 and vertical blue dashed lines denote a lead-time of 6(WWV), 6(NPMM), 4(SPMM), 12(IOB), 14(IOD), 10(SIOD), 9(TNA), 6(ATL3), and 9(SASD) months respectively; Abscissas indicate lead-time in months (negative values representing Niño3.4 lag). Red shading indicates the 10%-90% ensemble spread of simulated 43-year segments, obtained from splitting a 43,000-year XRO simulation into 1000 non-overlapping parts. **m**, All-months

correlation skill of 3-month running-mean Niño3.4 as a function of forecast lead for forecasts verified on 2002-2022 for the out-of-sample nRO (*magenta*) and XRO (*red*) fitted on 1950-1999, the AI model (*blue*), the XRO control fitted on 1979-2022 (*black*) and IRI operational models, the ensemble mean of dynamical models (*dark purple curve*), and ensemble-mean of statistical models (*dark cyan curve*). **n**, Same as **m**, but for Niño3.4 forecast skills for nRO (*magenta*) and XRO (*red*) control forecasts, AI model forecasts (*blue*), and NMME dynamical model forecasts (multi-model ensemble mean in *black*, ensemble-means from individual models in *other colours*). Validation period is 1979-2022 except for the AI and NMME models (period indicated in the legend). **o-p**, Correlation skill of nRO and XRO Niño3.4 forecasts as a function of initialization month (ordinate) and target month (abscissa; superscripts 0, 1, and 2 denote the current and subsequent years, respectively). Hatching highlights forecasts with a correlation <0.5. Dashed vertical blue lines denote the spring predictability barrier. The XRO accurately simulates the fundamental observed ENSO characteristics, its lead-lag relationships with other climate modes, and provides skilful forecasts at lead-times up to 16-18 months.

Figure 3. Quantifying the increased ENSO forecast skills from the coupled influences outside equatorial Pacific during 1979-2022. a, the all-months correlation skill of the 3-month running mean Niño3.4 index as a function of the forecast lead month in the control experiment (XRO, *black line*), the uninitialized ExPO+IO+AO experiment ($U_{\mathrm{ExPO+IO+AO}}$, removing initial conditions of other basins; *red line*), the decoupling ExPO+IO+AO experiment ($D_{\mathrm{ExPO+IO+AO}}$, removing the coupling of ENSO with other basins; *blue line*), and the relaxing ExPO+IO+AO to observations experiment ($R_{\mathrm{ExPO+IO+AO}}$, adding perfect "future" information of other basins in a hindcast case; *magenta line*). **b-d**, the skill difference of the Niño3.4 index as a function of initial time and target month between XRO and $D_{\mathrm{ExPO+IO+AO}}$ (b), between XRO and $U_{\mathrm{ExPO+IO+AO}}$ (c), and between $U_{\mathrm{ExPO+IO+AO}}$ and $D_{\mathrm{ExPO+IO+AO}}$ (d). **e-g**, Same as d, but for difference between control and the uninitialized ExPO, IO, and AO experiments, respectively. Hatching indicates that the correlation difference is significant at 90% confidence level using the two-tailed Fisher z-transformation test. The sensitivity experiments demonstrate the importance of the extratropical Pacific, Indian Ocean, and Atlantic Ocean in enhancing ENSO forecast skill, with distinct seasonal dependence. The interbasin memory sustains ENSO forecast skill beyond the spring predictability barrier with the IO and AO contributing skill in boreal summer and the ExPO in boreal winter.

Figure 4. Delineating contributions to ENSO amplitudes from other climate modes. a, b, c, Time series of Niño3.4 forecasts for the (a) XRO model, (b) decoupled ExPO+IO+AO experiment,

and (c) uninitialized ExPO+IO+AO experiment, as function of target time and forecast lead. **d-k**, the difference of Niño3.4 SSTAs (shading) and WWV anomalies (contours with interval of 0.6 m, positive in red and negative in black dashed, zero omitted), as a function of forecast start month and target month, between the control and uninitialized climate mode experiments for NPMM, IOB, IOD, SIOD, SPMM, TNA, ATL3, and SASD, respectively. Vertical reference dashed lines denote December of El Niño (red) and La Niña (blue) years, respectively. In **d-k**, the normalized observed time series of each climate-mode SSTA index is indicated on the bottom axis; the black arrows indicate the flow of forecast integration started from the selected time in the bottom. **l**, Composite difference of Nov-Dec-Jan Niño3.4 SSTA forecasts during El Niño events (red) and La Niña events (blue) between control and uninitialized U_{m} experiments started from months in a specific preceding season (-1 and 0 in parentheses denote preceding and current year, x axis from left to right is U_{Nino34}, U_{WWV}, U_{NPMM}, U_{SPMM}, U_{IOB}, U_{IOD}, U_{SIOD}, U_{TNA}, U_{ATL3}, and U_{SASD}, respectively); the events are selected when Nov-Dec-Jan Niño3.4 indices are greater than their standard deviation, which includes 7 El Niño events (1982, 1986, 1991, 1997, 2002, 2009, 2015) and 5 La Niña events (1988, 1998, 1999, 2007, 2010). The error bars show one standard deviation spread among the 7 El Niño/5 La Niña events. The XRO sensitivity experiments quantify the pathways via which the other climate modes influence El Niño and La Niña events.

Figure 5. Linking biases in the dynamics captured by the XRO to climate model deficiencies in forecasting ENSO during 1979-2022. (a) The all-months correlation skill of the 3-month running mean Niño3.4 index in XRO$^{\mathrm{m}}$ trained solely on 91 individual CMIP model outputs (*grey curves*), and in XRO trained on observations (*red*) and multi-model ensemble mean NMME models (*black*). (b) The ensemble mean and 10%-90% spread band of the changes in correlation skill of the Niño3.4 index, obtained by either correcting ENSO's internal linear dynamics ($\mathrm{XRO}^{m}_{L_{\mathrm{ENSO}}}$- XRO$^{\mathrm{m}}$, *red*), or correcting the remote climate mode feedbacks onto ENSO ($\mathrm{XRO}^{m}_{\boldsymbol{C}_1}$- XRO$^{\mathrm{m}}$, *magenta*), or correcting ENSO's teleconnections to the remote climate modes ($\mathrm{XRO}^{m}_{\boldsymbol{C}_2}$- XRO$^{\mathrm{m}}$, *blue*). Reforecasts using the XRO trained on climate model output, show that reduced biases in model ENSO dynamics and in climate mode interactions lead to more skilful ENSO forecasts.

Methods

Extended Nonlinear Recharge-Oscillator model (XRO)

The XRO model consists of a nonlinear recharge oscillator model for ENSO[51,52] coupled to stochastic-deterministic models (i.e., seasonally modulated first order autoregressive models) for the other climate modes[53–55]:

$$\frac{d}{dt}\begin{pmatrix}\boldsymbol{X}_{\mathrm{ENSO}}\\ \boldsymbol{X}_M\end{pmatrix} = \boldsymbol{L}\begin{pmatrix}\boldsymbol{X}_{\mathrm{ENSO}}\\ \boldsymbol{X}_M\end{pmatrix} + \begin{pmatrix}\boldsymbol{N}_{\mathrm{ENSO}}\\ \boldsymbol{N}_M\end{pmatrix} + \sigma_\xi \boldsymbol{\xi}, \tag{1}$$

$$\frac{d\boldsymbol{\xi}}{dt} = -r_\xi \boldsymbol{\xi} + \boldsymbol{w}(t), \tag{2}$$

where $\boldsymbol{X}_{\mathrm{ENSO}} = [T_{\mathrm{ENSO}}, h]$ and $\boldsymbol{X}_M = [T_{\mathrm{NPMM}}, T_{\mathrm{SPMM}}, T_{\mathrm{IOB}}, T_{\mathrm{IOD}}, T_{\mathrm{SIOD}}, T_{\mathrm{TNA}}, T_{\mathrm{ATL3}},\ T_{\mathrm{SASD}}]$ are state vectors of ENSO and other climate modes, respectively. This model allows for two-way interactions between ENSO and the other modes. Two indices are used to describe the oscillatory behaviour of ENSO[52,56]. They consist of SSTAs averaged over the Niño3.4 region 170°–120°W, 5°S–5°N (T_{ENSO}) and thermocline depth anomalies averaged over the equatorial Pacific 120°E–80°W, 5°S–5°N (h), i.e., the WWV index (with a constant factor of the area it covers). For other climate modes, we consider the SST indices of multiple climate modes (Supplementary Table 1) that have been shown to interact with ENSO, including the NPMM[12,38,57] and SPMM[13] in the extratropical Pacific, the IOB[14,58,59], IOD[60,61,15,43], and SIOD[16] in the Indian Ocean, and TNA[17,62], ATL3[63,18,43,64] and SASD[65,19] in the Atlantic Ocean. We recognise the possibility of enhancing ENSO forecast skill by incorporating additional modes of variability, provided they directly interact with ENSO, exhibit substantial memory extending beyond months, and offer additional sources of variability beyond the chosen eight.

The dynamics governing the state matrix $\boldsymbol{X}$ (consisting of 10 variables) contains linear ($\boldsymbol{L}$), nonlinear ($\boldsymbol{N}$), and stochastic ($\boldsymbol{\xi}$) terms. The linear dynamics contains four key submatrices, organized as follows:

$$\boldsymbol{L} = \begin{pmatrix} \boldsymbol{L}_{\text{ENSO}} & \boldsymbol{C_1} \\ \boldsymbol{C_2} & \boldsymbol{L}_M \end{pmatrix}, \tag{3}$$

where the linear operator submatrix $\boldsymbol{L}_{\text{ENSO}}$ describes the ENSO internal recharge-discharge dynamics[52,66], $\boldsymbol{L}_M$ represent the internal processes and interactions among the other climate modes; $\boldsymbol{C}$ are coupling submatrices, with $\boldsymbol{C_2}$ describing the impact of ENSO on other climate modes[29] and $\boldsymbol{C_1}$ describing the feedback of other modes on ENSO. To implement nonlinear dynamics associated with ENSO asymmetry, quadratic nonlinearities $b_1 T_{\text{ENSO}}^2 + b_2 T_{\text{ENSO}} h$ are incorporated into the SSTA equation of ENSO following Jin et al.[51] and An et al.[67], specifically, $\boldsymbol{N}_{\text{ENSO}} = [b_1 T_{\text{ENSO}}^2 + b_2 T_{\text{ENSO}} h, 0]$. These nonlinearities can be related to deterministic nonlinear ocean advection[68,67], as well as to atmospheric nonlinearity implicitly through the nonlinear SST-wind stress feedback[69–71]. A local quadratic nonlinearity $b_3 T_{\text{IOD}}^2$ is also incorporated in the SSTA equation for the IOD following the recent insights from An et al.[72] that IOD asymmetry is dominated by local nonlinear processes. The nonlinear terms for modes other that the IOD are set to zero given their observed smaller asymmetry and skewness (Supplementary Fig. 5i-j,m-p, ref[73]), specifically, $\boldsymbol{N}_M = [0,0,0, b_3 T_{\text{IOD}}^2, 0,0,0,0]$. Lastly, $\boldsymbol{\xi}$ is stochastic forcing due to weather and other high-frequency noise such as the Madden-Julian Oscillation and westerly wind bursts, which is approximated as red noise with decorrelation time scales of r_ξ and amplitudes of σ_ξ, respectively. Specifically, $\boldsymbol{w}(t)$ in Eq. (2) denotes white noise with a Gaussian distribution $N(0, 2r_\xi)$ ensuring that the variance of $\boldsymbol{\xi}$ is maintained at the unit level. We acknowledge the importance of the multiplicative (state-dependent) noise forcing on ENSO[74,75], however, accurately estimating the magnitude of the state-dependence remains a challenge with the observational data length.

Due to the strong seasonal dependence of ENSO and other climate modes, we incorporate seasonality by estimating the operator matrix and nonlinear parameters as

$$\boldsymbol{L} = \boldsymbol{L_0} + \sum_{j=1}^{2} (\boldsymbol{L}_j^c \cos j\omega t + \boldsymbol{L}_j^s \sin j\omega t)\,, \tag{4}$$

$$\boldsymbol{N} = \boldsymbol{N_0} + \sum_{j=1}^{2} \left(\boldsymbol{N}_j^c \cos j\omega t + \boldsymbol{N}_j^s \sin j\omega t\right), \tag{5}$$

where $\omega = 2\pi/(12\, months)$, and the subscripts 0, 1 and 2 indicate the mean, annual cycle, and the semi-annual components, respectively. The linear operator and nonlinear coefficients for the observations and CMIP simulations are estimated simultaneously by using multivariate linear regression and expressing the state vector tendency in Eq. (1) through a forward-differencing scheme following ref[76,77]. Compared to the conventional method, which estimates the annual cycle of operators by splitting the monthly data on each calendar month, our approach enables us to obtain the seasonal modulated operators without reducing sample size by a factor of 12. We emphasize that our approach constitutes the minimum number of degrees of freedom necessary to represent the seasonality. There are 50 parameters for each tendency equation of the 10 variables in the system (except 60 for T_{ENSO} and 55 for T_{IOD}). To meet the rule of thumb for regression sample size (at least 10 subjects per predictor)[78], 40–50 years of data is required to achieve a robust fit. The total number of parameters is 515, which are orders of magnitude fewer degrees of freedom than the AI models in comparison have, the latter which have substantially more than 100,000 free parameters[8].

The noise parameters are determined from the residuals of the XRO fit. There are 20 total noise parameters, i.e., a noise amplitude and decorrelation time scale for each of the 10 variables in the system. The noise amplitude $\square_{\square}$ is estimated from the standard deviations of the residuals of the XRO fit. The decorrelation time scales are estimated as $r_\xi = -ln(\boldsymbol{a_1})/\delta t$, where $\boldsymbol{a_1}$ is the lag-1 autocorrelation of the residual of the XRO fit. The order of observed noise time scale r_ξ^{-1} is about 0.25 ~ 0.70 months.

The XRO builds on the legacies of the Hasselmann stochastic climate model capturing upper ocean memory in SST variability, and the recharge oscillator model for the oscillatory core dynamics of ENSO. As a multivariate dynamical system, comparing with previous linear inverse models[79,28,27,80,35], the XRO offers an enhanced capability in representing the dynamics of ENSO (including recharge/discharge dynamics) and climate mode interactions, encompassing their seasonality and nonlinearity, which are of crucial importance in improving ENSO forecast skill. Moreover, the state vectors for linear inverse models are typically derived from the leading principal components truncated within the Empirical Orthogonal Function space, which, however, may not always represent physical processes.

Nonlinear RO model (nRO)

To highlight the climate mode interactions, we compared the XRO model with a nRO, which is described as:

$$\frac{d}{dt}\boldsymbol{X}_{\mathrm{ENSO}} = \boldsymbol{L}_{\mathrm{ENSO}}\boldsymbol{X}_{\mathrm{ENSO}} + \boldsymbol{N}_{\mathrm{ENSO}} + \sigma_{\xi_{\mathrm{ENSO}}}\boldsymbol{\xi}_{\mathrm{ENSO}}. \tag{5}$$

This model includes only processes internal to the tropical Pacific. The parameters for the nRO model are fitted separately.

Observational data

We use eight observational SST and 3-dimensional ocean temperature datasets to account the uncertainties in estimating the SST in global oceans and subsurface state in the equatorial Pacific (Supplementary Table 2). They include three observational SST reconstructions: HadISST (Hadley Centre Sea Ice and Sea Surface Temperature dataset version 1.1)[81], ERSST v5 (Extended Reconstructed Sea Surface Temperature version 5)[82] and COBE-SST 2 (Centennial in situ Observation-Based Estimates of Sea Surface Temperature version 2)[83] for 1871-2023; and five reanalysed SST and ocean temperature datasets: GECCO3 for 1950-2018 (the German contribution to Estimating the Circulation and Climate of the Ocean version 3)[84], GODAS for 1980-2023 (Global Ocean Data Assimilation System)[85], ORAS5 for 1958-2023 (the ECMWF Ocean Reanalysis System 5)[86], ORA20C for 1900-2009 (ensemble of 10-member ECMWF Ocean Reanalysis of the 20th Century)[87], PEODAS for 1960-2014 (the Predictive Ocean Atmosphere Model for Australia Ensemble Ocean Data Assimilation System)[88], and SODA224 for 1871-2010 (Simple Ocean Data Assimilation Phase 2.2.4)[89]. The thermocline depth is defined as the depth of the 20°C isotherm. We also use surface air temperature from the ERA5 reanalysis[90], and gridded precipitation from the Climate Prediction Center Merged Analysis of Precipitation (CMAP)[91] for 1979-2022. The monthly anomaly fields were calculated by removing the monthly climatology for the period of 1979-2022 and the quadratic trend over the whole period. We have focused on the satellite era from 1979 onwards because SST observations are sparse in the pre-satellite period.

Climate forecast and hindcast data

We use the 3-month averaged Niño3.4 index forecasts from the operational International Research Institute for Climate and Society (IRI) ENSO Forecast product[5]. We also use SST hindcasts and real-time forecasts from ten models participating in the North American Multi-

Model Ensemble (NMME) project[92]. The ensemble sizes range from 10 to 24 for each model (Supplementary Table 4). The monthly forecast anomalies were calculated with respect to the monthly climatology from January 1982 to December 2010 for each member and forecast lead. For CCSM4 and CFSv2, we eliminate the discontinuous forecast biases by calculating the forecast anomalies using two different climatological periods of 1982–98 and 1999–2010, respectively, following ref[45].

In addition, we use the Niño3.4, Niño3, and Niño4 indices forecasts from an AI model (the 3D-Geoformer ENSO neural network model[9]) covering the period of 1983-2021. This model demonstrated ENSO forecast skills comparable with the convolutional neural networks (CNN) model developed by Ham et al.[8], which is among the most skilful AI ENSO forecasts[93,94].

Stochastically forced XRO simulations

To assess the XRO's performance in simulating ENSO and mode interactions, we conducted stochastically forced simulations using the operators and stochastic forcing matrices estimated from the ORAS5 reanalysis for 1979-2022 (*black curves* in Extended Data Fig. 1). We numerically integrate Eqs. 1-2 with a time step of 0.01 month for 45,000 years and archive monthly-averaged states for the analysis. The last 43,000 years were analysed and split into 1000 non-overlapping epochs of 43-year each, aligning with the observational record length. An example of simulated Niño3.4 SSTA index for the 10 consecutive centuries is shown in Supplementary Fig. 3.

Out-of-sample reforecasts

To perform robust out-of-sample testing of the XRO performance, we next use observational data including the pre-satellite period since at least 40-50 years of data are required to get a robust

XRO fit. We choose to discard data before 1950 since there are large uncertainties in the SSTA and equatorial thermocline depth indices (Supplementary Fig. 15). Therefore, we fitted the XRO and nRO models on 1950-1999 (50 years) data, conducted deterministic retrospective 21-month forecasts by integrating the XRO (Eq. 1) and nRO (Eq. 5) initialized from observed state values for the period of 2002-2022, and verified the model against observations in the 2002-2022 period, To access the impact of the decadal change in the performance of the XRO in forecasting ENSO, we also verified the model on two other 21-year no-overlapping periods: the previous period 1950-1970 (in which period of 1973-2022 data was used for training) and the middle period 1972-1992 (in which the periods of 1950-1970 and 1994-2022 data was used for training). The multi-data-products ensemble mean SSTA and WWV anomaly indices were used for fitting and verification.

Control XRO and nRO reforecasts

Using the operator and stochastic forcing parameters estimated from the ORAS5 reanalysis for 1979-2022, we conducted a control experiment by integrating the XRO (Eq. 1) initialized from observed state values of $[T_{\mathrm{ENSO}}, h, T_{\mathrm{NPMM}}, T_{\mathrm{SPMM}}, T_{\mathrm{IOB}}, T_{\mathrm{IOD}}, T_{\mathrm{SIOD}}, T_{\mathrm{TNA}}, T_{\mathrm{ATL3}}, T_{\mathrm{SASD}}]$ with retrospective 21-month forecasts for the period of January 1979–October 2023 (referred to XRO). The ensemble mean forecast of 100-members is almost identical to the deterministic forecast in which the stochastic forcing terms are neglected during the integration (Supplementary Fig. 16a,b). Although the 100-member stochastic XRO forecasts provide an opportunity for probabilistic ENSO forecasts (Supplementary Fig. 16c-f), here we focus on the deterministic skill and neglect the stochastic forcing terms in all the remaining forecast experiments. Similarly, we conducted a nRO deterministic experiment by integrating Eq. (5) initialized from observed state values of $[T_{\mathrm{ENSO}}, h]$.

Cross-validated reforecasts.

We carried out cross-validated forecasts using both the XRO and nRO models from the ORAS5 reanalysis for 1979-2022, employing a jackknife subsampling approach. We sequentially excluded 3-year segments of data (1979-81, 1982-85, 1986-89, 1990-93, 1994-97, 1998-2001, 2002-05, 2006-09, 2010-13, 2014-17, 2018-21, and 2022), then trained the model operator parameters based on the remaining data. Subsequently, we generated forecasts for each month during the years not included in the model fitting. The uncertainty in the fitted parameters is illustrated as *black shading* in Extended Data Fig. 1. The skill of cross-validated forecast is not sensitive to the choice of excluding from 2 to 7 years (Supplementary Fig. 8a).

Large ensemble simulations and perfect model reforecasting experiments

To assess of the robustness of the XRO fitting and forecasting performance, we use large ensemble (LENS) historical simulations for four climate models: Community Earth System Model version 1 (CESM1)[95], version 2 (CESM2)[96], Model for Interdisciplinary Research on Climate version 6 (MIROC6)[97], and Max Planck Institute for Meteorology Earth System Model version 1.1 (MPI-ESM)[98]. Each LENS was generated by repeatedly running the same model simulation with identical external forcing but with small initial condition differences. The number of members for each LENS used in this study are as follows: 39 for CESM1, 100 for CESM2, 50 for MIROC6, and 99 for MPI-ESM. We use the historical period of 1959-2002, aligning it with the observational record length (43 years).

We performed the “perfect model” reforecast, where the XRO model was trained by the LENS output and tasked to reforecast itself instead of the observations. We carried out twin experiments for each LENS (Supplementary Fig. 8b-e). The “Same-Member” reforecast experiment, in which the XRO model is repeatedly fitted for a member, forecasted, and verified against the same member. This aligns with the XRO control experiment for the observations. In the "Cross-Member" reforecast experiment, the XRO model is fitted for a specific member but forecasted and verified against a different member (an independent realization in the LENS). Specifically, we forecast ensemble member *j* using the two versions of XRO models, which were fitted on member *j-1 and j-2* data, respectively, and repeat the process for all members within the LENS. The skill difference between the Cross-Member experiment and the Same-Member experiment isolates the uncertainty of XRO parameter fitting and its impact on reforecasting skill. All four LENS results using the same observational record length (43-year) confirm that the uncertainty in parameter estimation leads to XRO reforecasting correlation skill error of less than 0.1 within 21 lead months (Supplementary Fig. 8b-e).

Quantitative reforecasting experiments

To rigorously dissect the interplay between ENSO and the different climate modes in the different ocean basins, we designed three sets of sensitivity experiments to mimic the experiment protocol of previous CGCM studies:

a) Uninitialized experiments: We performed uninitialized mode-□ experiments (U_j) by setting the initial condition of $□_{□}$ to zero, while keeping everything else the same as in the control experiment. The effect of the mode-□ initial condition can be assessed as the difference between the control and U_j (XRO-U_j). To disentangle the role of a specific ocean basin's initial conditions, we also conducted uninitialized experiments by setting the initial conditions of all modes to zero in the corresponding ocean basins. For example, the uninitialized extratropical Pacific Ocean experiment (referred to as U_{ExPO}) is the same as the control experiment but with the initial conditions of the NPMM and SPMM set to zero. Similarly, U_{IO}, $U_{\mathrm{AO}}$and $U_{\mathrm{ExPO+IO+AO}}$ denote the uninitialized Indian Ocean, uninitialized Atlantic Ocean, and uninitialized "all other basins" experiments, respectively. In addition, the uninitialized ENSO SSTA (U_{Nino34}) and WWV anomaly (U_{WWV}) experiments are same as XRO, except that the initial conditions of T_{ENSO} and h are set to zero, respectively. The uninitialized ENSO (U_{ENSO}) experiment is same as XRO, but the initial conditions of both T_{ENSO} and h are set to zero. The difference in the climate system response between the control experiment and U_j isolates the effect of mode-*j*/basin-*j*'s initialization.

b) Decoupled experiments: We performed decoupled mode-j experiments (referred to D_j) – in which specific mode(s) are suppressed – by strongly increasing the diagonal damping rate of mode-j in the $\boldsymbol{L}$ operator to an *e*-folding time scale of 5 days. This mimics the partially coupled experiments in fully coupled climate models that restore the ocean surface temperature toward prescribed conditions. The differences between the control experiment and D_j isolate the role of mode-j in the system. To disentangle the role of the different ocean basins, we conducted decoupled ocean basin experiments. For example, the decoupled extratropical Pacific Ocean experiment (referred to D_{ExPO}) removes both the NPMM and SPMM from the system. Similarly, the decoupled Indian Ocean experiment (D_{IO}) removes the IOB, IOD and SIOD together from the system; the decoupled Atlantic Ocean experiment (D_{AO}) removes the TNA, ALT3, and SASD together from the system; and the decoupled all other modes experiment ($D_{\text{ExPO+IO+AO}}$) removes all other modes except ENSO. We note that the $D_{\text{ExPO+IO+AO}}$ experiment is very close to the nRO in which the parameters were fitted separately. The difference between the control experiment and D_j isolates the effect of mode-*j*/basin-*j*'s coupling. The sum of individual basin decoupled experiments exceeds the effect of decoupling all at once (Extended Data Fig. 3b,d,e), suggesting the presence of indirect pathways due to interactions among basins.

c) *Relaxation towards observations experiments:* We performed relaxation ocean basin-j experiments (referred to R_j) by relaxing the SSTA indices towards the observations in the corresponding ocean basins with a time scale of 5 days. For example, the relaxation extratropical Pacific Ocean experiment (referred to as R_{ExPO}) is the same as the control but with the NPMM and SPMM being relaxed to the observations. Similarly, R_{IO}, R_{AO}, and $R_{\mathrm{ExPO+IO+AO}}$ denote the relaxation Indian Ocean, relaxation Atlantic Ocean, and relaxation all other basins except the equatorial Pacific experiments. The difference between the control experiment and R_j highlights the effect from perfect "future" knowledge of basin-j. The relaxation towards observations experiments greatly overestimate ENSO forecast skill because of built in presumed perfect predictions for the stochastic excitations and ENSO's impacts on the modes in these basins (*magenta curves* in Extended Data Fig. 3d,e).

Losing memory experiments

We carried out "losing memory" experiments by artificially adding additional damping to the original diagonal damping rates of all other non-ENSO modes in the $\square_{\square}$ operator (Extended Data Fig. 4). The prescribed damping rates are (5 day)$^{-1}$, (30 day)$^{-1}$, (90 day)$^{-1}$, (180 day)$^{-1}$, and (360 day)$^{-1}$, in the different experiments, ranging from strong damping (no memory) to less damping (long memory).

Deseasonalizing experiments.

We carried out deseasonalizing experiments to illustrate the role of the operator parameters' annual and semi-annual cycles in ENSO forecast skill (Supplementary Fig. 17). In the $\mathrm{XRO}_{\mathrm{ac=0}}$ model, we considered only the annual mean component ($\boldsymbol{L_0}$ and $\boldsymbol{N_0}$ in Eqs. 3-4, each tendency equation has ~10 parameters, a total number of parameters of $103 = 10 \times 10 + 3$). 10–15 years of data is required to meet the rule of thumb for regression sample size (at least 10 subjects per predictor) [78]. In the XRO$_{\text{ac=1}}$ model, we considered both the annual mean and annual cycle components in the operator ($\boldsymbol{L_0}$, $\boldsymbol{L_1^c}$, $\boldsymbol{L_1^s}$, $\boldsymbol{N_0}$, $\boldsymbol{N_1^c}$ and $\boldsymbol{N_1^s}$ in Eqs. 3-4, each tendency equation has ~30 parameters, the total number of parameters is $309 = 3 \times 100 + 3 \times 3$). At least 25 years of data is required [78]. The difference between XRO and XRO$_{\text{ac=0}}$ isolates the combined impacts of the annual and semi-annual cycles in the operator parameters, whereas the difference between XRO and XRO$_{\text{ac=1}}$ isolates the impact of just the semi-annual cycle in the operator parameters. The parameters for the XRO$_{\text{ac=0}}$, and XRO$_{\text{ac=1}}$ experiments can be either refitted separately (Supplementary Fig. 17a-d) or taken from the XRO control experiment (Supplementary Fig. 17e-h). Regardless which parameter estimation method is used, we find that the seasonal cycle is critically important in suppressing SPB for ENSO, while the semi-annual cycle is less important.

Removing nonlinearity experiments

We carried out "removing nonlinearity" experiments to illustrate the role of the XRO nonlinear operators in ENSO forecast skill (Supplementary Fig. 18). In the XRO$_{\text{linear}}$ experiment, we consider only linear operators and set $\boldsymbol{N}_{\text{ENSO}}$ and $\boldsymbol{N_M}$ to zero. In the XRO$_{\text{linearENSO}}$ experiment, we only consider linear operators and $\boldsymbol{N_M}$, but set $\boldsymbol{N}_{\text{ENSO}}$ to zero. In the XRO$_{\text{linearIOD}}$ experiment, we only consider linear operators and $\boldsymbol{N}_{\text{ENSO}}$, but set $\boldsymbol{N_M}$ to zero. The difference between XRO and XRO$_{\text{linear}}$ isolates the impact of the nonlinear operator parameters, whereas the difference between XRO and XRO$_{\text{linearENSO}}$ isolates the impact of the ENSO nonlinear operator parameters. The parameters for the XRO$_{\text{linear}}$, the XRO$_{\text{linearENSO}}$, and XRO$_{\text{linearIOD}}$ experiments can be either refitted separately (Supplementary Fig. 18a-d) or taken from the XRO control experiment (Supplementary Fig. 18e-h). Regardless which of method we use to obtain the parameters, we find that the ENSO nonlinear dynamics are critically important for ENSO forecast skill, especially for forecasting the amplitude of the peak phase and the fast transition from El Niño to La Niña. Further, we find that the impact of IOD's nonlinearity on ENSO forecast skill is neglectable.

Prediction skill metrics and significance tests

The forecast skill is quantified using the anomaly correlation coefficient (ACC) and root mean square error (RMSE) metrics[99]. The ACC is computed as the Pearson correlation coefficient between the deterministic forecast (f) and the observations (o):

$$ACC = \frac{cov(f, o)}{\sigma_f \cdot \sigma_o}, \tag{6}$$

and the RMSE is defined as

$$RMSE = \sqrt{\overline{(f - o)^2}}, \tag{7}$$

where σ_f and σ_o are the standard deviations of the observations and forecast, respectively.

The Fisher z-transformation was used to test statistical significance of the ACC differences as follows:

$$Z = 0.5 \frac{\ln\left(\frac{1+r_1}{1-r_1}\right) - \ln\left(\frac{1+r_2}{1-r_2}\right)}{\sqrt{\frac{1}{n_1-3} + \frac{1}{n_2-3}}}, \tag{8}$$

where r_1 and r_2 are the correlation coefficients, n_1 and n_2 are the sample sizes of the first and second group samples. The absolute value $|Z|$ is then compared against a critical value from the *t*-distribution for a two-tailed test. We rejected the null hypothesis that the two correlations are not significantly different at 90% confidence level if $|Z|$ exceeds the critical value.

The XRO reforecasting experiments based on CMIP model output

We analyse monthly mean SST and 3-dimensional ocean temperature fields from 91 CMIP5 and CMIP6 historical simulations (Supplementary Table 5). All model outputs were re-gridded to a common $1° \times 1°$ horizontal resolution using bilinear interpolation. The monthly anomaly fields were calculated by removing the monthly climatology for the period of 1900-1999 and the quadratically detrended over the full 100-year period.

Using the linear and nonlinear operators trained solely on CMIP model m output for 1900-1999, we conducted retrospective 21 months forecasts with initial conditions from the observations for the period of January 1982– October 2023 (referred to XRO^m). To understand the impacts of model biases on ENSO dynamics and its coupling with other modes, we also conducted sensitivity experiments by correcting the different components of the linear and nonlinear operators with the observed parameters (See Extended Data Table 2). For example, the experiment $\mathrm{XRO}_{\boldsymbol{L}}^m$ is the same as XRO^m, but with the linear operator $\boldsymbol{L}$ being replaced by the observed $\boldsymbol{L}$ operator. The difference $\mathrm{XRO}_{\boldsymbol{L}}^m - \mathrm{XRO}^m$ is used to isolate the effect of correcting model m's linear dynamics biases. Similarly, the experiments $\mathrm{XRO}_{\boldsymbol{L}_{\mathrm{ENSO}}}^m$, $\mathrm{XRO}_{\boldsymbol{C}_1}^m$, and $\mathrm{XRO}_{\boldsymbol{C}_2}^m$ were conducted to isolate the impacts of model m's biases on the internal linear ENSO dynamics, the coupling feedback to ENSO parameters, and ENSO teleconnection dynamics, respectively.

The XRO2 ENSO types and pantropical SSTA forecasts

The additional XRO model (referred to XRO2) was set up to predict different types of El Niño (i.e., ENSO diversity). We introduced two SSTA indices in the state vectors of ENSO, i.e., Niño3 index (SSTAs averaged over 150°–90°W, 5°S–5°N) and Niño4 index (SSTAs averaged over 160°E–150°W, 5°S–5°N): $\boldsymbol{X}_{\mathrm{ENSO}} = [T_{\mathrm{Nino3}}, T_{\mathrm{Nino4}}, h]$ instead of using Niño3.4. The quadratic nonlinearities $b_1 T_{\mathrm{Nino3}}^2 + b_2 T_{\mathrm{Nino3}} h$ are only incorporated into the SSTA equation of T_{Nino3}, in presence of the strong asymmetry of Niño3 index whereas the less pronounced asymmetry of Niño4 index: $\boldsymbol{N}_{\mathrm{ENSO}} = [b_1 T_{\mathrm{Nino3}}^2 + b_2 T_{\mathrm{Nino3}} h, 0, 0]$. All other terms are the same as the standard XRO model. Using the operator parameters estimated from the ORAS5 reanalysis for 1979-2022, we conducted similar retrospective 21-month forecasts for the period of January 1979–October 2023. The hindcast skills of Niño3 and Niño4 indices are better than those from the NMME dynamical models and comparable to the AI model. The forecasts of Niño3 and Niño4 indices were used to define the El Niño types in terms of the EP-type, CP-type, and mixed-type, following [100,8]. The unified complex ENSO index (UCEI) is defined as

$$UCEI = (N_3 + N_4) + (N_3 - N_4)i = re^{\theta i}, \tag{9}$$

where

$$r = \sqrt{(N_3 + N_4)^2 + (N_3 - N_4)^2}, \tag{10}$$

and

$$\theta = \begin{cases} \arctan \dfrac{N_3 - N_4}{N_3 + N_4} & when\ N_3 + N_4 > 0 \\ \arctan \dfrac{N_3 - N_4}{N_3 + N_4} - \pi & when\ N_3 + N_4 < 0 \end{cases} \tag{11}$$

where N_3 and N_4 denote the Niño3 and Niño4 indices, respectively; The El Niño type is determined from θ as follows:

$$\left\{ \begin{array}{ll} 15° \leq \theta < 90° & EP\ El\ Nino \\ -15° \leq \theta < 15° & Mixed\ El\ Nino \\ -90° \leq \theta < -15° & CP\ El\ Nino \end{array} \right\}. \tag{12}$$

We also conducted out-of-sample XRO2 ENSO type reforecasts by fitting on 1950-1990 with the multi-products ensemble mean indices and verifying on 1991-2022 (Supplementary Table 3).

With the forecasted ten SSTA indices, the pantropical SSTA (30°S-30°N) at each grid point ($SSTA_j$) can be predicted using the seasonal regression model:

$$\mathrm{SSTA_j} = c_0\boldsymbol{X} + A_c\boldsymbol{X}\cos\omega t + A_s\boldsymbol{X}\sin\omega t + B_c\boldsymbol{X}\cos 2\omega t + B_s\boldsymbol{X}\sin 2\omega t\,, \qquad (13)$$

where c_0, A_c, A_s, B_c, and B_s have ten coefficients associated with each SSTA index, respectively. We also conducted the cross-validated XRO2 forecasts and pantropical SSTA forecast by excluding 3-year data out and trained XRO2 operators and SSTA regression coefficients, then forecasts for each month during the years not included in the model fitting.

Further details are provided in the Supplementary Information, relying on references[101-113].

Data availability

Datasets used in this paper are freely available. Observational data: links in Supplementary Table 2. NMME: https://iridl.ldeo.columbia.edu/SOURCES/.Models/.NMME/; 3D-Geoformer ENSO AI model forecast: http://msdc.qdio.ac.cn/data/metadata-special-detail?id=1602252663859298305; CESM1 LENS: https://www.cesm.ucar.edu/community-projects/lens/data-sets; CESM2 LENS: https://www.cesm.ucar.edu/community-projects/lens2/data-sets; MPI-ESM LENS: https://esgf-data.dkrz.de/projects/mpi-ge/; CMIP5 outputs: https://esgf-node.llnl.gov/projects/cmip5/; and MIROC6 LENS and CMIP6 outputs: https://esgf-node.llnl.gov/projects/cmip6/. All the map figures (Fig. 1a,c,d, and Supplementary Figs. 1, 2, 14) were generated using python Cartopy version 0.22.0 (https://zenodo.org/records/8216315). The source data for figures in the main text is available at https://doi.org/10.5281/zenodo.10951443.

Code availability

The XRO model code is deposited at https://doi.org/10.5281/zenodo.10681114. The code to calculate the predictive skill is available at https://github.com/pangeo-data/climpred.

Method References

51. Jin, F.-F. *et al.* Simple ENSO Models. in *El Niño Southern Oscillation in a Changing Climate* (eds. McPhaden, M. J., Santoso, A. & Cai, W.) 119–151 (American Geophysical Union (AGU), 2020).
52. Jin, F.-F. An equatorial ocean recharge paradigm for ENSO. Part I: conceptual model. *J. Atmos. Sci.* **54**, 811–829 (1997).
53. Hasselmann, K. Stochastic climate models Part I. Theory. *Tellus* **28**, 473–485 (1976).
54. Frankignoul, C. & Hasselmann, K. Stochastic climate models, Part II Application to sea-surface temperature anomalies and thermocline variability. *Tellus* **29**, 289–305 (1977).
55. Stuecker, M. F. The climate variability trio: stochastic fluctuations, El Niño, and the seasonal cycle. *Geoscience Letters* **10**, 51 (2023).
56. Meinen, C. S. & McPhaden, M. J. Observations of Warm Water Volume Changes in the Equatorial Pacific and Their Relationship to El Niño and La Niña. *J. Climate* **13**, 3551–3559 (2000).
57. Richter, I., Stuecker, M. F., Takahashi, N. & Schneider, N. Disentangling the North Pacific Meridional Mode from tropical Pacific variability. *npj Clim Atmos Sci* **5**, 1–9 (2022).
58. Klein, S. A., Soden, B. J. & Lau, N. C. Remote sea surface temperature variations during ENSO: Evidence for a tropical atmospheric bridge. *J. Climate* **12**, 917–932 (1999).
59. Xie, S.-P. *et al.* Indian Ocean capacitor effect on Indo-Western Pacific climate during the summer following El Niño. *J. Climate* **22**, 730–747 (2009).
60. Saji, N. H., Goswami, B. N., Vinayachandran, P. N. & Yamagata, T. A dipole mode in the tropical Indian Ocean. *Nature* **401**, 360–363 (1999).
61. Webster, P. J., Moore, A. M., Loschnigg, J. P. & Leben, R. R. Coupled ocean–atmosphere dynamics in the Indian Ocean during 1997–98. *Nature* **401**, 356–360 (1999).
62. Enfield, D. B. & Mayer, D. A. Tropical Atlantic sea surface temperature variability and its relation to El Nino Southern Oscillation. *J. Geophys. Res.-Oceans* **102**, 929–945 (1997).
63. Zebiak, S. Air-Sea Interaction in the Equatorial Atlantic Region. *J. Clim.* **6**, 1567–1568 (1993).
64. Nnamchi, H. C. *et al.* Thermodynamic controls of the Atlantic Niño. *Nature Communications* **6**, 8895 (2015).
65. Rodrigues, R. R., Campos, E. J. D. & Haarsma, R. The Impact of ENSO on the South Atlantic Subtropical Dipole Mode. *Journal of Climate* **28**, 2691–2705 (2015).
66. Jin, F.-F., Kim, S. T. & Bejarano, L. A coupled-stability index for ENSO. *Geophysical Research Letters* **33**, (2006).
67. An, S.-I., Tziperman, E., Okumura, Y. M. & Li, T. ENSO Irregularity and Asymmetry. in *El Niño Southern Oscillation in a Changing Climate* 153–172 (American Geophysical Union (AGU), 2020). doi:10.1002/9781119548164.ch7.
68. An, S.-I. & Jin, F.-F. Nonlinearity and Asymmetry of ENSO. *J. Climate* **17**, 2399–2412 (2004).

69. Kang, I.-S. & Kug, J.-S. El Niño and La Niña sea surface temperature anomalies: Asymmetry characteristics associated with their wind stress anomalies. *Journal of Geophysical Research: Atmospheres* **107**, ACL 1-1-ACL 1-10 (2002).

70. Choi, K.-Y., Vecchi, G. A. & Wittenberg, A. T. ENSO Transition, Duration, and Amplitude Asymmetries: Role of the Nonlinear Wind Stress Coupling in a Conceptual Model. *J. Climate* **26**, 9462–9476 (2013).

71. Geng, T., Cai, W. & Wu, L. Two Types of ENSO Varying in Tandem Facilitated by Nonlinear Atmospheric Convection. *Geophysical Research Letters* **47**, e2020GL088784 (2020).

72. An, S.-I. *et al.* Main drivers of Indian Ocean Dipole asymmetry revealed by a simple IOD model. *npj Clim Atmos Sci* **6**, 1–7 (2023).

73. Lübbecke, J. F. & McPhaden, M. J. Symmetry of the Atlantic Niño mode. *Geophysical Research Letters* **44**, 965–973 (2017).

74. Gebbie, G., Eisenman, I., Wittenberg, A. & Tziperman, E. Modulation of Westerly Wind Bursts by Sea Surface Temperature: A Semistochastic Feedback for ENSO. *J. Atmos. Sci.* **64**, 3281–3295 (2007).

75. Jin, F.-F., Lin, L., Timmermann, A. & Zhao, J. Ensemble-mean dynamics of the ENSO recharge oscillator under state-dependent stochastic forcing. *Geophysical Research Letters* **34**, (2007).

76. Zhao, S., Jin, F.-F. & Stuecker, M. F. Improved Predictability of the Indian Ocean Dipole Using Seasonally Modulated ENSO Forcing Forecasts. *Geophys. Res. Lett.* **46**, 9980–9990 (2019).

77. Chen, H.-C. & Jin, F.-F. Simulations of ENSO Phase-Locking in CMIP5 and CMIP6. *Journal of Climate* **34**, 5135–5149 (2021).

78. Harrell, F. E. Regression Modeling Strategies: With Applications to Linear Models, Logistic Regression, and Survival Analysis. (Springer, New York, NY, 2001). doi:10.1007/978-1-4757-3462-1.

79. Vimont, D. J. Analysis of the Atlantic Meridional Mode Using Linear Inverse Modeling: Seasonality and Regional Influences. *Journal of Climate* **25**, 1194–1212 (2012).

80. Zhao, Y., Jin, Y., Li, J. & Capotondi, A. The Role of Extratropical Pacific in Crossing ENSO Spring Predictability Barrier. *Geophysical Research Letters* **49**, e2022GL099488 (2022).

81. Rayner, N. A. *et al.* Global analyses of sea surface temperature, sea ice, and night marine air temperature since the late nineteenth century. *Journal of Geophysical Research: Atmospheres* **108**, (2003).

82. Huang, B. *et al.* Extended Reconstructed Sea Surface Temperature, Version 5 (ERSSTv5): Upgrades, Validations, and Intercomparisons. *Journal of Climate* **30**, 8179–8205 (2017).

83. Hirahara, S., Ishii, M. & Fukuda, Y. Centennial-Scale Sea Surface Temperature Analysis and Its Uncertainty. *Journal of Climate* **27**, 57–75 (2014).

84. Köhl, A. Evaluating the GECCO3 1948–2018 ocean synthesis – a configuration for initializing the MPI-ESM climate model. *Quarterly Journal of the Royal Meteorological Society* **146**, 2250–2273 (2020).

85. Behringer, D. & Xue, Y. Evaluation of the global ocean data assimilation system at NCEP: The Pacific Ocean. in *Eighth Symposium on Integrated Observing and Assimilation Systems for Atmosphere, Oceans, and Land Surface* vol. 2.3 11–15 (Washington, 2004).

86. Zuo, H., Balmaseda, M. A., Tietsche, S., Mogensen, K. & Mayer, M. The ECMWF operational ensemble reanalysis–analysis system for ocean and sea ice: a description of the system and assessment. *Ocean Science* **15**, 779–808 (2019).

87. de Boisséson, E., Balmaseda, M. A. & Mayer, M. Ocean heat content variability in an ensemble of twentieth century ocean reanalyses. *Clim Dyn* **50**, 3783–3798 (2018).

88. Yin, Y., Alves, O. & Oke, P. R. An Ensemble Ocean Data Assimilation System for Seasonal Prediction. *Mon. Wea. Rev.* **139**, 786–808 (2011).

89. Carton, J. A. & Giese, B. S. A Reanalysis of Ocean Climate Using Simple Ocean Data Assimilation (SODA). *Mon. Wea. Rev.* **136**, 2999–3017 (2008).

90. Hersbach, H. *et al.* The ERA5 global reanalysis. *Quarterly Journal of the Royal Meteorological Society* **146**, 1999–2049 (2020).

91. Xie, P. P. & Arkin, P. A. Global precipitation: A 17-year monthly analysis based on gauge observations, satellite estimates, and numerical model outputs. *Bull. Amer. Meteor. Soc.* **78**, 2539–2558 (1997).

92. Kirtman, B. P. *et al.* The North American Multimodel Ensemble: Phase-1 Seasonal-to-Interannual Prediction; Phase-2 toward Developing Intraseasonal Prediction. *Bull. Amer. Meteor. Soc.* **95**, 585–601 (2014).

93. Mu, B., Qin, B. & Yuan, S. ENSO-ASC 1.0.0: ENSO deep learning forecast model with a multivariate air–sea coupler. *Geoscientific Model Development* **14**, 6977–6999 (2021).

94. Gao, C., Zhou, L. & Zhang, R.-H. A Transformer-Based Deep Learning Model for Successful Predictions of the 2021 Second-Year La Niña Condition. *Geophysical Research Letters* **50**, e2023GL104034 (2023).

95. Kay, J. E. *et al.* The Community Earth System Model (CESM) Large Ensemble Project: A Community Resource for Studying Climate Change in the Presence of Internal Climate Variability. *Bulletin of the American Meteorological Society* **96**, 1333–1349 (2015).

96. Rodgers, K. B. *et al.* Ubiquity of human-induced changes in climate variability. *Earth System Dynamics* **12**, 1393–1411 (2021).

97. Shiogama, H. *et al.* MIROC6 Large Ensemble (MIROC6-LE): experimental design and initial analyses. *Earth System Dynamics* **14**, 1107–1124 (2023).

98. Maher, N. *et al.* The Max Planck Institute Grand Ensemble: Enabling the Exploration of Climate System Variability. *Journal of Advances in Modeling Earth Systems* **11**, 2050–2069 (2019).

99. Brady, R. X. & Spring, A. climpred: Verification of weather and climate forecasts. *Journal of Open Source Software* **6**, 2781 (2021).

100. Zhang, Z., Ren, B. & Zheng, J. A unified complex index to characterize two types of ENSO simultaneously. *Sci Rep* **9**, 8373 (2019).

101. Stein, K., Timmermann, A., Schneider, N., Jin, F.-F. & Stuecker, M. F. ENSO Seasonal Synchronization Theory. *J. Climate* **27**, 5285–5310 (2014).

102. Levine, A. F. Z. & McPhaden, M. J. The annual cycle in ENSO growth rate as a cause of the spring predictability barrier. *Geophysical Research Letters* **42**, 5034–5041 (2015).

103. Zhao, S., Jin, F.-F. & Stuecker, M. F. Understanding Lead Times of Warm Water Volumes to ENSO Sea Surface Temperature Anomalies. *Geophysical Research Letters* **48**, e2021GL094366 (2021).

104. Okumura, Y. M., Ohba, M., Deser, C. & Ueda, H. A Proposed Mechanism for the Asymmetric Duration of El Niño and La Niña. *Journal of Climate* **24**, 3822–3829 (2011).

105. DiNezio, P. N. & Deser, C. Nonlinear Controls on the Persistence of La Niña. *J. Climate* **27**, 7335–7355 (2014).

106. Iwakiri, T. & Watanabe, M. Mechanisms linking multi-year La Niña with preceding strong El Niño. *Sci Rep* **11**, 17465 (2021).

107. Iwakiri, T. & Watanabe, M. Multiyear ENSO Dynamics as Revealed in Observations, Climate Model Simulations, and the Linear Recharge Oscillator. *Journal of Climate* **35**, 7625–7642 (2022).

108. Kim, J.-W., Yu, J.-Y. & Tian, B. Overemphasized role of preceding strong El Niño in generating multi-year La Niña events. *Nat Commun* **14**, 6790 (2023).

109. Kim, J.-W. & Yu, J.-Y. Single- and multi-year ENSO events controlled by pantropical climate interactions. *npj Clim Atmos Sci* **5**, 1–11 (2022).

110. Chen, H.-C., Jin, F.-F. & Jiang, L. The Phase-Locking of Tropical North Atlantic and the Contribution of ENSO. *Geophysical Research Letters* **48**, e2021GL095610 (2021).

111. Jiang, F. *et al.* Resolving the Tropical Pacific/Atlantic Interaction Conundrum. *Geophysical Research Letters* **50**, e2023GL103777 (2023).

112. Trenberth, K. E. The Definition of El Niño. *Bulletin of the American Meteorological Society* **78**, 2771–2778 (1997).

113. Enfield, D. B., Mestas-Nuñez, A. M., Mayer, D. A. & Cid-Serrano, L. How ubiquitous is the dipole relationship in tropical Atlantic sea surface temperatures? *Journal of Geophysical Research: Oceans* **104**, 7841–7848 (1999).

Acknowledgments

SZ and FFJ were supported by the U.S. National Science Foundation (NSF) grant AGS-2219257 and NOAA's Climate Program Office's Modeling, Analysis, Predictions, and Projections (MAPP)

Program grant NA23OAR2007440. MFS was supported by NSF grant AGS-2141728. MFS and SZ were supported by NOAA's Climate Program Office's MAPP program grant NA20OAR4310445. JSK was supported by the National Research Foundation of Korea grant funded by the Korean government (NRF-2022R1A3B1077622). MAC was supported by NSF award OCE-2219829. This is IPRC publication XXX, SOEST contribution YYY, and PMEL contribution 5579.

Author contributions

FFJ, SZ, and MFS conceptualized the research. SZ designed the model and experiments, conducted the analysis, produced the figures, and wrote the initial manuscript, in discussion with FFJ. FFJ, WC, MFS, and SZ structured the paper. ATW, MFS, and SZ designed the LENS perfect model experiments. MAC coined the acronym "XRO". All authors contributed to interpreting the results and improving the paper.

Competing interests

The authors declare no competing interests.

Additional information

Supplementary information: The online version contains supplementary material available at X

Correspondence and requests for materials should be addressed to Fei-Fei Jin.

Extended Data Legends

Extended Data Fig. 1| Seasonally-modulated strength of mode interactions in observations and CMIP5/6 models, as diagnosed from the linear part of the XRO model. (a) ENSO recharge-oscillator coefficients, (b) Coupling processes denoted by the contribution of other modes to the tendencies of ENSO SSTA and WWV anomalies, (c) ENSO-forced processes denoted by the contribution of ENSO SSTA and WWV anomalies to the SSTA tendency of other modes, (d) Interactions among NPMM, SPMM, IOB, IOD, SIOD, TNA, ATL3, and SASD. The coefficient L_{ij} has been normalized by a factor of σ_j/σ_i, where σ_i and σ_j are the monthly standard deviations of the indices in row i and column j, respectively, so that all coefficients are comparable, and the units are year^{-1}. The diagonal panels (*blue frames*) show the damping rate for each index. The black curves with shading show the XRO fit to the ORAS5 reanalysis (with 10%-90% spread band from the cross-validated fitting excluding 3-year data, see *"Cross-validated reforecasts" in Methods*), and the red curves with shading show the ensemble mean with 10%-90% spread band of the 91 CMIP5/6 historical simulations. ENSO can be strongly driven by climate modes in extratropical Pacific, Indian Ocean, and Atlantic Ocean, which in some seasons are as important as the dynamics internal to the equatorial Pacific. Most of the non-ENSO modes are more strongly driven by ENSO (and their own damping) than by any of the other non-ENSO modes in other basins. The climate models underestimate the strength of most of the mode interactions and miss the seasonality.

Extended Data Fig. 2| Decadal change in the ENSO forecast correlation skill. a, The all-months correlation skill of the 3-month running mean Niño3.4 index verified on 1950-1970 for the out-of-sample XRO fitted on 1973-2022 (*red curve*), out-of-sample nRO fitted on 1973-2022 (*magenta curve*), in-sample XRO fitted on 1950-1970 (*black dashed curve*) and in-sample XRO fitted on the full-period 1950-2022 (*blue dashed curve*). The bottom inset shows the time series of Niño3.4 index for out-of-sample training (*blue*) and verifying (*orange*) periods, respectively. **b-c**, same as **a**, but verifying on 1972-1992 and 2002-2022, respectively. The XRO is superior to the nRO regardless the verifying periods and decadal changes of ENSO forecast skill.

Extended Data Fig. 3| Test of additivity (i.e., linearity) of the sensitivity experiments. a, Regression slope and linear correlation coefficients for the Niño3.4 SSTA forecasts between the effects of the uninitialized ExPO+IO+AO experiment ($\mathrm{XRO} - U_{\mathrm{ExPO+IO+AO}}$) and the sum of the effects of the individual uninitialized ExPO, IO, and AO experiments ($3 * \mathrm{XRO} - U_{\mathrm{ExPO}} - U_{\mathrm{IO}} - U_{\mathrm{AO}}$). **b** and **c,** same as **a**, but for decoupling experiments ($\mathrm{XRO} - D_{\mathrm{ExPO+IO+AO}}$ vs. $3 * \mathrm{XRO} - D_{\mathrm{ExPO}} - D_{\mathrm{IO}} - D_{\mathrm{AO}}$) and relaxing towards observation experiments ($\mathrm{XRO} - R_{\mathrm{ExPO+IO+AO}}$ vs. $3 * \mathrm{XRO} - R_{\mathrm{ExPO}} - R_{\mathrm{IO}} - R_{\mathrm{AO}}$), respectively. **d, e** the all-months correlation skill (d) and RMSE (e) of the 3-month running mean Niño3.4 index, as a function of the forecast lead month in the control experiment (*black line*) and sensitivity experiments: the uninitialized ExPO+IO+AO experiment (*solid red line*) and sum of uninitialized ExPO, IO, and AO individually (*dashed red line*), the decoupling ExPO+IO+AO experiment (*solid blue line*) and sum of decoupling ExPO, IO, and AO individually (*dashed blue line*), and the relaxing ExPO+IO+AO to observation experiment (*solid magenta line*) and sum of relaxing ExPO, IO, and AO to observation individually (*dashed magenta line*). The individual basin uninitialized experiments are additive with the slopes and correlations at all lead months being very close to 1. But the individual basin decoupling experiments and the individual relaxation towards observations experiments are not additive, owing to a nonlinear dependence on the operator parameters. The sum of the effects of decoupling ExPO, IO, and AO individually is much larger than the effect of decoupling ExPO+IO+AO, suggesting that the decoupling experiment framework overestimates the contribution of each basin, given the presence of indirect pathways due to interactions among basins.

Extended Data Fig. 4| Influence of the memory effect outside the equatorial Pacific on ENSO forecast skill. Shown are the all-months correlation skill (a) and RMSE (b) of the 3-month running mean Niño3.4 index, as a function of the forecast lead month in the XRO forecast (*black*), the nRO forecast (*grey triangle*), and the "Losing memory" sensitivity experiments (*colour curves*) by adding different damping rates (ranging from a strong damping rate of $-(5\ \text{day})^{-1}$ implying no memory to a weak damping rate of $-(360\ \text{day})^{-1}$ implying longer memory) to the non-ENSO modes (See *"Losing memory experiments" in Methods*). The initial condition memory effect of the climate modes outside equatorial Pacific extends the skill of ENSO forecasts.

Extended Data Fig. 5| Contribution of each climate mode's initialization to ENSO correlation skill. Shown is the forecast skill difference of the Niño3.4 SSTA index, as a function of initial time and target month, between the control and uninitialized climate mode sensitivity experiments for the NPMM, SPMM, IOB, IOD, SIOD, TNA, ATL3, and SASD, respectively. The contributions of the IOD, NPMM, and TNA dominate the ENSO forecast skill improvement.

Extended Data Fig. 6| Impacts of climate-mode initialization to ENSO forecasts. Shown is the difference of Niño3.4 SSTA (shading) and WWV anomalies (contours with interval of 0.6 m, positive in red and negative in black dashed, zero omitted), as a function of forecast lead and target time, between control and uninitialized climate mode experiments for NPMM, SPMM, IOB, IOD, SIOD, TNA, ATL3, and SASD, respectively. Vertical reference dashed lines denote December of El Niño (red) and La Niña (blue) years, respectively. The normalized time series of each climate mode SSTA index is indicated in the bottom axis; the black arrows indicate the flow of forecast integration started from the selected time in the bottom. The XRO sensitivity experiments quantify how the initial states of key climate modes affect subsequent ENSO events.

Extended Data Fig. 7| Impacts on ENSO forecast skill of correcting biases in the XRO parameters fitted to individual CMIP simulations. Shown is the difference of the all-months correlation skill for the Niño3.4 SSTA index, between the corrected-parameter forecast experiment and the XRO^{m} experiment trained solely on CMIP model outputs. (a) Effect of correcting linear operators (XRO$^{m}_{\boldsymbol{L}}$- XRO^{m}), (b) effect of correcting ENSO internal linear dynamics (XRO$^{m}_{\boldsymbol{L}_{\mathrm{ENSO}}}$- XRO^{m}), (c) effect of correcting remote climate mode feedbacks onto ENSO (XRO$^{m}_{\boldsymbol{C}_1}$- XRO^{m}), and (d) effect of correcting ENSO teleconnections to remote climate modes (XRO$^{m}_{\boldsymbol{C}_2}$- XRO^{m}). The model is sorted by the averaged correlation skill of the XRO^{m} forecast at 6-15 lead months. Reforecasts using the XRO trained on global climate model output show that correcting CGCMs' dynamical biases in ENSO and climate mode interactions lead to more skilful ENSO forecasts. Most important is correcting ENSO biases (which improves skill at longest lead-times), followed by correcting the remote climate mode impact on ENSO (which improves skill at intermediate leads). Less skill is gained by improving ENSO's teleconnection to the remote modes.

Extended Data Fig. 8| Correlation forecast skill for the Indian Ocean Dipole, using the XRO trained with climate model outputs. (a) The correlation skill of the IOD index in Sep-Oct-Nov (SON) as a function of forecast lead, in the XRO^{m} trained solely on 91 individual CMIP model outputs (grey curves), the XRO trained on observations (red curve), and the original (not XRO) multi-model mean of the ensemble means of the forecasts from the NMME models (black). (b) the ensemble mean and 10%-90% spread band of the changes in correlation skill for the IOD index, obtained by correcting the ENSO internal linear dynamics (XRO$^{m}_{\boldsymbol{L}_{\mathrm{ENSO}}}$- XRO^{m}, *red*), or the remote-mode feedbacks onto ENSO (XRO$^{m}_{\boldsymbol{C}_1}$- XRO^{m}, *magenta*), or the ENSO teleconnections to remote modes (XRO$^{m}_{\boldsymbol{C}_2}$- XRO^{m}, *blue*). Reforecasts using the XRO trained on climate model output show that reducing CGCM biases in the dynamics of ENSO's climate mode interactions improves IOD forecasts.

Extended Data Table 1| Details of the XRO forecasting experiments based on observations (1979-2022).

Extended Data Table 2| Details of the XRO forecasting experiments using global climate model output as training data.

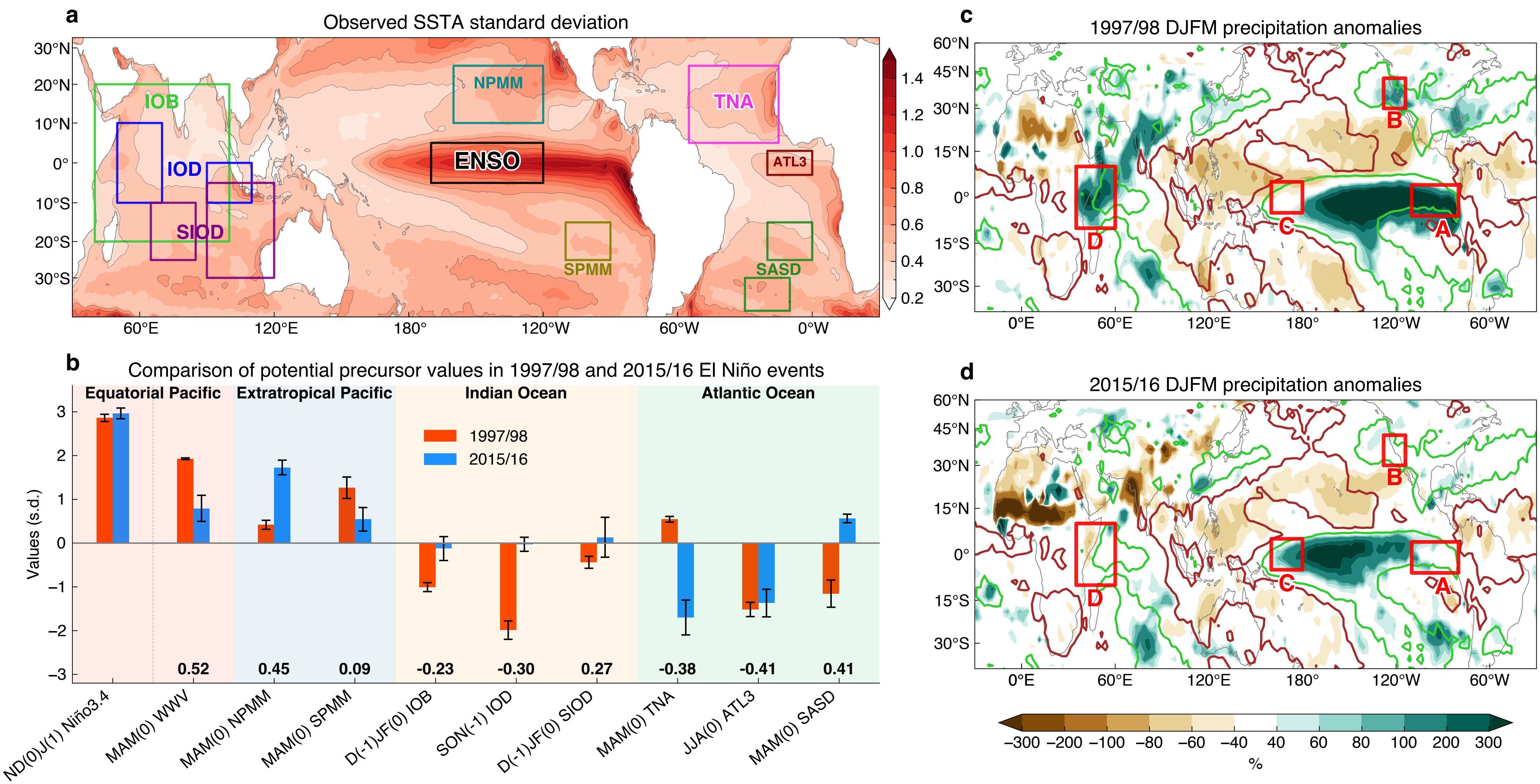
a
Observed SSTA standard deviation
IOB
IOD
SIOD
NPMM
ENSO
SPMM
TNA
ATL3
SASD
b
Comparison of potential precursor values in 1997/98 and 2015/16 El Niño events
Equatorial Pacific
Extratropical Pacific
Indian Ocean
Atlantic Ocean
1997/98
2015/16
Values (s.d.)
0.52
0.45
0.09
-0.23
-0.30
0.27
-0.38
-0.41
0.41
ND(0)J(1) Niño3.4
MAM(0) WWV
MAM(0) NPMM
MAM(0) SPMM
D(-1)JF(0) IOB
SON(-1) IOD
D(-1)JF(0) SIOD
MAM(0) TNA
JJA(0) ATL3
MAM(0) SASD
c
1997/98 DJFM precipitation anomalies
d
2015/16 DJFM precipitation anomalies
A
B
C
D
%

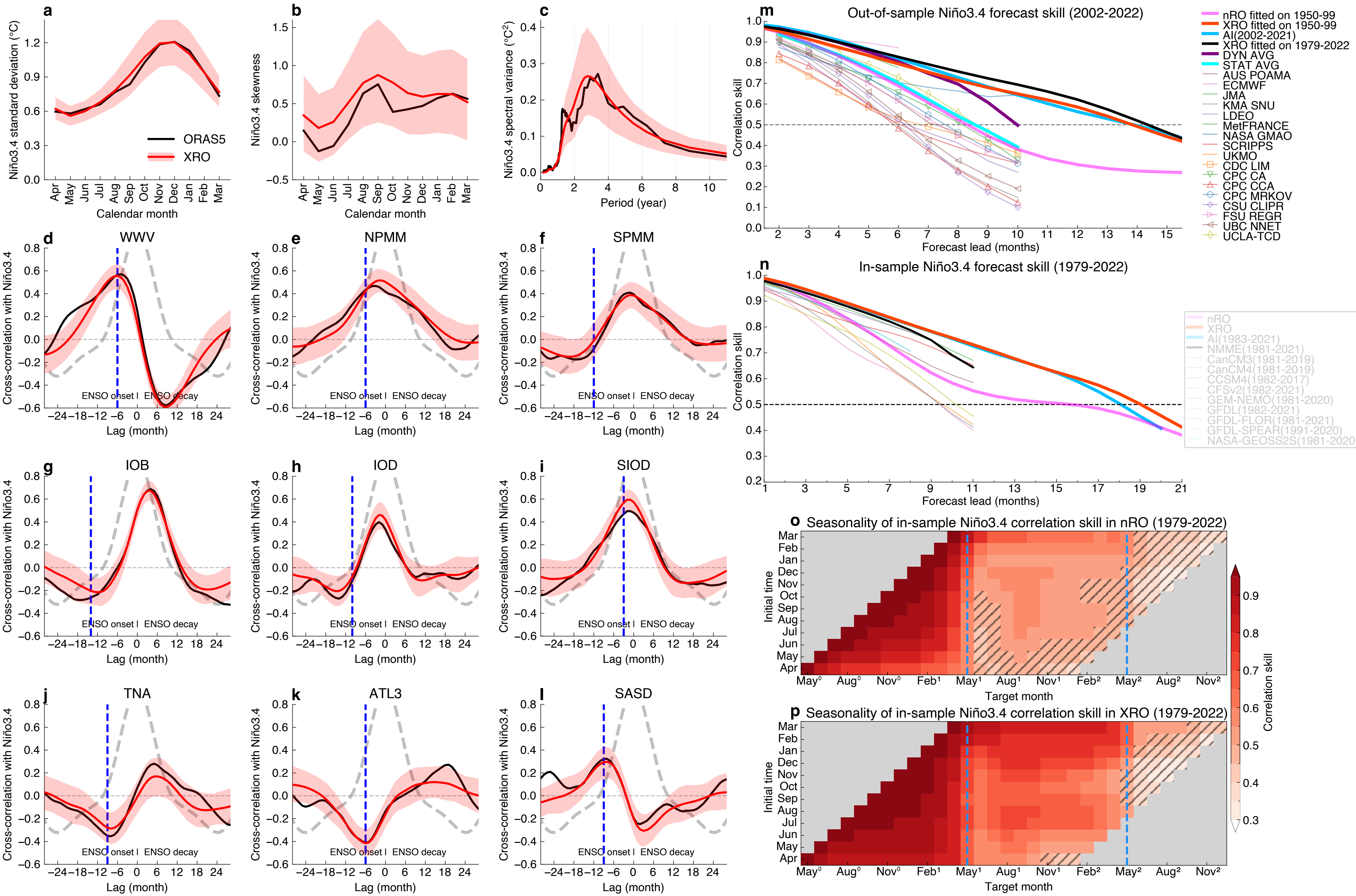
a
Niño3.4 standard deviation (°C)
Calendar month
ORAS5
XRO
b
Niño3.4 skewness
Calendar month
c
Niño3.4 spectral variance (°C²)
Period (year)
d WWV
e NPMM
f SPMM
g IOB
h IOD
i SIOD
j TNA
k ATL3
l SASD
Cross-correlation with Niño3.4
Lag (month)
ENSO onset | ENSO decay
m Out-of-sample Niño3.4 forecast skill (2002-2022)
Correlation skill
Forecast lead (months)
nRO fitted on 1950-99
XRO fitted on 1950-99
AI(2002-2021)
XRO fitted on 1979-2022
DYN AVG
STAT AVG
AUS POAMA
ECMWF
JMA
KMA SNU
LDEO
MetFRANCE
NASA GMAO
SCRIPPS
UKMO
CDC LIM
CPC CA
CPC CCA
CPC MRKOV
CSU CLIPR
FSU REGR
UBC NNET
UCLA-TCD
n In-sample Niño3.4 forecast skill (1979-2022)
Correlation skill
Forecast lead (months)
nRO
XRO
AI(1983-2021)
NMME(1981-2021)
CanCM3(1981-2019)
CanCM4(1981-2019)
CCSM4(1982-2017)
CFSv2(1982-2021)
GEM-NEMO(1981-2020)
GFDL(1982-2021)
GFDL-FLOR(1981-2021)
GFDL-SPEAR(1991-2020)
NASA-GEOSS2S(1981-2020)
o Seasonality of in-sample Niño3.4 correlation skill in nRO (1979-2022)
p Seasonality of in-sample Niño3.4 correlation skill in XRO (1979-2022)
Initial time
Target month
Correlation skill

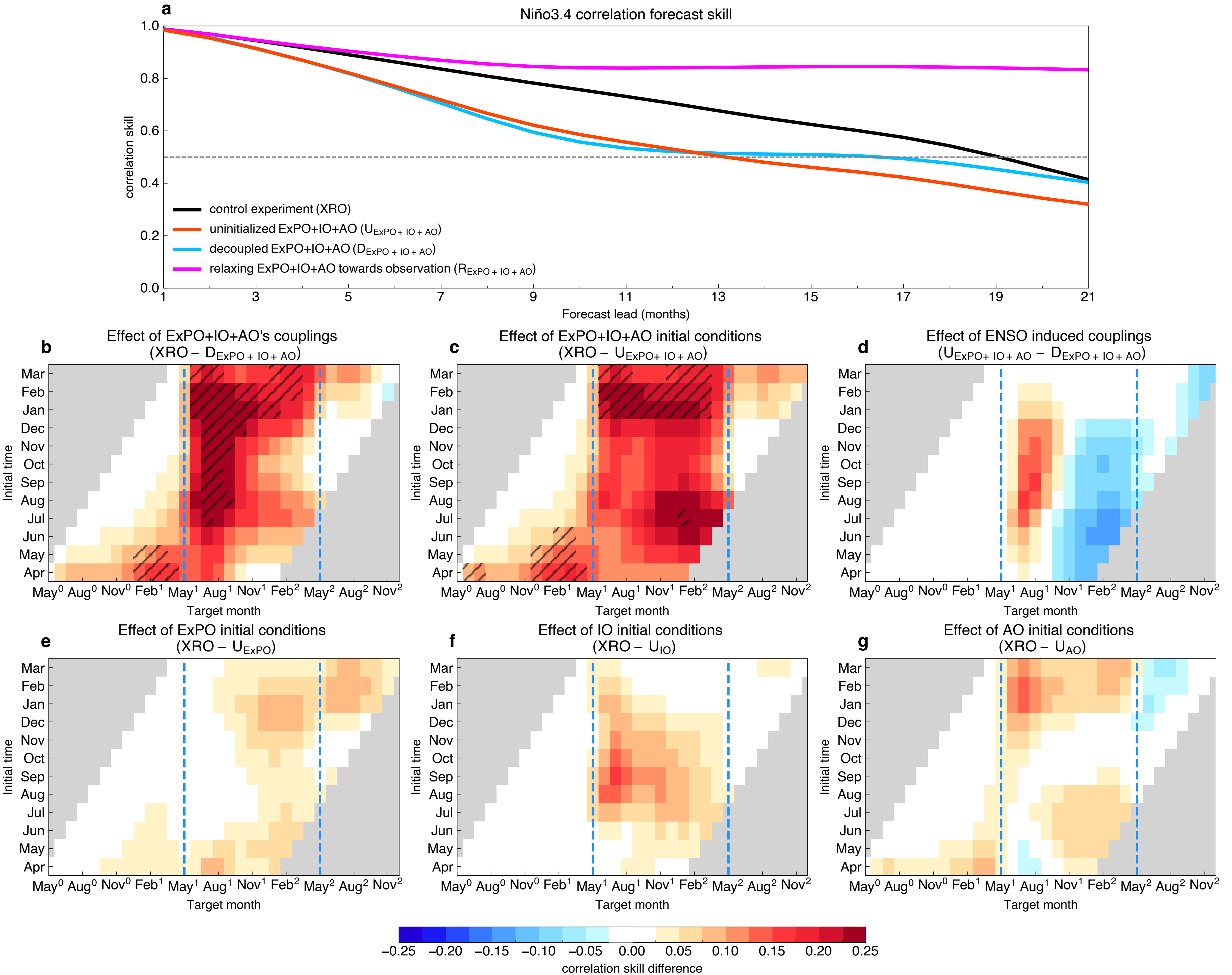

a
Niño3.4 correlation forecast skill
correlation skill
Forecast lead (months)
control experiment (XRO)
uninitialized ExPO+IO+AO ($U_{ExPO+IO+AO}$)
decoupled ExPO+IO+AO ($D_{ExPO+IO+AO}$)
relaxing ExPO+IO+AO towards observation ($R_{ExPO+IO+AO}$)
b
Effect of ExPO+IO+AO's couplings
($XRO - D_{ExPO+IO+AO}$)
c
Effect of ExPO+IO+AO initial conditions
($XRO - U_{ExPO+IO+AO}$)
d
Effect of ENSO induced couplings
($U_{ExPO+IO+AO} - D_{ExPO+IO+AO}$)
e
Effect of ExPO initial conditions
($XRO - U_{ExPO}$)
f
Effect of IO initial conditions
($XRO - U_{IO}$)
g
Effect of AO initial conditions
($XRO - U_{AO}$)
Initial time
Target month
correlation skill difference

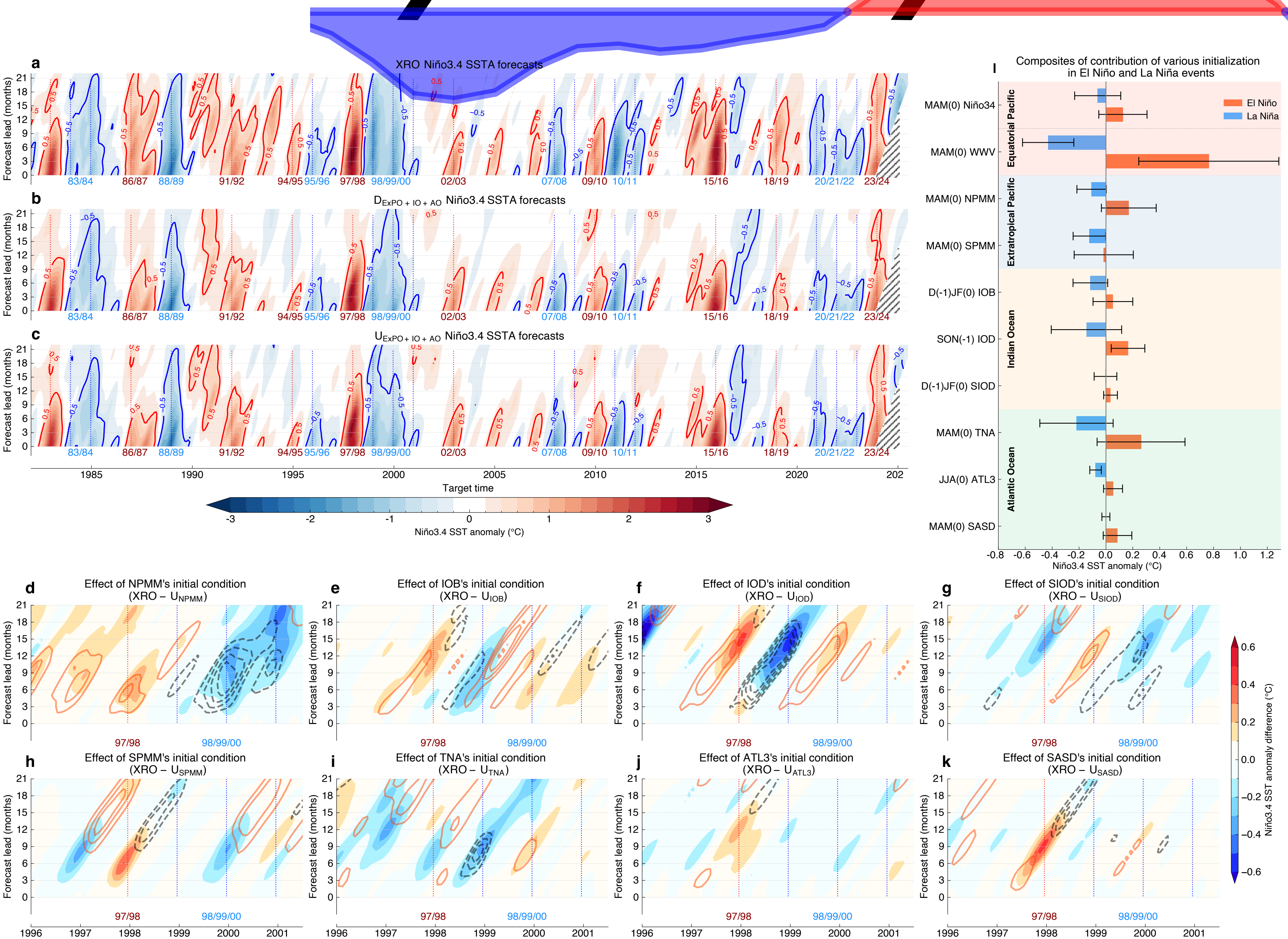

a
XRO Niño3.4 SSTA forecasts
b
D$_{ExPO + IO + AO}$ Niño3.4 SSTA forecasts
c
U$_{ExPO + IO + AO}$ Niño3.4 SSTA forecasts
Forecast lead (months)
83/84
86/87
88/89
91/92
94/95
95/96
97/98
98/99/00
02/03
07/08
09/10
10/11
15/16
18/19
20/21/22
23/24
1985
1990
1995
2000
2005
2010
2015
2020
202
Target time
-3
-2
-1
0
1
2
3
Niño3.4 SST anomaly (°C)
l
Composites of contribution of various initialization in El Niño and La Niña events
El Niño
La Niña
Equatorial Pacific
Extratropical Pacific
Indian Ocean
Atlantic Ocean
MAM(0) Niño34
MAM(0) WWV
MAM(0) NPMM
MAM(0) SPMM
D(-1)JF(0) IOB
SON(-1) IOD
D(-1)JF(0) SIOD
MAM(0) TNA
JJA(0) ATL3
MAM(0) SASD
-0.8
-0.6
-0.4
-0.2
0.0
0.2
0.4
0.6
0.8
1.0
1.2
Niño3.4 SST anomaly (°C)
d
Effect of NPMM's initial condition
(XRO – U$_{NPMM}$)
e
Effect of IOB's initial condition
(XRO – U$_{IOB}$)
f
Effect of IOD's initial condition
(XRO – U$_{IOD}$)
g
Effect of SIOD's initial condition
(XRO – U$_{SIOD}$)
h
Effect of SPMM's initial condition
(XRO – U$_{SPMM}$)
i
Effect of TNA's initial condition
(XRO – U$_{TNA}$)
j
Effect of ATL3's initial condition
(XRO – U$_{ATL3}$)
k
Effect of SASD's initial condition
(XRO – U$_{SASD}$)
1996
1997
1998
1999
2000
2001
Niño3.4 SST anomaly difference (°C)
0.6
0.4
0.2
0.0
−0.2
−0.4
−0.6

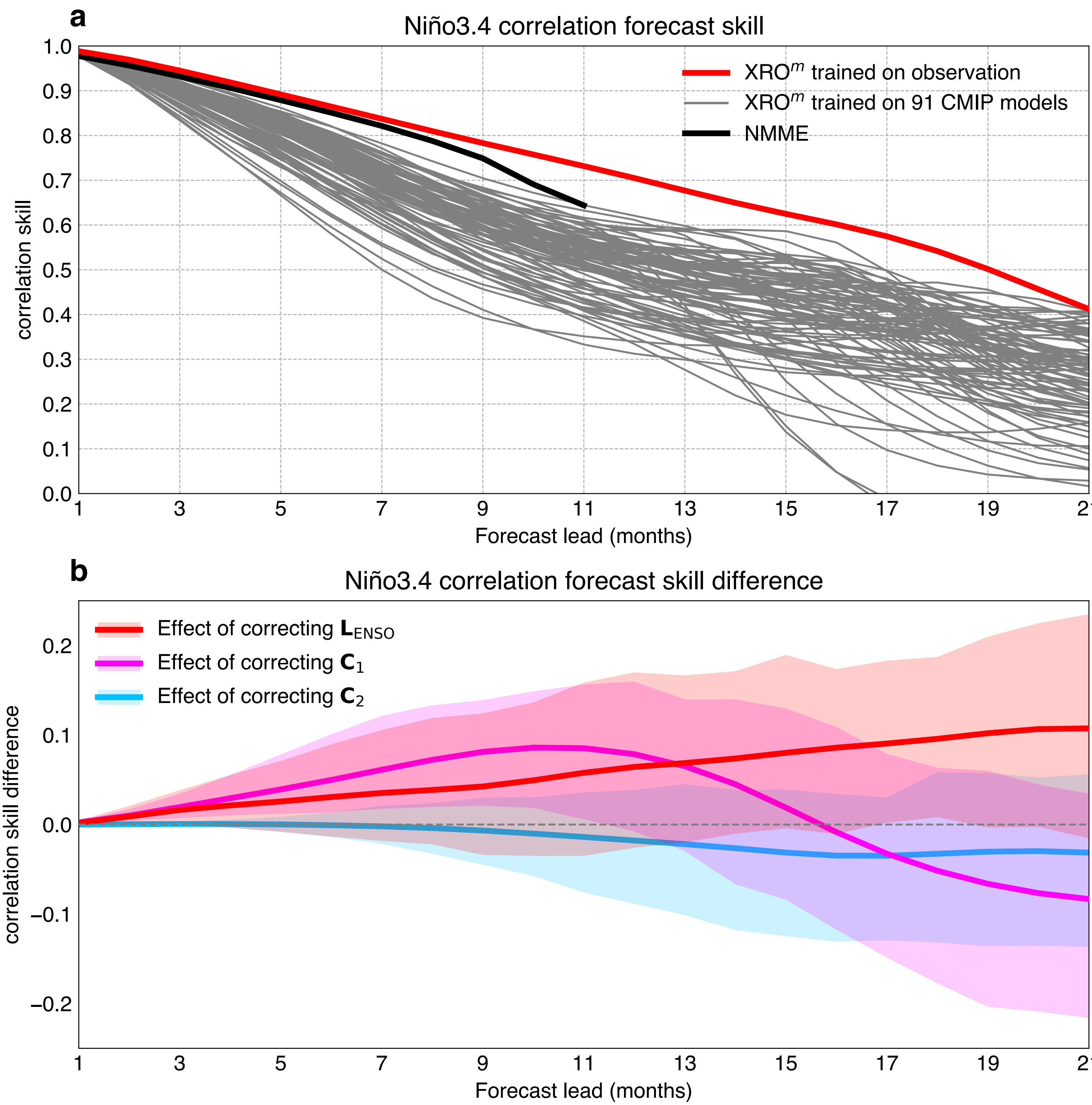
a
Niño3.4 correlation forecast skill
XRO^m trained on observation
XRO^m trained on 91 CMIP models
NMME
correlation skill
Forecast lead (months)
b
Niño3.4 correlation forecast skill difference
Effect of correcting $\mathbf{L}_{\mathrm{ENSO}}$
Effect of correcting $\mathbf{C}_1$
Effect of correcting $\mathbf{C}_2$
correlation skill difference
Forecast lead (months)

Supplementary Information for
"Explainable El Niño predictability from climate mode interactions"

Sen Zhao[1], Fei-Fei Jin[1,2], Malte F. Stuecker[3,2], Philip R. Thompson[3], Jong-Seong Kug[4], Michael J. McPhaden[5], Mark A. Cane[6], Andrew T. Wittenberg[7], Wenju Cai[8,9,10,11]

[1] *Department of Atmospheric Sciences, School of Ocean and Earth Science and Technology (SOEST), University of Hawai'i at Mānoa, HI, USA*
[2] *International Pacific Research Center, SOEST, University of Hawai'i at Mānoa, Honolulu, HI, USA*
[3] *Department of Oceanography, SOEST, University of Hawai'i at Mānoa, Honolulu, HI, USA*
[4] *School of Earth and Environmental Sciences, Seoul National University, Seoul, South Korea*
[5] *National Oceanic and Atmospheric Administration (NOAA)/Pacific Marine Environmental Laboratory, Seattle, WA, USA*
[6] *Lamont Doherty Earth Observatory of Columbia University, Palisades, NY, USA*
[7] *NOAA/OAR/Geophysical Fluid Dynamics Laboratory, Princeton, NJ, USA*
[8] *Frontiers Science Center for Deep Ocean Multispheres and Earth System, Physical Oceanography Laboratory, and Sanya Oceanographic Institution, Ocean University of China, Qingdao, China*
[9] *Laoshan Laboratory, Qingdao, China*
[10] *State Key Laboratory of Loess and Quaternary Geology, Institute of Earth Environment, Chinese Academy of Sciences, Xi'an, China*
[11] *State Key Laboratory of Marine Environmental Science & College of Ocean and Earth Sciences, Xiamen University, Xiamen, China*

Correspondence and requests for materials should be addressed to Fei-Fei Jin (jff@hawaii.edu)

Contents:

Supplementary Text

Supplementary Text 1. Efficacy of the XRO in simulating ENSO and other climate modes

First, the XRO captures the observed seasonal synchronization of ENSO, with the Niño3.4 SSTA standard deviation peaking in November-December-January (Fig. 2a). This seasonal synchronization is primarily governed by the seasonal modulation of the SSTA growth rate due to the tropical Pacific background seasonal cycle (*Stein et al. 2014*; *Chen and Jin 2021*; *Levine and McPhaden 2015*). Second, the XRO successfully replicates El Niño-La Niña asymmetry, manifesting as positively skewed Niño3.4 SSTAs (Fig. 2b). This asymmetry arises from multiple nonlinear physical processes, such as oceanic nonlinear dynamical heating (*An and Jin 2004*; *An et al. 2020*) and nonlinear SST-wind stress coupling due to the nonlinear dependence of deep convection on SST (*Kang and Kug 2002*; *Choi et al. 2013*; *Geng et al. 2020*). Third, the observed ENSO periodicity is reasonably captured, with a Niño3.4 spectral peak at periods of 2-6 years (Fig. 2c).The XRO also captures the lead-time of warm water volume (WWV) anomaly ahead of ENSO SSTA by approximately 6-9 months (Fig. 2d), which is largely controlled by ENSO periodicity (*Zhao et al. 2021*). Fourth, the XRO generates the observed irregular interannual oscillations between El Niño and La Niña, including occurrences of single- and multi-year ENSO events (Supplementary Fig. 3). Various mechanisms governing multi-year ENSO occurrences have been well-documented, including nonlinearity (*Okumura et al. 2011*; *DiNezio and Deser 2014*), ENSO-combination mode and anomalous Ekman transport (*Iwakiri and Watanabe 2021*, *2022*), the NPMM and North Pacific Oscillation (*Ding et al. 2022*; *Geng et al. 2023*; *Park et al. 2021*; *Kim et al. 2023*), as well as inter-basin interactions with tropical Indian and/or Atlantic Oceans (*Kim and Yu 2022*). Notably, the XRO model incorporates all these elements either explicitly or implicitly (See *"Extended Nonlinear Recharge-Oscillator model (XRO)" in Methods*). Fifth, the XRO accurately reproduces the rapid decline in ENSO SSTA autocorrelation across boreal spring, commonly referred to as the spring persistence barrier (Supplementary Fig. 4).

The XRO reproduces the seasonal synchronization of the other climate modes that is seen in observations (Supplementary Fig. 5a-h), which in this model is largely caused by the seasonally varying damping rates of the individual modes, together with their coupled interactions (see diagonal axis in Extended Data Fig. 1). Notably, ENSO-driven processes play a pronounced role in the seasonal synchronization of some of the modes. For instance, the IOB warming, forced by El Niño, reaches its mature phase during boreal spring and summer, following the mature phase of El Niño (Supplementary Fig. 5c). The variance of the TNA peaks in boreal spring, due to both the seasonal modulation of its damping rate and the remote forcing from ENSO (*Chen et al. 2021*; *Jiang et al. 2023*). Moreover, the XRO reasonably reproduces the observed asymmetries of both the IOB and IOD, manifesting as positively skewed SSTAs in the central and western tropical Indian Ocean, and negatively skewed SSTAs in the eastern Indian Ocean near Java and Sumatra (Supplementary Fig. 5k-l). The positive skewness of the IOB primarily arises as a response to the skewed remote forcing from ENSO, while the IOD asymmetry is dominated by local nonlinear processes (*An et al. 2023*). Furthermore, the XRO accurately reproduces the observed seasonal autocorrelation of the other modes (Supplementary Fig. 6).

Supplementary Tables

Supplementary Table 1. Definition of SST indices for climate modes used in the study.

Climate Mode	Acronym	Description	References
El Niño-Southern Oscillation	ENSO	SSTAs averaged over Niño3.4 region 170°–120°W, 5°S–5°N	(*Trenberth 1997*)
North Pacific Meridional Mode	NPMM	SSTAs averaged over 160°-120°W, 10°-25°N	(*Richter et al. 2022*)
South Pacific Meridional Mode	SPMM	SSTAs averaged over 110°-90°W, 25°-15°S	(*Zhang et al. 2014*)
Indian Ocean Basin mode	IOB	SSTAs averaged over 40°–100°E, 20°S–20°N	(*Xie et al. 2009*)
Indian Ocean Dipole mode	IOD	SSTAs averaged over 50°–70°E, 10°S–10°N minus those averaged over 90°–110°E, 10°S–0°N	(*Saji et al. 1999*)
Southern Indian Ocean Dipole mode	SIOD	SSTAs averaged over 65°–85°E, 25°–10°S minus those averaged over 90°–120°E, 30°–10°S	(*Jo et al. 2022*)
Tropical North Atlantic variability	TNA	SSTAs averaged over 55°–15°W, 5°–25°N	(*Enfield et al. 1999*)
Atlantic Niño	ALT3	SSTAs averaged over 20°W–0°E, 3°S–3°N	(*Nnamchi et al. 2015*)
South Atlantic Subtropical Dipole	SASD	SSTAs averaged over 60°–0°W, 45°–35°S minus those averaged over 40°W–20°E, 30°–20°S	(*Rodrigues et al. 2015*)

Supplementary Table 2. Observational data used in the study.

Dataset (Period)	Variables	Description and Reference	Source
HadISST (1871-2023)	SST	Hadley Centre Sea Ice and Sea Surface Temperature dataset version 1.1 (*Rayner et al. 2003*)	https://www.metoffice.gov.uk/hadobs/hadisst/
ERSSTv5 (1871-2023)	SST	Extended Reconstructed Sea Surface Temperature version 5 (*Huang et al. 2017*)	https://psl.noaa.gov/data/gridded/data.noaa.ersst.v5.html
COBE-SST2 (1871-2023)	SST	Centennial in situ Observation-Based Estimates of Sea Surface Temperature version 2 (*Hirahara et al. 2014*)	https://ds.data.jma.go.jp/tcc/tcc/products/elnino/cobesst_doc.html
GECCO3 (1950-2018)	SST, Temp*	German contribution to Estimating the Circulation and Climate of the Ocean version 3 (*Köhl 2020*)	https://icdc.cen.uni-hamburg.de/thredds/catalog/ftpthredds/EASYInit/GECCO3/regular_1x1_grid/catalog.html
GODAS (1950-2023)	SST, Temp	Global Ocean Data Assimilation System (*Behringer and Xue 2004*)	https://psl.noaa.gov/data/gridded/data.godas.html
ORAS5 (1958-2023)	SST, Temp	ECMWF Ocean Reanalysis System 5 (*Zuo et al. 2019*)	https://doi.org/10.24381/cds.67e8eeb7
ORA20C (1900-2009)	SST, Temp	ECMWF Ocean Reanalysis of the 20th Century (*de Boisséson et al. 2018*)	https://www.cen.uni-hamburg.de/en/icdc/data/ocean/easy-init-ocean/ecmwf-ensemble-of-ocean-reanalyses-of-the-20th-century-ora-20c.html
PEODAS (1960-2014)	SST, Temp	Predictive Ocean Atmosphere Model for Australia Ensemble Ocean Data Assimilation System (*Yin et al. 2011*)	http://opendap.bom.gov.au:8080/thredds/catalogs/bmrc-poama-catalog.html
SODA224 (1871-2010)	SST, Temp	Simple Ocean Data Assimilation Phase 2.2.4 (*Carton and Giese 2008*)	https://apdrc.soest.hawaii.edu/dods/public_data/SODA
ERA5 (1979-2022)	Surface air temperature	ECMWF Atmospheric Reanalysis v5 (*Hersbach et al. 2020*)	https://doi.org/10.24381/cds.f17050d7
CMAP (1979-2022)	Precipitation	Gridded precipitation from the Climate Prediction Center Merged Analysis of Precipitation (*Xie and Arkin 1997*)	https://psl.noaa.gov/data/gridded/data.cmap.html

*Temp is 3-dimensional ocean temperature

Supplementary Table 3. El Niño type forecasts for the Nov-Dec-Jan target season, based on Niño3 and Niño4 indices at a 9-month lead-time.

Year	ORAS5	XRO2 fitted on 1979-2022 (lead=9)	XRO2 fitted on 1950-1990 (lead=9)	AI (lead=9)	NMME (lead=9)
1982	EP	EP	-	-	MIX
1986	MIX	MIX	-	MIX	MIX
1991	MIX	MIX	MIX	MIX	MIX
1997	EP	EP	EP	MIX	MIX
2002	MIX	MIX	MIX	Neutral state	MIX
2009	MIX	EP	Neutral state	MIX	MIX
2015	MIX	MIX	MIX	MIX	MIX

Supplementary Table 4. Details of the NMME models used in this study.

Model	Name used here	Period	Ensemble size	Maximum lead time (months)
CMC1-CanCM3	CanCM3	January 1981–December 2019	10	11
CMC2-CanCM4	CanCM4	January 1981–December 2019	10	11
COLA-RSMAS-CCSM4	CCSM4	January 1982–December 2017	10	11
NCEP-CFSv2	CFSv2	January 1982–July 2022	24	9
GEM-NEMO	GEM-NEMO	January 1981–December 2020	10	11
GFDL-CM2p1-aer04	GFDL	January 1982–December 2021	10	11
GFDL-CM2p5-FLOR-A06	GFDL-FLOR	March 1980–December 2021	12	11
GFDL-CM2p5-FLOR-B01	GFDL-FLOR	March 1980–December 2021	12	11
GFDL-SPEAR	GFDL-SPEAR	January 1991–December 2020	15	11
NASA-GEOSS2S	NASA-GEOSS2S	January 1981–December 2020	10	8

Supplementary Table 5. Lists of the 91 CMIP5/6 climate models used in this study.

CMIP5 No.	CMIP5 Models	Member	CMIP6 No.	CMIP6 Models	Member
1	ACCESS1-0	r1i1p1	1	ACCESS-CM2	r1i1p1f1
2	ACCESS1-3	r1i1p1	2	ACCESS-ESM1-5	r1i1p1f1
3	bcc-csm1-1	r1i1p1	3	AWI-CM-1-1-MR	r1i1p1f1
4	bcc-csm1-1-m	r1i1p1	4	BCC-CSM2-MR	r1i1p1f1
5	BNU-ESM	r1i1p1	5	BCC-ESM1	r1i1p1f1
6	CanESM2	r1i1p1	6	CAMS-CSM1-0	r1i1p1f1
7	CCSM4	r1i1p1	7	CAS-ESM2-0	r1i1p1f1
8	CESM1-BGC	r1i1p1	8	CESM2	r4i1p1f1
9	CESM1-CAM5	r1i1p1	9	CESM2-FV2	r1i1p1f1
10	CESM1-FASTCHEM	r1i1p1	10	CESM2-WACCM	r1i1p1f1
11	CESM1-WACCM	r1i1p1	11	CESM2-WACCM-FV2	r1i1p1f1
12	CMCC-CESM	r1i1p1	12	CIESM	r1i1p1f1
13	CMCC-CM	r1i1p1	13	CMCC-CM2-HR4	r1i1p1f1
14	CMCC-CMS	r1i1p1	14	CMCC-CM2-SR5	r1i1p1f1
15	CNRM-CM5	r1i1p1	15	CMCC-ESM2	r1i1p1f1
16	CSIRO-Mk3-6-0	r1i1p1	16	CNRM-CM6-1	r1i1p1f2
17	FGOALS-g2	r1i1p1	17	CNRM-ESM2-1	r1i1p1f2
18	FGOALS-s2	r1i1p1	18	CanESM5	r1i1p1f1
19	FIO-ESM	r1i1p1	19	E3SM-1-0	r1i1p1f1
20	GFDL-CM3	r1i1p1	20	E3SM-1-1	r1i1p1f1
21	GFDL-ESM2G	r1i1p1	21	E3SM-1-1-ECA	r1i1p1f1
22	GFDL-ESM2M	r1i1p1	22	EC-Earth3	r1i1p1f1
23	GISS-E2-H-CC	r1i1p1	23	EC-Earth3-Veg	r1i1p1f1
24	GISS-E2-H	r1i1p1	24	FGOALS-f3-L	r1i1p1f1
25	GISS-E2-R-CC	r1i1p1	25	FGOALS-g3	r1i1p1f1
26	GISS-E2-R	r1i1p1	26	FIO-ESM-2-0	r1i1p1f1
27	HadCM3	r1i1p1	27	GFDL-CM4	r1i1p1f1
28	HadGEM2-AO	r1i1p1	28	GFDL-ESM4	r1i1p1f1
29	HadGEM2-CC	r1i1p1	29	GISS-E2-1-G	r1i1p1f1
30	HadGEM2-ES	r1i1p1	30	GISS-E2-1-G-CC	r1i1p1f1
31	IPSL-CM5A-LR	r1i1p1	31	GISS-E2-1-H	r1i1p1f1
32	IPSL-CM5A-MR	r1i1p1	32	HadGEM3-GC31-LL	r1i1p1f3
33	IPSL-CM5B-LR	r1i1p1	33	INM-CM4-8	r1i1p1f1
34	MIROC5	r1i1p1	34	INM-CM5-0	r10i1p1f1
35	MIROC-ESM-CHEM	r1i1p1	35	IPSL-CM6A-LR	r1i1p1f1
36	MIROC-ESM	r1i1p1	36	MIROC6	r1i1p1f1
37	MPI-ESM-LR	r1i1p1	37	MIROC-ES2L	r1i1p1f2
38	MPI-ESM-MR	r1i1p1	38	MPI-ESM-1-2-HAM	r1i1p1f1
39	MPI-ESM-P	r1i1p1	39	MPI-ESM1-2-HR	r1i1p1f1
40	MRI-CGCM3	r1i1p1	40	MPI-ESM1-2-LR	r10i1p1f1
41	MRI-ESM1	r1i1p1	41	MRI-ESM2-0	r1i2p1f1
42	NorESM1-ME	r1i1p1	42	NESM3	r1i1p1f1
43	NorESM1-M	r1i1p1	43	NorESM2-LM	r1i1p1f1
			44	NorESM2-MM	r1i1p1f1
			45	SAM0-UNICON	r1i1p1f1
			46	TaiESM1	r1i1p1f1
			47	UKESM1-0-LL	r1i1p1f2
			48	NorCPM1	r1i1p1f1

Supplementary Figures

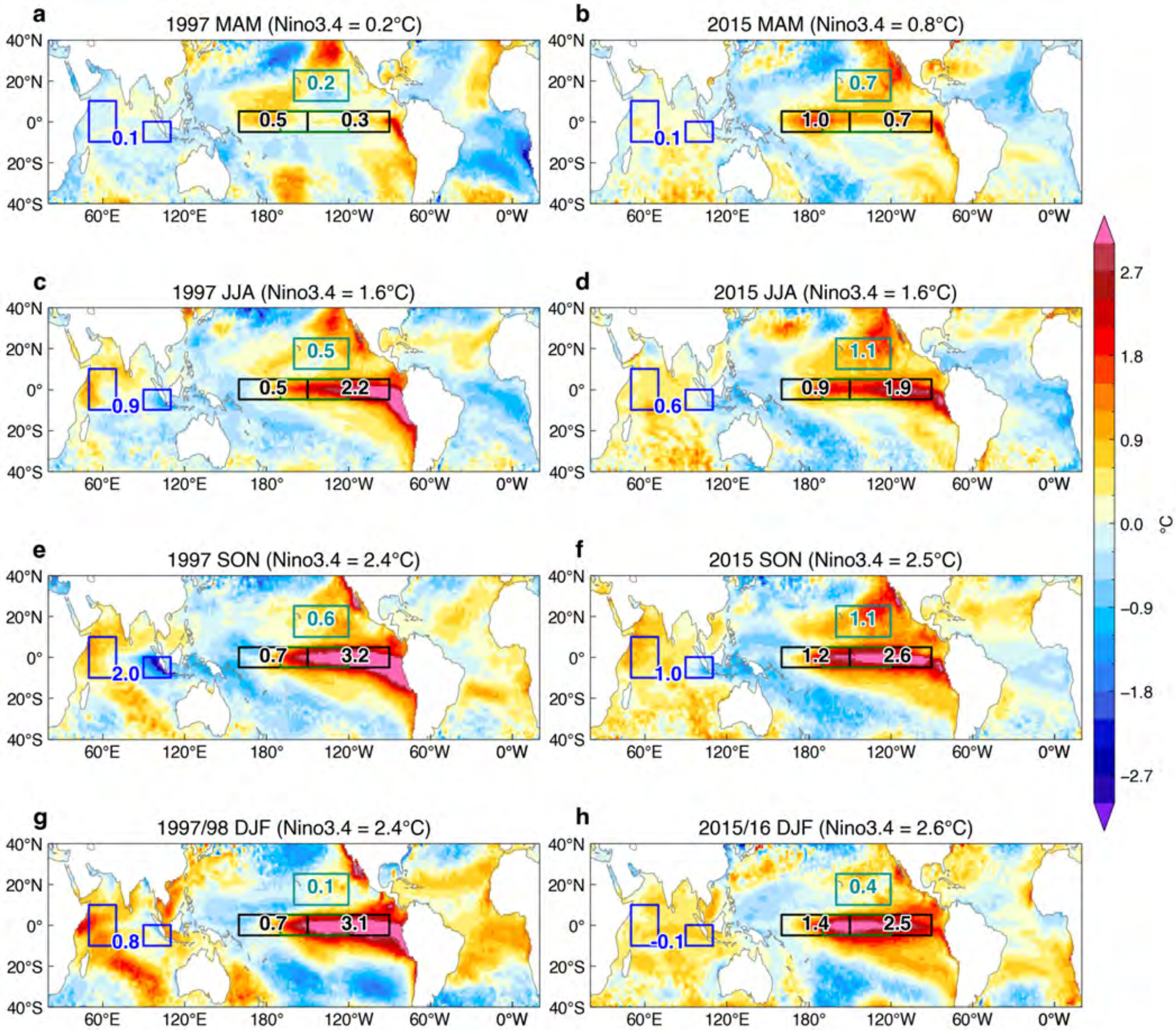

Supplementary Fig. 1| Observed differences in tropical SSTA pattern and evolution between the 1997/98 and 2015/16 El Niño events derived from ORAS5 reanalysis. The SSTAs during (a) 1997 MAM, (b) 2015 MAM, (c) 1997 JJA, (d) 2015 JJA, (e) 1997 SON, (f) 2015 SON, (g) 1997/98 DJF and (h) 2015/16 DJF. In each panel, the values of Niño3, Niño4, IOD, and NPMM SSTAs are indicated in the corresponding boxes, and the value of Niño3.4 is indicated in the title. The 1997/98 and 2015/16 El Niño events have different SSTA patterns in the central and far eastern equatorial Pacific, as well as different associated IOD and NPMM intensities. The 1997 event exhibits eastern Pacific El Niño characteristics with the warmest SSTAs in the far eastern equatorial Pacific and a strong concurrent IOD, partly due to stronger WWV preconditioning. In 2015, the SSTA peak is located closer to the central Pacific, possibly due to the strong coupling of the NPMM and central equatorial Pacific SST.

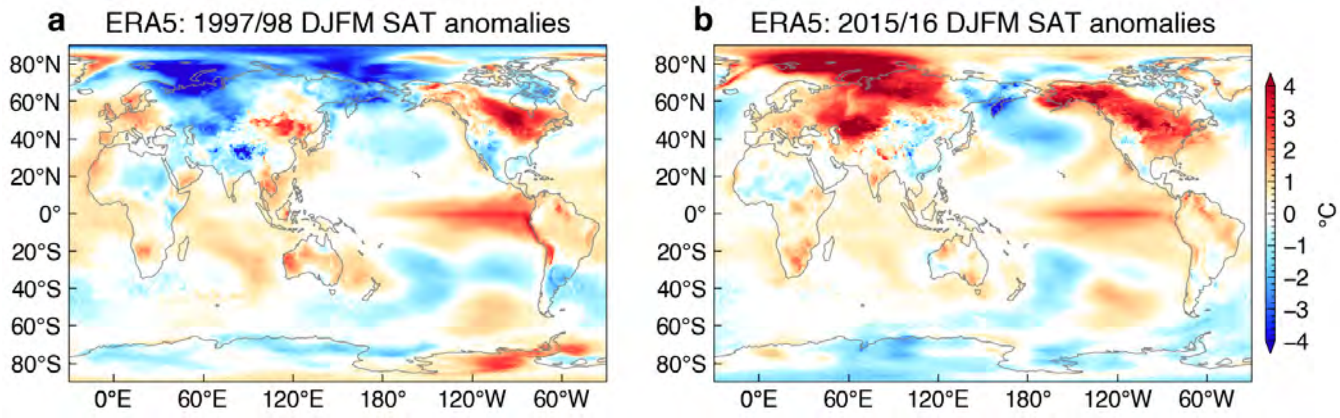

Supplementary Fig. 2| Observed surface air temperature (SAT) anomalies for the 1997/98 and 2015/16 El Niño events during December-March (DJFM). The (a) 1997/98 and (b) 2015/16 El Niño events were associated with different pan-Arctic SAT, consistent with Jeong et al. (*2022*).

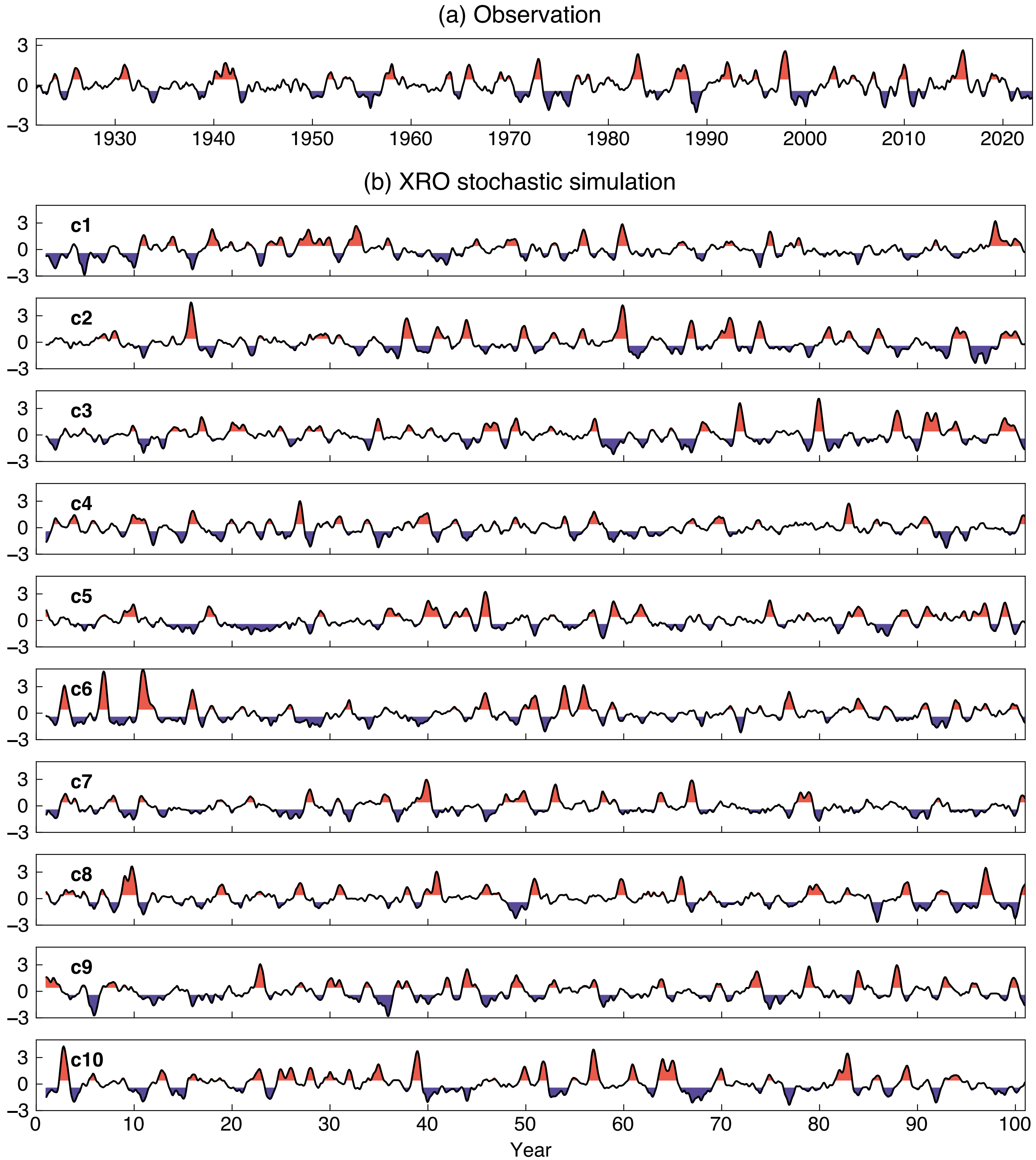

Supplementary Fig. 3| ENSO time series in the observation and XRO stochastic simulation. The 3-month running mean of Niño3.4 SSTA for (**a**) the ensemble mean of multiple observational SST datasets for 1923-2022 (Supplementary Table 2), and (**b**) the 10 consecutive centuries (numbered) from the XRO stochastic simulation. The red/blue shading denote the SSTA above 0.5 / below -0.5℃, respectively. The XRO stochastic simulation reproduces the irregular interannual oscillations between El Niño and La Niña.

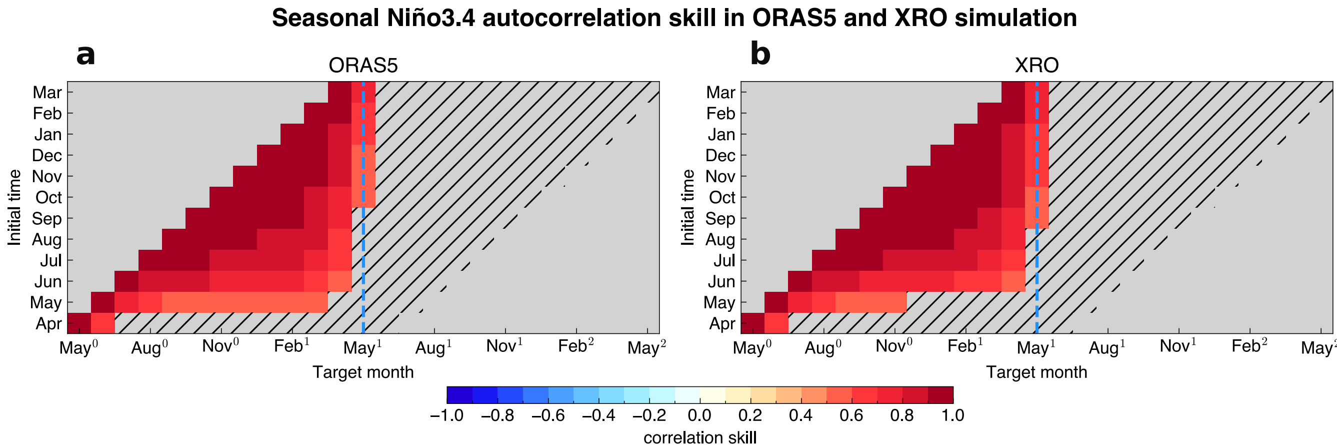

Supplementary Fig. 4| Seasonal autocorrelation of Niño3.4 SST index. Correlations of Niño3.4 index with itself, as a function of initialization month (ordinate) and target month (abscissa) for the ORAS5 reanalysis (1979-2022) (**a**) and for the XRO stochastic simulations (**b**, ensemble mean). Hatching highlights correlation skills less than 0.5. The dashed vertical blue lines denote the spring predictability barrier season. The XRO accurately reproduces the rapid decline in ENSO SSTA autocorrelation across boreal spring.

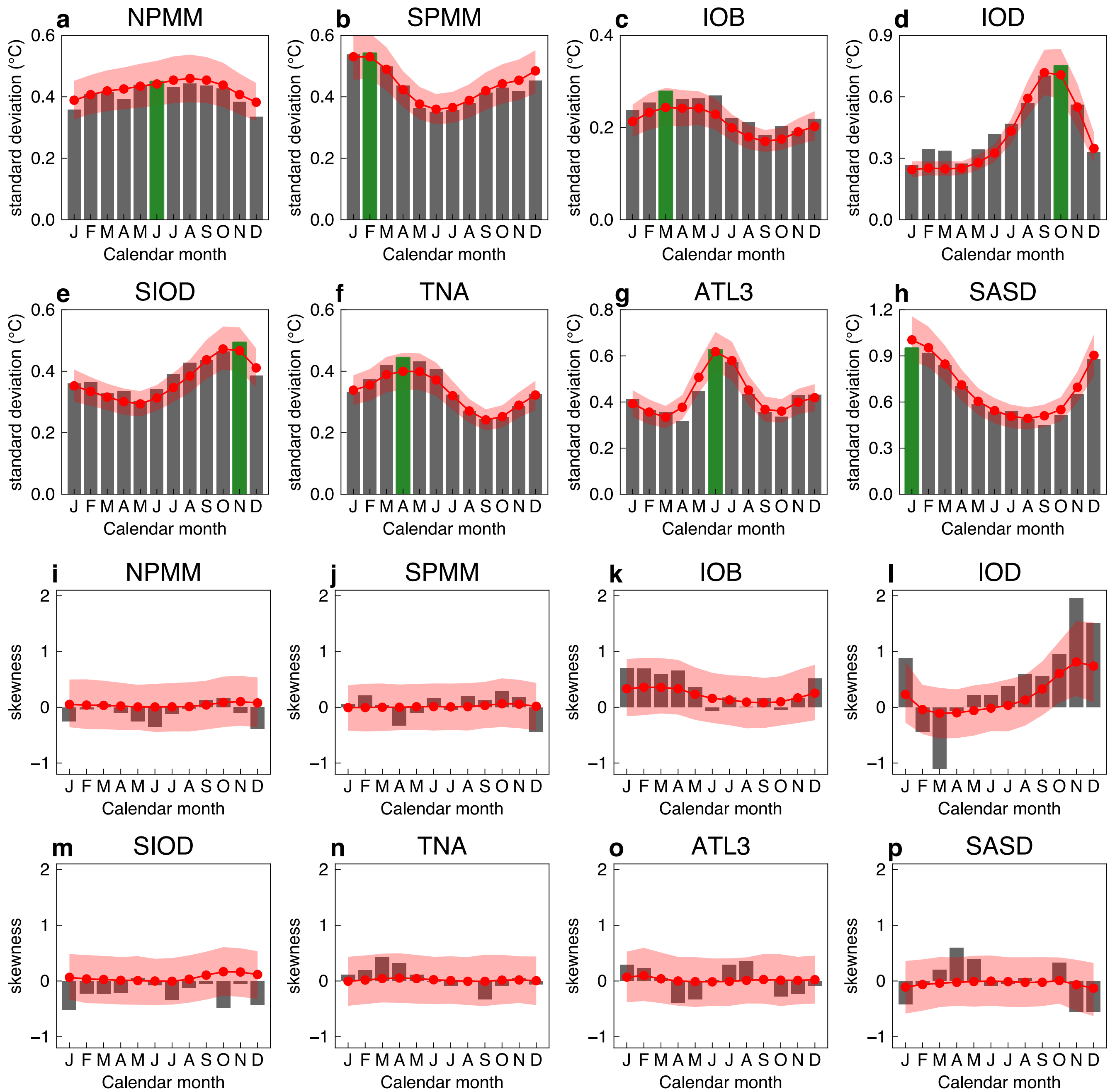

Supplementary Fig. 5| Seasonal statistics of SSTA indices for the other climate modes. a-h, Seasonally varying standard deviation of the SSTA indices for the NPMM, SPMM, IOB, IOD, SIOD, TNA, ATL3, and SASD, respectively, in the ORAS5 observations (1979-2022) (*bars*) and the XRO stochastic simulations (*red curves*). Red shading indicates the 10%-90% spread bands of simulated 43-year epochs, obtained from splitting a 43,000-year XRO simulation into 1000 non-overlapping blocks. The month of peak standard deviation for each observed mode is indicated in green. **i-p**, Same as a-h, but for seasonally varying skewness. The XRO accurately simulates the observed seasonal synchronization of specific climate modes, and reasonably reproduces the observed warm/cold asymmetries of both the IOB and IOD.

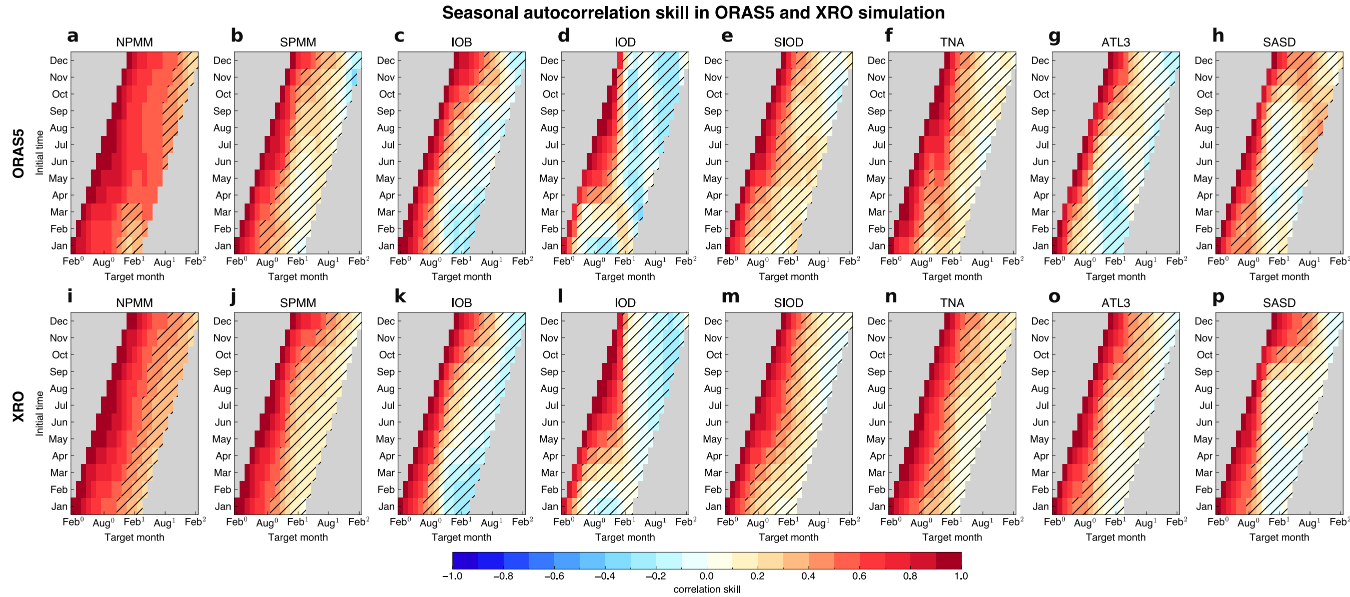

Supplementary Fig. 6| Seasonal autocorrelation of SSTA indices for other climate modes. Correlations of each index with itself, as a function of initialization month (ordinate) and target month (abscissa) for the ORAS5 reanalysis (1979-2022) (upper row) and for the XRO stochastic simulations (bottom row, ensemble mean). Hatching highlights correlation skills less than 0.5. The XRO accurately reproduces the seasonal autocorrelation structures of the other climate modes.

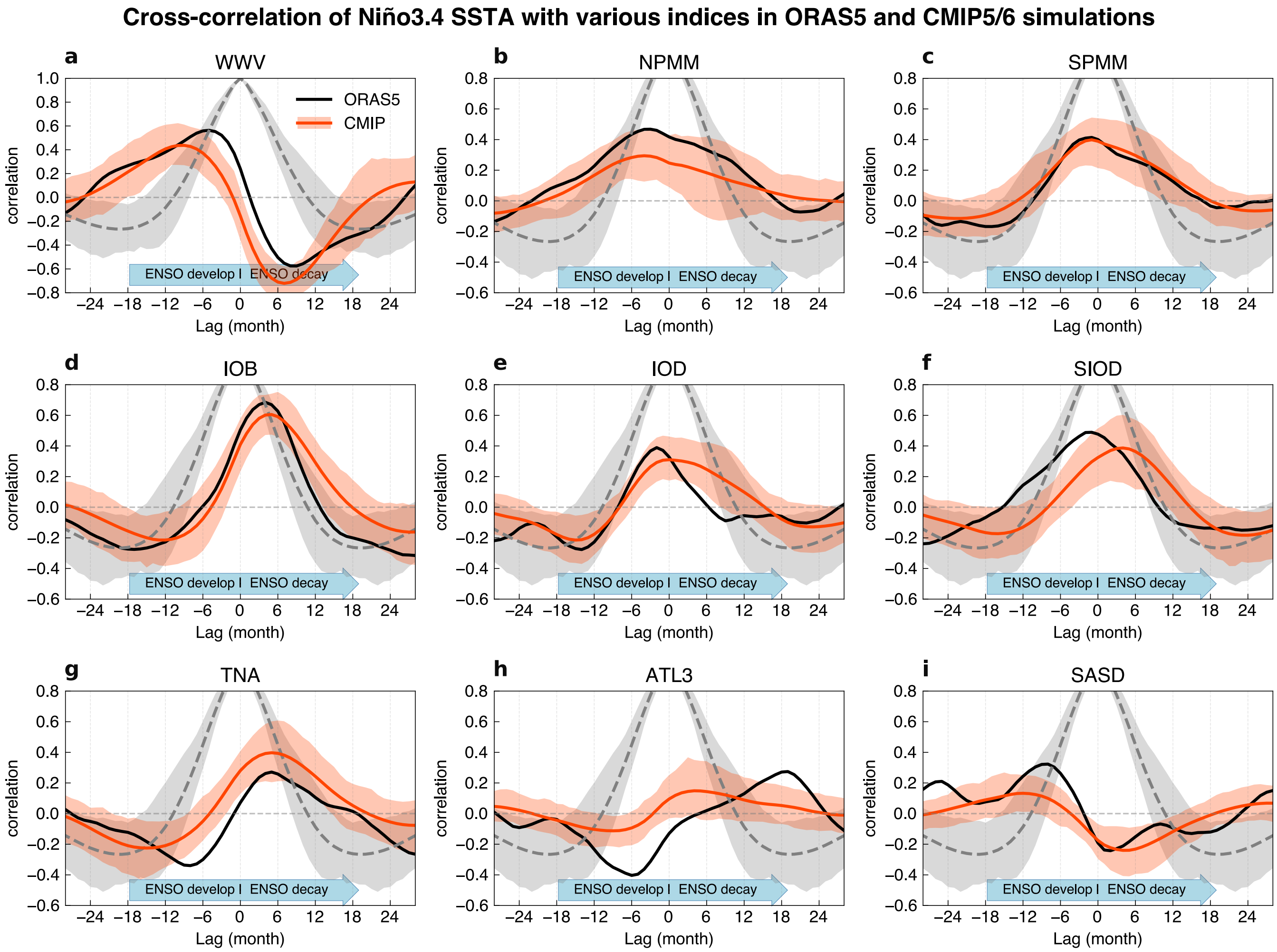

Supplementary Fig. 7| ENSO's lead-lag relationship with equatorial Pacific warm water volume (WWV) index and SSTA indices of other climate modes in CMIP historical simulations. Shown as monthly cross-correlations of each index with the lagged Niño3.4 index in ORAS5 reanalysis (1979-2022) (*black*) and CMIP5/6 historical simulations (1900-1999) (ensemble mean in red curves; red shading indicates the 10%-90% spread bands of 91 individual models). The dashed curves show the ensemble mean autocorrelation of Niño3.4 index in CMIP5/6 historical simulations (shading indicates the 10%-90% spread bands of 91 individual models). Abscissas are the lead-time, with negative values representing months for which the Niño3.4 index lags, and positive values representing months for which the Niño3.4 index leads. It is challenging for climate models to realistically simulates the observed ENSO SSTA lead-lag relationship with WWV anomalies and the SSTA indices for the other climate modes, especially for WWV index and Atlantic Ocean SST indices.

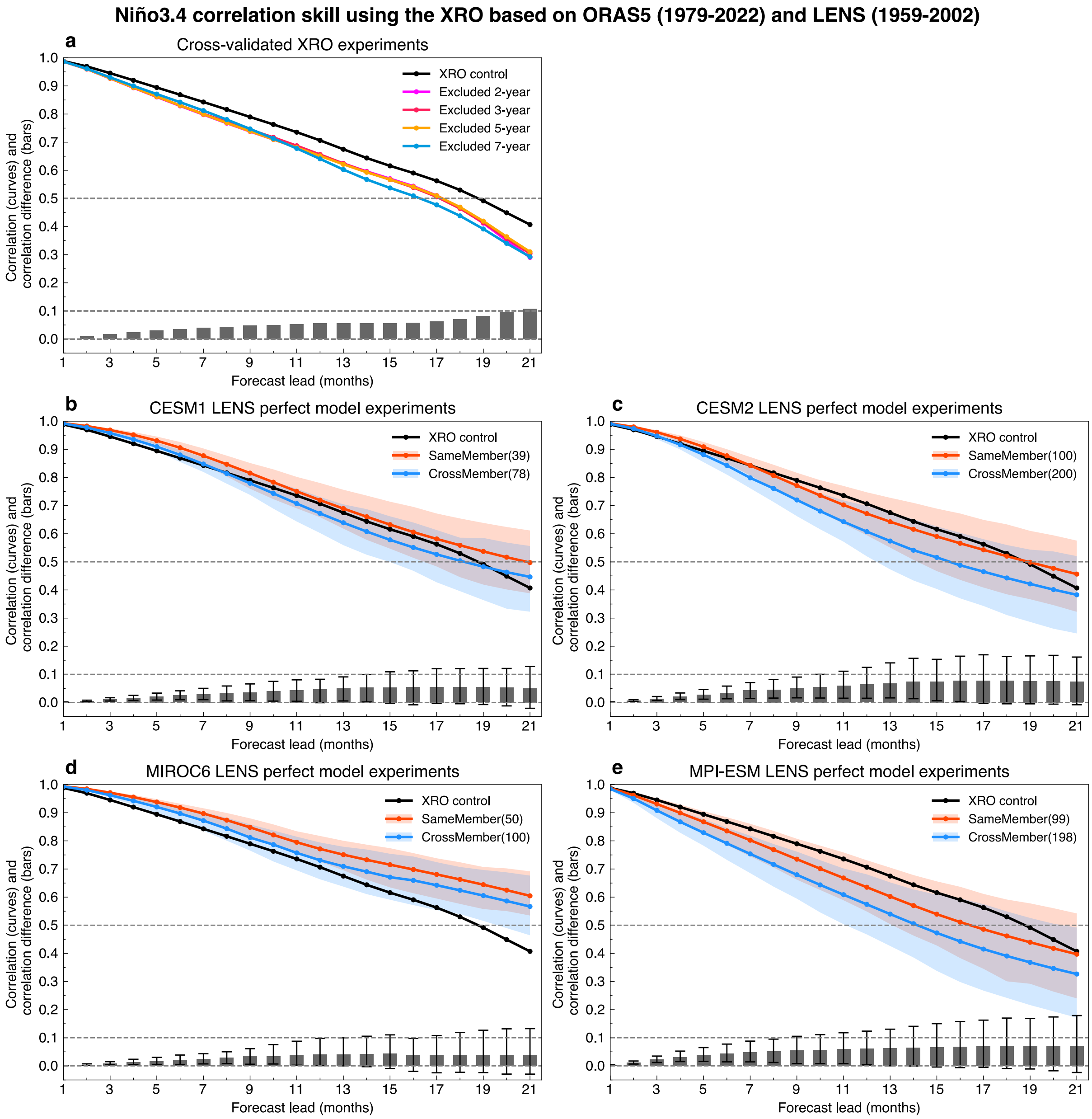

Supplementary Fig. 8| Robustness of the XRO parameter fitting and reforecasting ENSO. **a**, the all-months correlation skill of the 3-month running mean Niño3.4 index during 1979-2022 as a function of forecast lead for the XRO control forecast (*black curve*) and cross-validated XRO forecast that excluded from 2 to 7 years data (*coloured curves*), the mean skill difference between cross-validated XRO forecast and control forecast (*bars*). The dashed lines indicate 0.5, 0.1, and zero correlation skills. **b-d**, Same as **a**, but for skill for LENS perfect model "Same-Member" and "Cross-Member" experiments for CESM1, CESM2, MIROC6, and MPI-ESM during 1959-2002, respectively (See *"Large ensemble simulations and perfect model reforecasting experiments" in Methods*). The shadings denote the 10%-90% spread among the ensemble members within each LENS. The bottom bars denote the mean difference between "Same-Member" and "Cross-Member" experiments with error bars denote the 10%-90% spread among the ensemble members within each LENS. The XRO fitting and reforested ENSO is robust with uncertainty in Niño3.4 correlation skill less than 0.1 within 21 lead months.

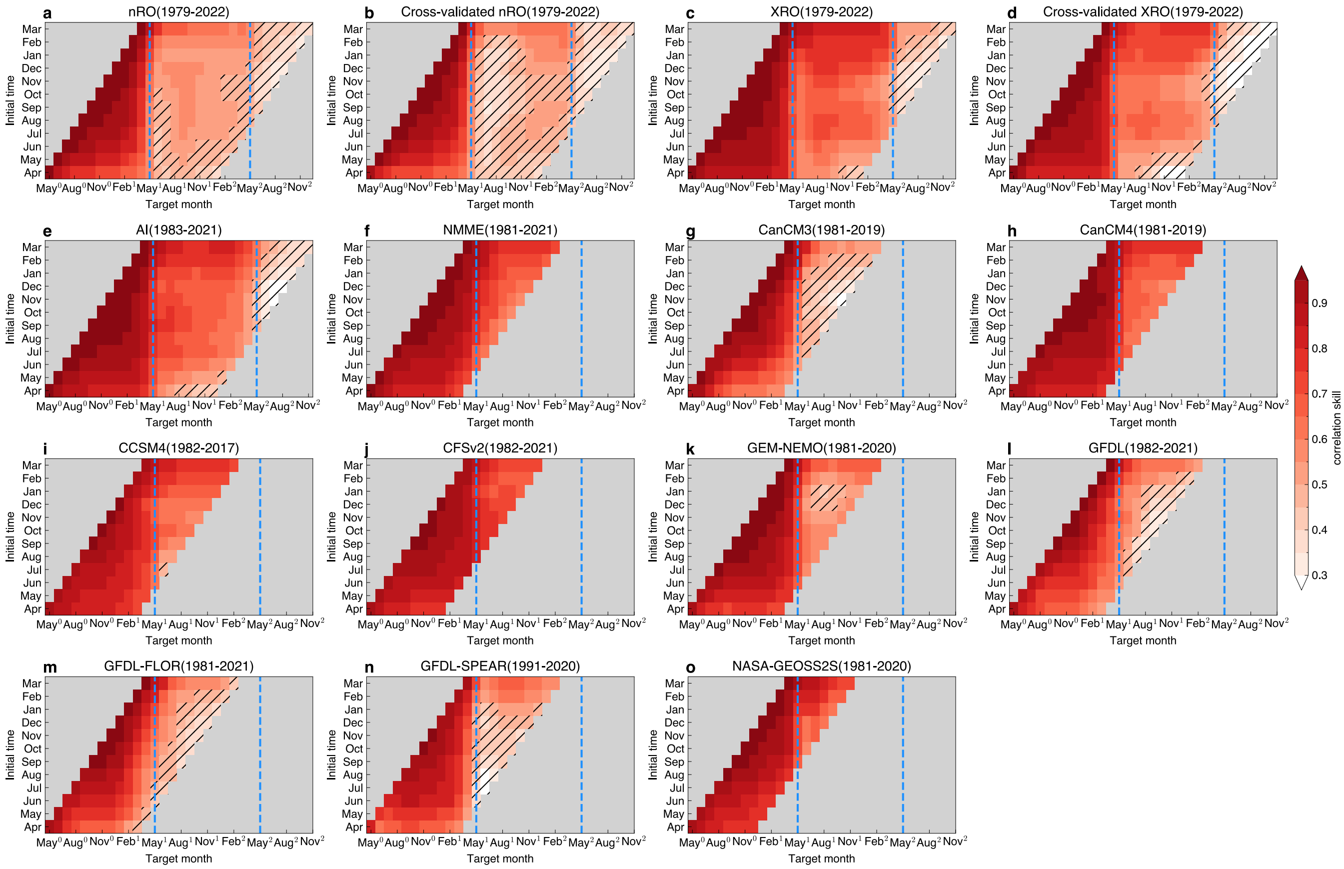

Supplementary Fig. 9| Seasonality of correlation forecast skill for ENSO. The correlation skills verified during 1979-2022 of various model forecasts of the Niño3.4 SSTA index, as a function of the start month (ordinate) and target month (abscissa; superscripts 0, 1, 2 denote the current and subsequent years, respectively), for the nRO (a), Cross-validated nRO (b), XRO (c), Cross-validated XRO (d), AI model (e), multi-model mean of NMME ensemble means (f), and ensemble means from individual dynamical models in the North American Multi-Model Ensemble (NMME)(g-o). Hatching highlights the forecasts with correlation skill less than 0.5. The dashed vertical blue lines denote the spring predictability barrier season. The nRO and most of the dynamical models exhibit a pronounced spring predictability barrier in May-June-July. The SPB is much less pronounced in the XRO, which is comparable in skill with the AI model in all seasons.

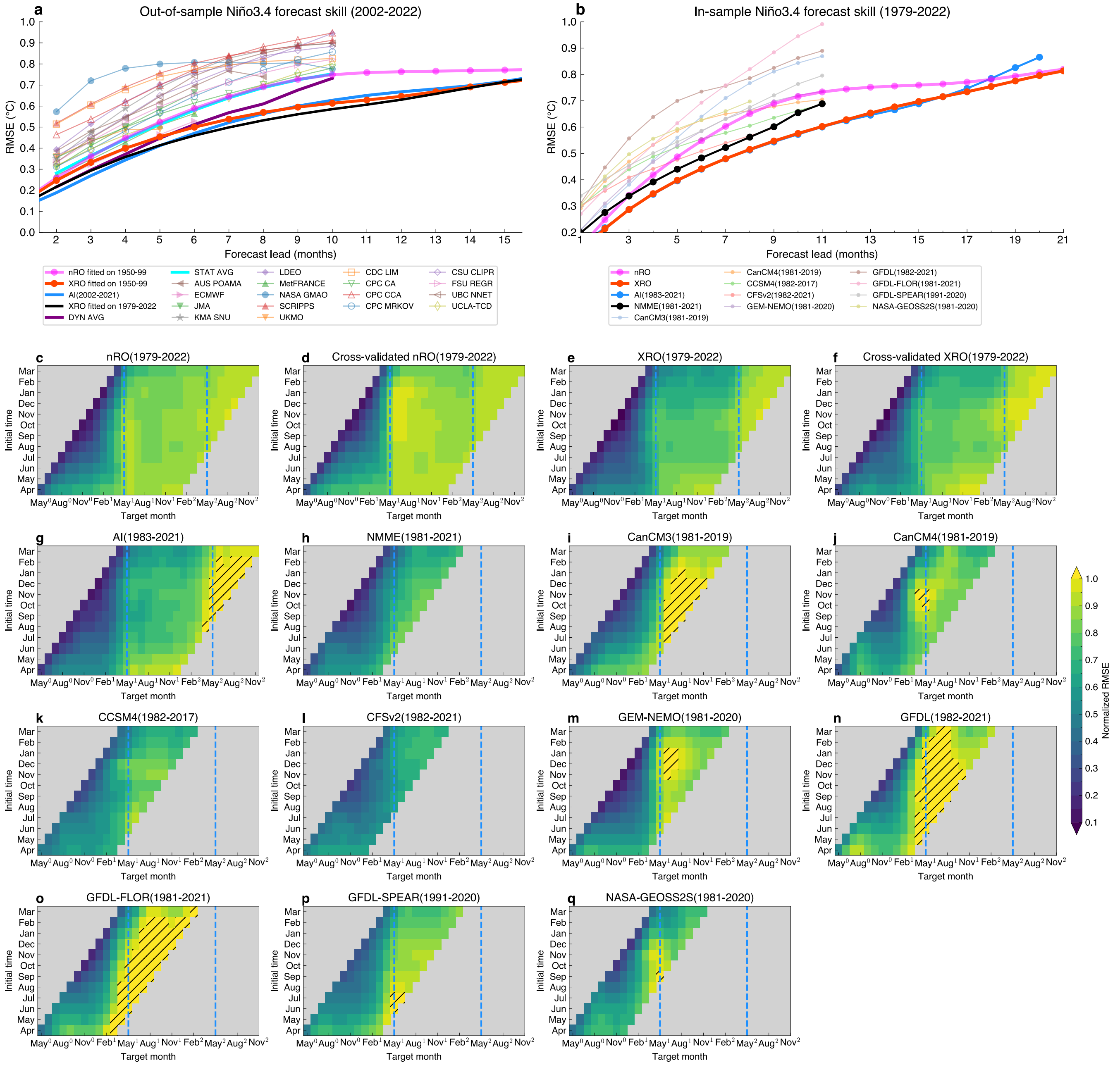

Supplementary Fig. 10| Root Mean Square Error (RMSE) forecast metric for ENSO. **a**, The all-months RMSE forecasts verified on 2002-2022 of the 3-month running mean Niño3.4 SSTA index, as a function of the forecast lead month in the out-of-sample nRO fitted on 1950-1999 (*magenta*), out-of-sample XRO fitted on 1950-1999 (*red*), the AI model, the XRO control fitted on 1979-2022 (*black curve*) and operational models aggregated by the International Research Institute for Climate and Society (IRI), ensemble mean of dynamical models (DYN AVG, *dark purple curve*), ensemble mean of statistical models (STAT AVG, *dark cyan curve*). **b**, same as **a**, but for RMSE skill of Niño3.4 forecasts verified 1979-2022 in the in-sample nRO (*magenta*), in-sample XRO model (*red*), AI model (*blue*), dynamical models from the North American Multi-Model Ensemble (NMME) project (multi-model ensemble of NMME in *black*, ensemble mean from individual models in *other colours*); **c-q**, The relative RMSE of

Niño3.4 SSTA forecasts, normalized by the seasonally-varying standard deviation of the observations, as a function of the forecast start month (ordinate) and target month (abscissa; superscripts 0, 1, 2 denote the current and subsequent years, respectively), for the nRO, cross-validated nRO, XRO, cross-validated XRO, AI model, dynamical models from the North American Multi-Model Ensemble (NMME) project (multi-model ensemble of NMME, ensemble mean from individual models). The dashed vertical blue lines denote the spring predictability barrier season. The superior efficacy of the XRO in ENSO forecasting is supported by the RMSE metric.

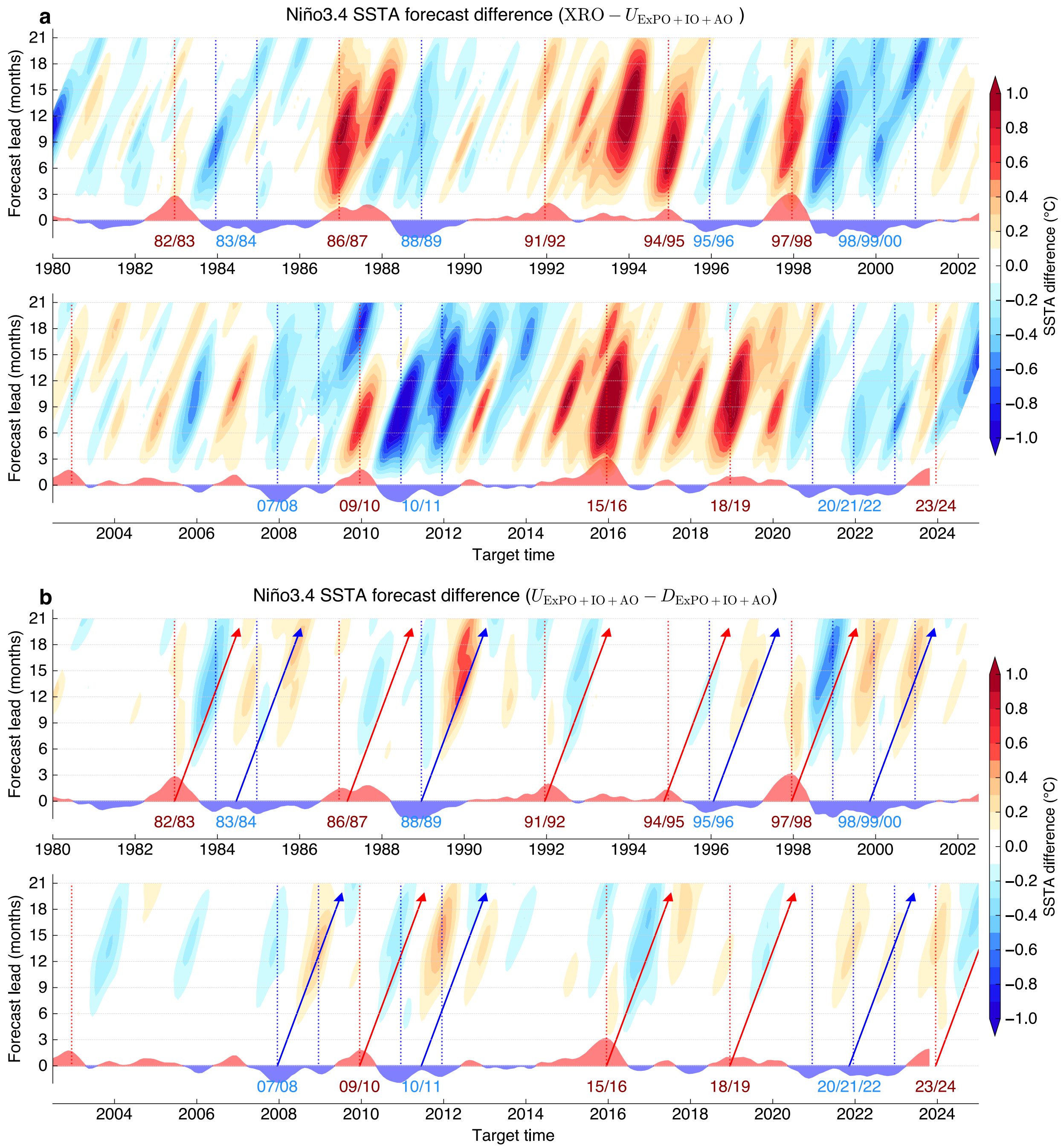

Supplementary Fig. 11| Comparison role of climate-mode interactions on Niño3.4 forecast between the component due to other climate modes' initial state and the component due to the ENSO initial state. Shown are the differences of Niño3.4 SSTA (*shading*) as a function of forecast lead and target time between the control and uninitialized ExPO+IO+AO experiment (a), and between the uninitialized ExPO+IO+AO and decoupled ExPO+IO+AO experiment forecasts (b). Vertical reference dashed lines denote December of El Niño (red) and La Niña (blue) years, respectively. The observed normalized time series of Niño3.4 SSTA index is indicated in the bottom axis. In b, the arrows indicate the flow of forecast integration started from the selected time. The other climate modes mainly affect ENSO via their initial condition memory.

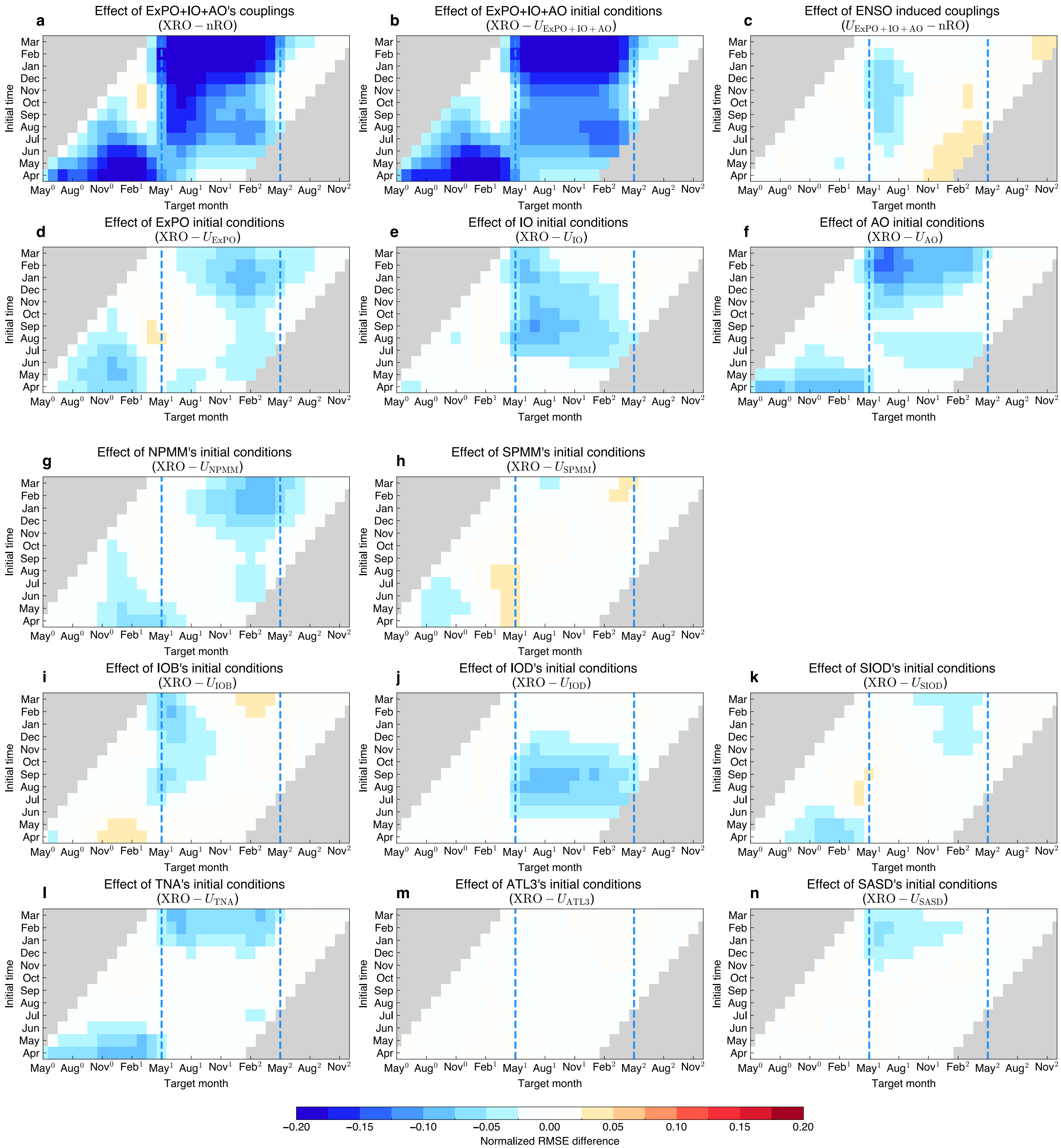

Supplementary Fig. 12| Quantifying the reduced ENSO forecast Root Mean Square Error (RMSE) from the coupled influences outside equatorial Pacific during 1979-2022. Shown is the relative RMSE difference of the Niño3.4 SSTA forecasts, normalized by the seasonally-varying standard deviation of the observations, as a function of the forecast start month (ordinate) and target month (abscissa; superscripts 0, 1, 2 denote the current and subsequent years, respectively). **a-d,** the skill difference between XRO and $D_{\mathrm{ExPO+IO+AO}}$ (a), between XRO and $U_{\mathrm{ExPO+IO+AO}}$ (b), and between $U_{\mathrm{ExPO+IO+AO}}$ and $D_{\mathrm{ExPO+IO+AO}}$ (c); **e-n,** the skill difference between control and the uninitialized ExPO, IO, AO, NPMM, SPMM, IOB, IOD, SIOD, TNA, ATL3, and SASD experiments, respectively. The importance of climate mode interactions in ENSO forecasting is supported by the RMSE metric.

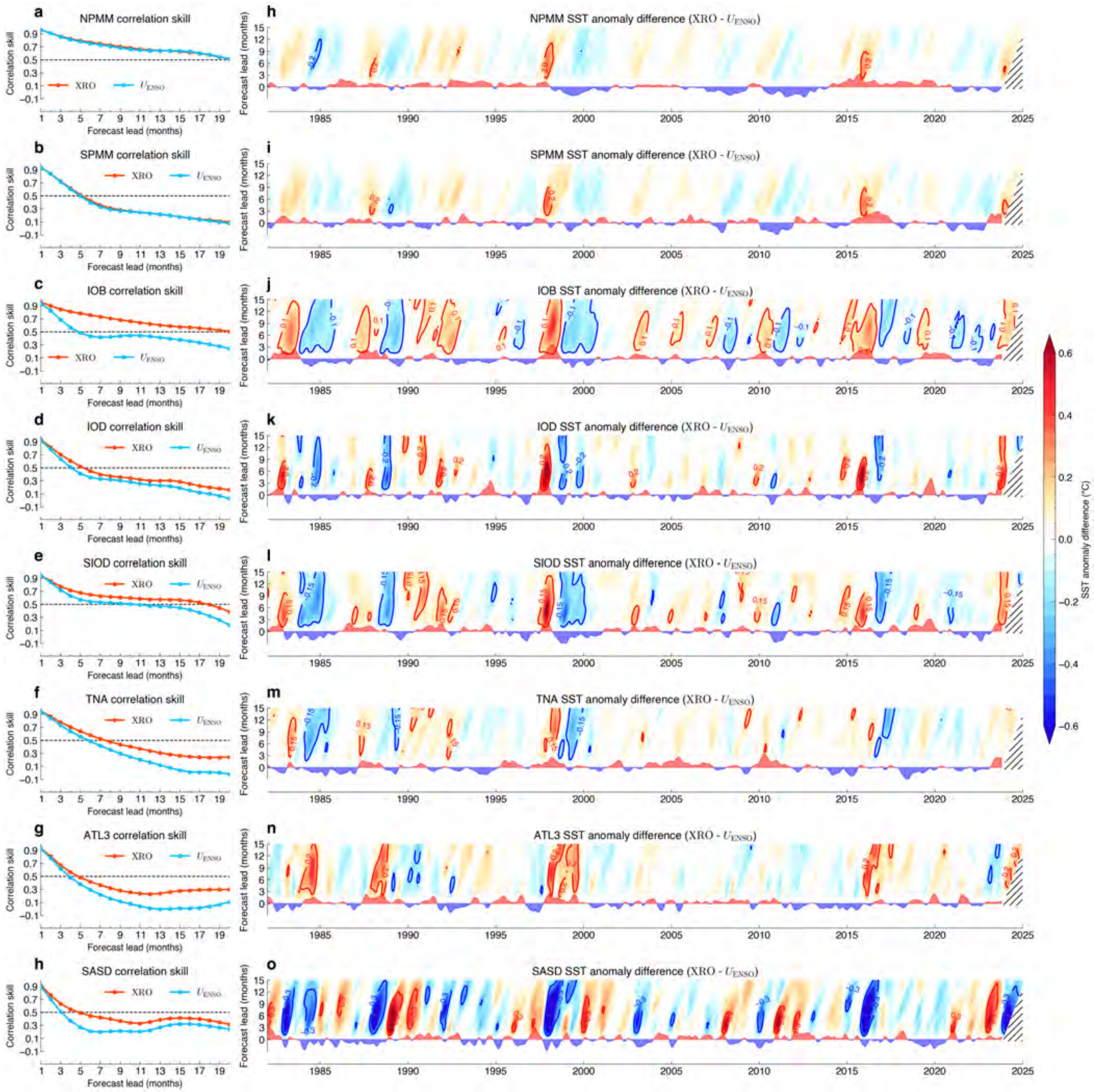

Supplementary Fig. 13| Impact of ENSO's initialization to other climate mode forecasts. Left panels (**a-h**) show the all-months correlation skill of the 3-month running mean each climate mode index during 1979-2022 as a function of forecast lead for the XRO control forecast (*red curve*) and uninitialized ENSO experiment (U_{ENSO}) forecast (*blue curve*). Right panels (**h-o**) show the difference of other climate mode SSTA (shading) as a function of forecast lead and target time, between control and uninitialized ENSO experiment (U_{ENSO}). The normalized time series of each climate mode SSTA index is indicated in the bottom axis. The XRO sensitivity experiments quantify how the initial states of ENSO affect the predictability of the other climate modes.

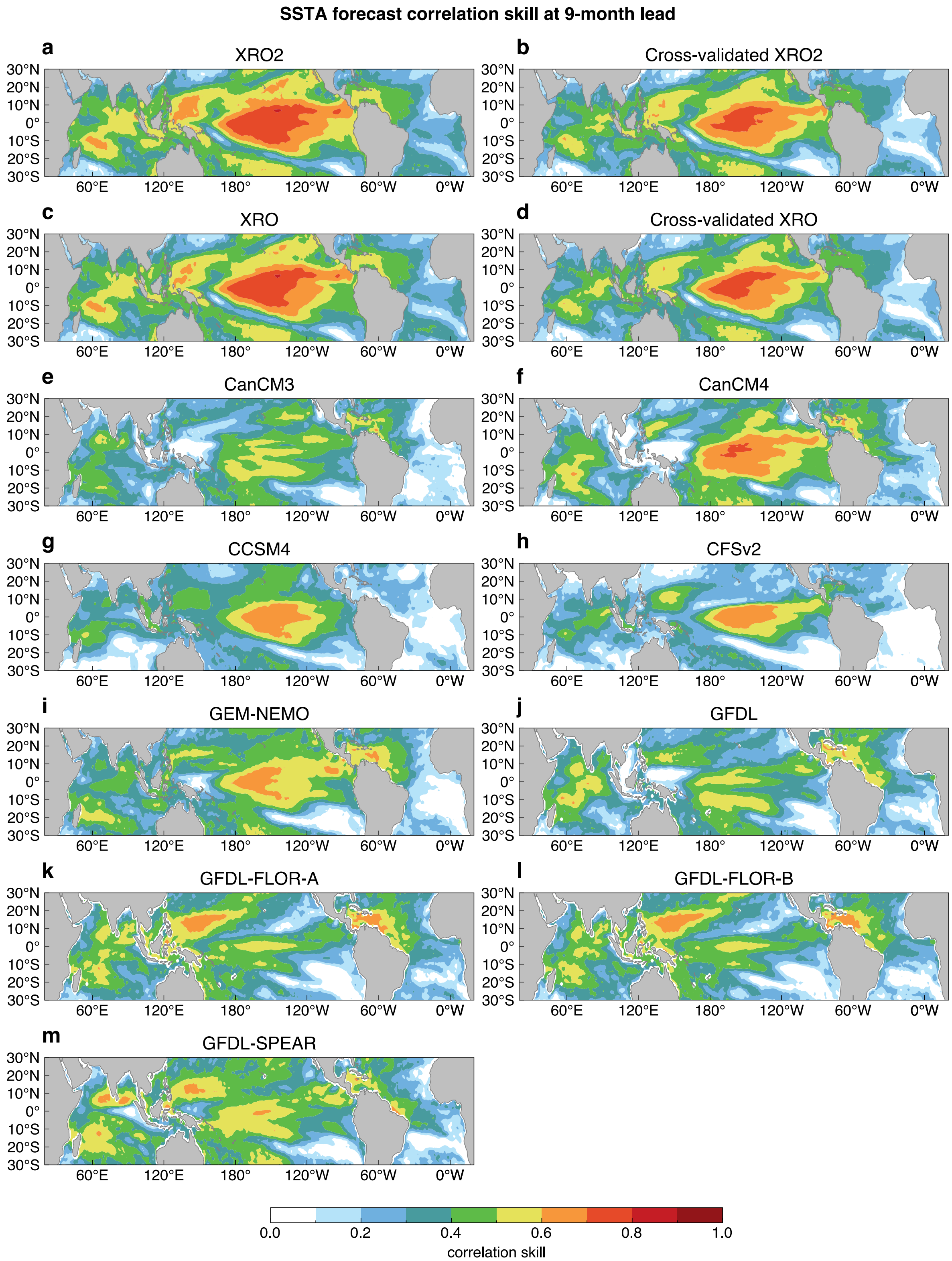
SSTA forecast correlation skill at 9-month lead
a
XRO2
b
Cross-validated XRO2
c
XRO
d
Cross-validated XRO
e
CanCM3
f
CanCM4
g
CCSM4
h
CFSv2
i
GEM-NEMO
j
GFDL
k
GFDL-FLOR-A
l
GFDL-FLOR-B
m
GFDL-SPEAR
30°N
20°N
10°N
0°
10°S
20°S
30°S
60°E
120°E
180°
120°W
60°W
0°W
0.0
0.2
0.4
0.6
0.8
1.0
correlation skill

(continued)

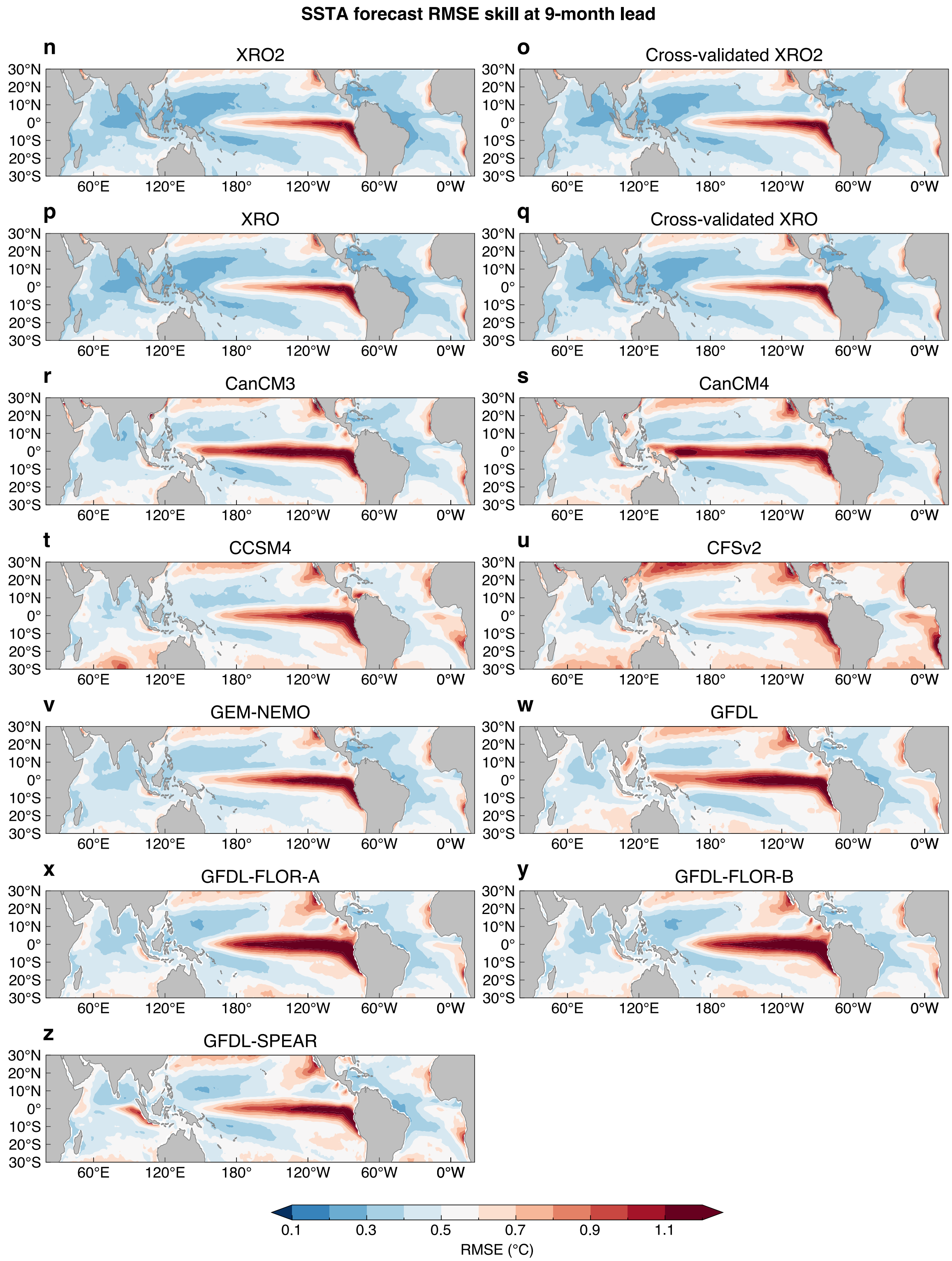

Supplementary Fig. 14| Pantropical SSTA forecast skill at 9-month lead time verified on 1982-2022. Correlation skill (**a-m**) and RMSE (**n-z**) for the SST forecasts include XRO2, cross-validated XRO2, XRO, cross-validated XRO, and the available nine NMME models. The XRO2 provide more skilful SSTA forecast than the operatorial climate models in most of the pantropical regions.

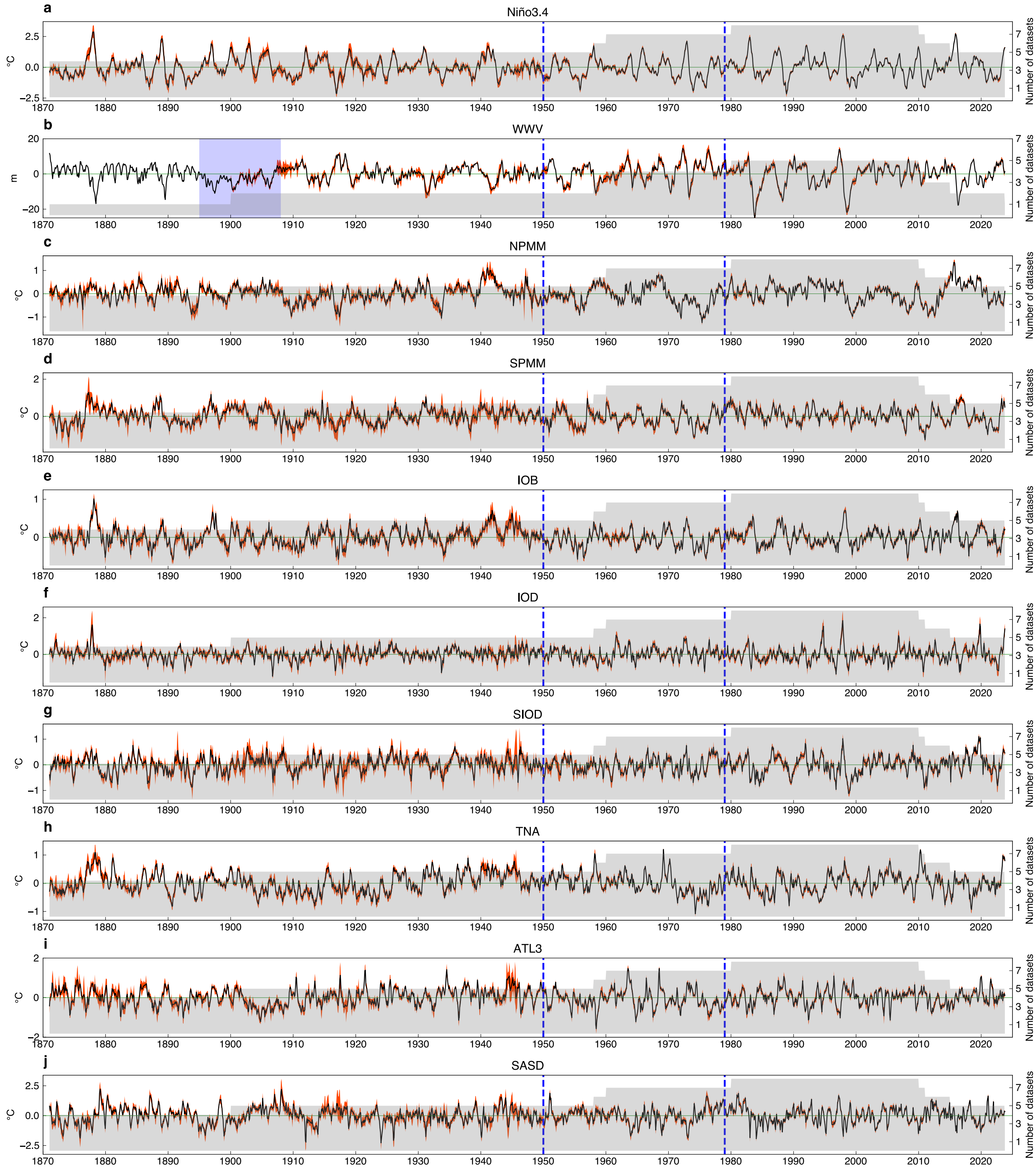

Supplementary Fig. 15| Time series of various SSTA indices and WWV anomaly index in multiple observation/reanalysis datasets. SST datasets include (HadISST: 1871-2023, ERSSTv5: 1871-2023, COBE-SST2: 1871-2023, ORAS5: 1958-2023, SODA224: 1871-2010, ORA20C: 1900-2009, PEODAS: 1960-2014, GECOO3: 1948-2018, GODAS: 1980-2023), WWV datasets include (ORAS5: 1958-2023, SODA224: 1871-2010, ORA20C: 1900-2009, PEODAS: 1960-2014, GECOO3: 1948-2018, GODAS:

1980-2023). The monthly anomalies were calculated by removing the monthly climatology for 1980-2010 and the quadratic trend over the whole period. The black curve is mean of all datasets, the red shading denotes the 10%-90% inter-dataset spread, the grey shading indicates the number of datasets calculated for each month, the blue vertical reference lines denote January of 1950 and 1979. There are large uncertainties in the data before 1950, especially for equatorial Pacific WWV and SSTA in other basins (large inter-dataset spread shown by red shadings), and during time of World War II (1936-1949). There are also periods that are not physically consistent with current theory or understanding of ENSO, for instance, the multiple El Niño events occurred when a long period of discharged WWV state during 1895-1908 (blue shading period, compare with the Nino34 SSTA and WWV anomaly).

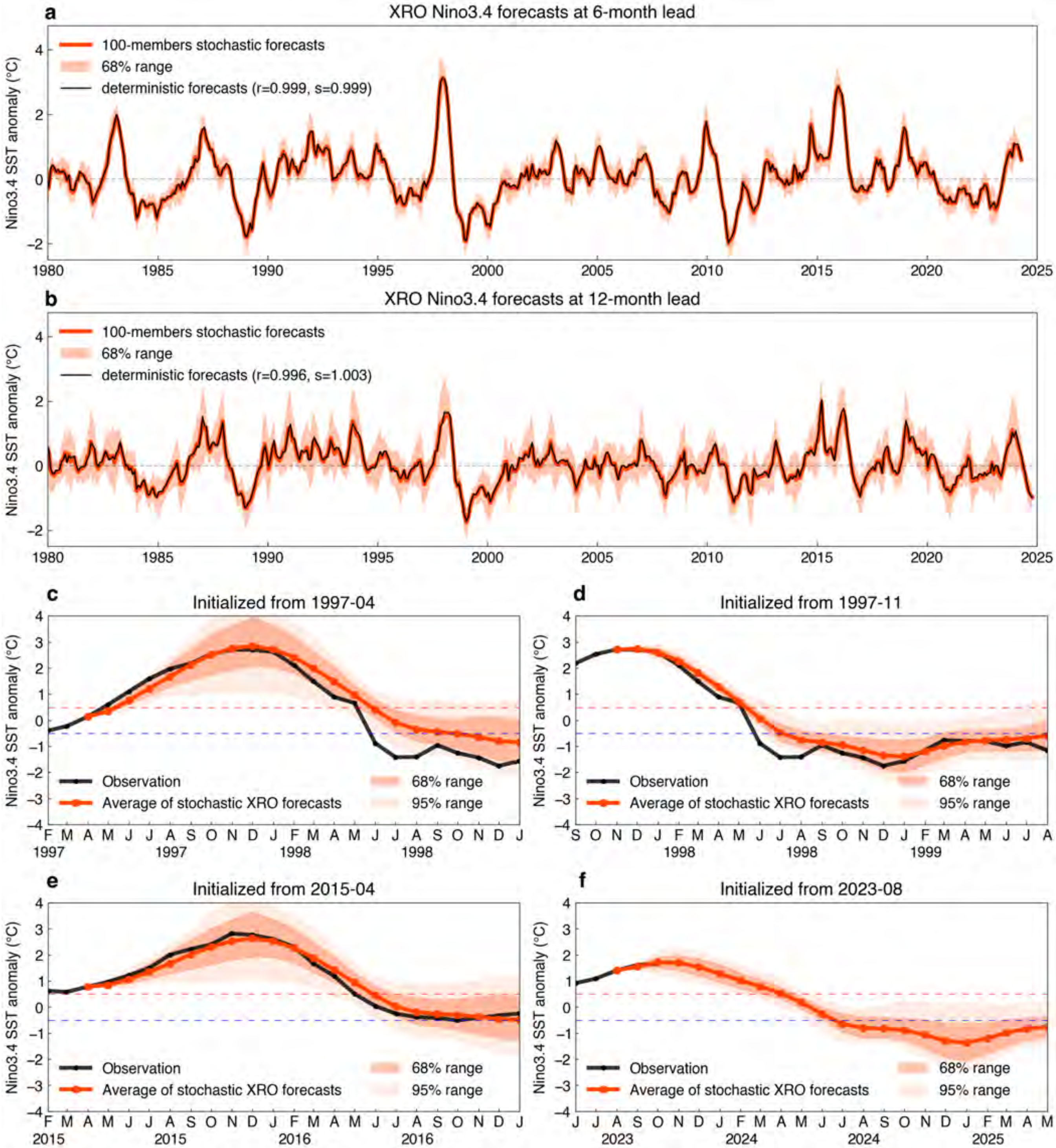

Supplementary Fig. 16| 100-member stochastic forecasts of ENSO by the XRO. a-b, Time series of XRO-forecasted Niño3.4 SSTA, at lead-times of (a) 6 months and (b) 12 months. Black curves correspond to a deterministic forecast, in which the stochastic forcing term is neglected during the integration. Forecasts from a 100-member stochastic XRO ensemble are shown in red (dark red for the ensemble mean, red shadings indicate the central 68% range of the ensemble members). The correlation and regression slope between the deterministic forecast and the stochastic ensemble mean are indicated in the corresponding legends. **c-f**, Niño3.4 SSTA forecasts initialized in (a) 1997 April, (b) 1997 November, (c) 2015 April, and (d) 2023 August. Red curves show the ensemble-mean XRO forecast; dark red envelope is the central 68% range of the ensemble members; lighter red is the central 95% range; black curves show the observations. The ensemble mean of the XRO stochastic forecasts is almost identical to the deterministic XRO forecast. The XRO stochastic forecasts provide an opportunity for probabilistic ENSO forecasts. The seasonality of the ENSO growth rate leads to a substantial spread in forecast outcomes from November to February. This inherent spread reflects a higher degree of uncertainty in predicting the peak amplitude of ENSO during this period. Conversely, from April to June, the forecast spread is narrower. However, this does not necessarily imply a better forecast skill, as the actual signal during this period is quite weak, resulting in a low signal-to-noise ratio.

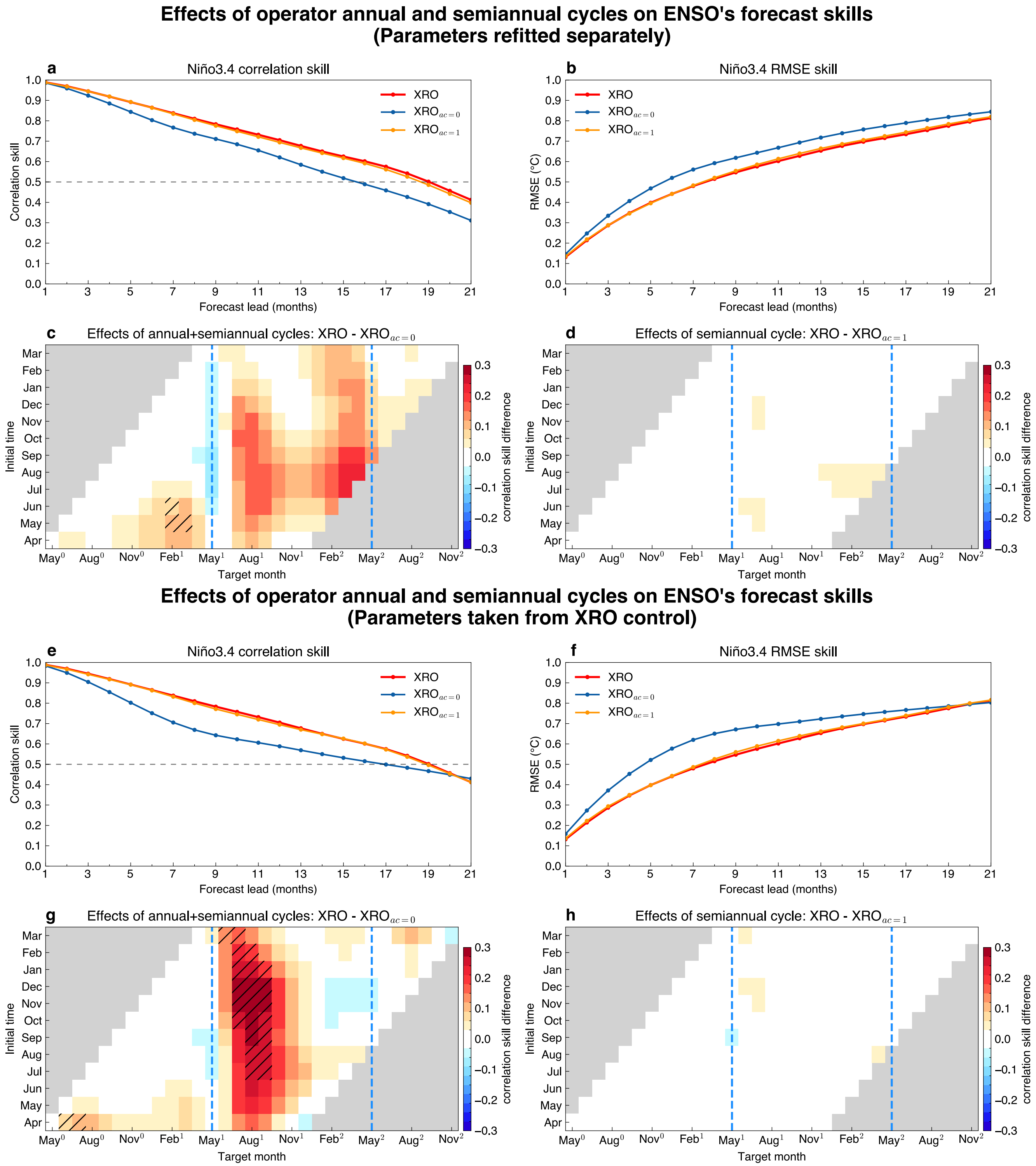

Supplementary Fig. 17| Effects of the XRO operator's annual and semiannual cycles on its ENSO forecast skill during 1979-2022. a-b, The all-months (a) correlation skill and (b) RMSE of the forecasted 3-month running mean Niño3.4 SSTA index, as a function of forecast lead, for the XRO in which the annual mean, annual cycle, and semiannual components are all considered in the linear and nonlinear parameters (*red*), XRO$_{ac=0}$ in which only the annual mean component is considered (*blue*), and XRO$_{ac=1}$

in which both the annual mean and annual cycle components are considered (*orange*). **c-d**, the skill difference of the Niño3.4 index, as a function of start month (ordinate) and target month (abscissa), between XRO and the deseasonalized experiments: (c) $XRO_{ac=0}$ and (d) $XRO_{ac=1}$. Hatching indicates that the correlation difference is significant at 90% confidence level using the two-tailed Fisher z-transformation test. The dashed vertical blue lines denote the spring predictability barrier (SPB) season. **a-d,** the parameters for $XRO_{ac=0}$ and $XRO_{ac=1}$ are refitted separately; **e-h**, same as **a-d**, but for $XRO_{ac=0}$ and $XRO_{ac=1}$ in which the parameters are taken from the XRO control experiment. The seasonal cycle is critically important for suppressing the SPB for ENSO, while the semi-annual cycle is less important.

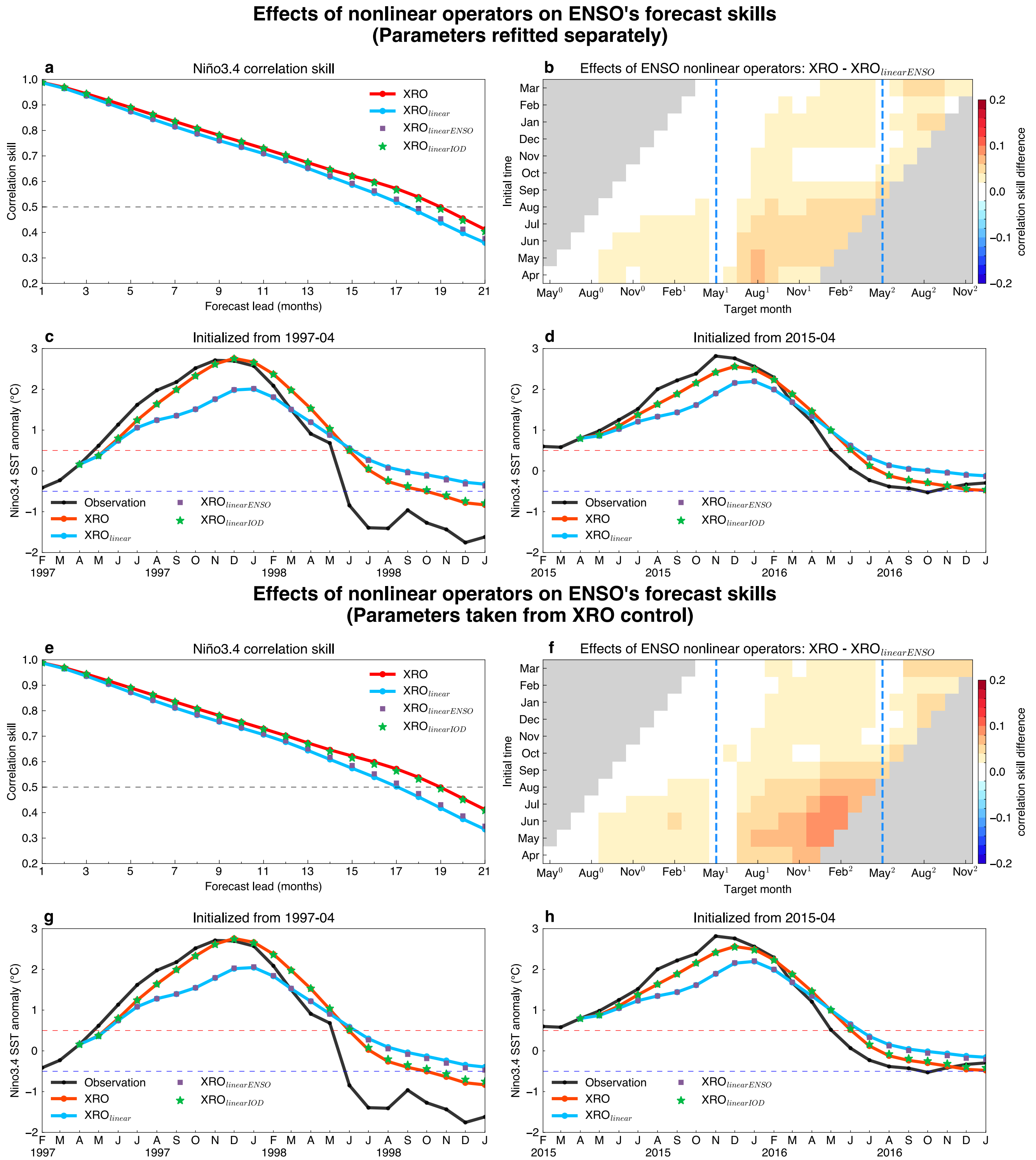

Supplementary Fig. 18| Effects of the XRO nonlinear operators on its ENSO forecast skill during 1979-2022. a, The all-months (a) correlation skill of the forecasted 3-month running mean Niño3.4 SSTA index, as a function of forecast lead for the XRO control (*red*), XRO$_{\mathrm{linear}}$ (*blue*), XRO$_{\mathrm{linearENSO}}$ (*purple square*), and XRO$_{\mathrm{linearIOD}}$ (*green star*s). **b**, the skill difference of the Niño3.4 index, as a function of start month (ordinate) and target month (abscissa), between XRO and XRO$_{\mathrm{linearENSO}}$. The dashed vertical blue lines denote the spring predictability barrier season. **c-d**, monthly Niño3.4 SSTA forecasts initialized in

(a) 1997 April and (b) 2015 April for the XRO control (*red*), XRO_{linear} (*blue*), $XRO_{linearENSO}$ (*purple square*), and $XRO_{linearIOD}$ (*green star*s); black curves show the observations. **a-d,** the parameters for XRO_{linear}, $XRO_{linearENSO}$, and $XRO_{linearIOD}$ are refitted separately; **e-h**, same as **a-d**, but for XRO_{linear}, $XRO_{linearENSO}$, and $XRO_{linearIOD}$ in which the parameters are taken from the XRO control experiment. The ENSO nonlinear dynamics are critically important for ENSO forecast skill, especially for forecasting the amplitude of the peak phase and fast transition from El Niño to La Niña. The impact of the IOD's nonlinearity on ENSO forecast skill is neglectable.

References in Supplementary Information

An, S.-I., and F.-F. Jin, 2004: Nonlinearity and Asymmetry of ENSO. *J. Climate*, **17**, 2399–2412, https://doi.org/10.1175/1520-0442(2004)017<2399:NAAOE>2.0.CO;2.

An, S.-I., E. Tziperman, Y. M. Okumura, and T. Li, 2020: ENSO Irregularity and Asymmetry. *El Niño Southern Oscillation in a Changing Climate*, American Geophysical Union (AGU), 153–172.

An, S.-I., H.-J. Park, S.-K. Kim, W. Cai, A. Santoso, D. Kim, and J.-S. Kug, 2023: Main drivers of Indian Ocean Dipole asymmetry revealed by a simple IOD model. *npj Clim Atmos Sci*, **6**, 1–7, https://doi.org/10.1038/s41612-023-00422-2.

Behringer, D., and Y. Xue, 2004: Evaluation of the global ocean data assimilation system at NCEP: The Pacific Ocean. *Eighth Symposium on Integrated Observing and Assimilation Systems for Atmosphere, Oceans, and Land Surface*, Vol. 2.3 of, AMS 84th Annual Meeting, Washington, 11–15.

de Boisséson, E., M. A. Balmaseda, and M. Mayer, 2018: Ocean heat content variability in an ensemble of twentieth century ocean reanalyses. *Clim Dyn*, **50**, 3783–3798, https://doi.org/10.1007/s00382-017-3845-0.

Carton, J. A., and B. S. Giese, 2008: A Reanalysis of Ocean Climate Using Simple Ocean Data Assimilation (SODA). *Mon. Wea. Rev.*, **136**, 2999–3017, https://doi.org/10.1175/2007MWR1978.1.

Chen, H.-C., and F.-F. Jin, 2021: Simulations of ENSO Phase-Locking in CMIP5 and CMIP6. *Journal of Climate*, **34**, 5135–5149, https://doi.org/10.1175/JCLI-D-20-0874.1.

Chen, H.-C., F.-F. Jin, and L. Jiang, 2021: The Phase-Locking of Tropical North Atlantic and the Contribution of ENSO. *Geophysical Research Letters*, **48**, e2021GL095610, https://doi.org/10.1029/2021GL095610.

Choi, K.-Y., G. A. Vecchi, and A. T. Wittenberg, 2013: ENSO Transition, Duration, and Amplitude Asymmetries: Role of the Nonlinear Wind Stress Coupling in a Conceptual Model. *J. Climate*, **26**, 9462–9476, https://doi.org/10.1175/jcli-d-13-00045.1.

DiNezio, P. N., and C. Deser, 2014: Nonlinear Controls on the Persistence of La Niña. *J. Climate*, **27**, 7335–7355, https://doi.org/10.1175/JCLI-D-14-00033.1.

Ding, R., Y.-H. Tseng, E. Di Lorenzo, L. Shi, J. Li, J.-Y. Yu, C. Wang, C. Sun, J.-J. Luo, K.-J. Ha, Z.-Z. Hu, and F. Li, 2022: Multi-year El Niño events tied to the North Pacific Oscillation. *Nat Commun*, **13**, 3871, https://doi.org/10.1038/s41467-022-31516-9.

Enfield, D. B., A. M. Mestas-Nuñez, D. A. Mayer, and L. Cid-Serrano, 1999: How ubiquitous is the dipole relationship in tropical Atlantic sea surface temperatures? *Journal of Geophysical Research: Oceans*, **104**, 7841–7848, https://doi.org/10.1029/1998JC900109.

Geng, T., W. Cai, and L. Wu, 2020: Two Types of ENSO Varying in Tandem Facilitated by Nonlinear Atmospheric Convection. *Geophysical Research Letters*, **47**, e2020GL088784, https://doi.org/10.1029/2020GL088784.

Geng, T., F. Jia, W. Cai, L. Wu, B. Gan, Z. Jing, S. Li, and M. J. McPhaden, 2023: Increased occurrences of consecutive La Niña events under global warming. *Nature*, **619**, 774–781, https://doi.org/10.1038/s41586-023-06236-9.

Hersbach, H., B. Bell, P. Berrisford, S. Hirahara, A. Horányi, J. Muñoz-Sabater, J. Nicolas, C. Peubey, R. Radu, D. Schepers, A. Simmons, C. Soci, S. Abdalla, X. Abellan, G. Balsamo, P. Bechtold, G. Biavati, J. Bidlot, M. Bonavita, G. De Chiara, P. Dahlgren, D. Dee, M. Diamantakis, R. Dragani, J. Flemming, R. Forbes, M. Fuentes, A. Geer, L. Haimberger, S. Healy, R. J. Hogan, E. Hólm, M. Janisková, S. Keeley, P. Laloyaux, P. Lopez, C. Lupu, G. Radnoti, P. de Rosnay, I. Rozum, F. Vamborg, S. Villaume, and J.-N. Thépaut, 2020: The ERA5 global reanalysis. *Quarterly Journal of the Royal Meteorological Society*, **146**, 1999–2049, https://doi.org/10.1002/qj.3803.

Hirahara, S., M. Ishii, and Y. Fukuda, 2014: Centennial-Scale Sea Surface Temperature Analysis and Its Uncertainty. *Journal of Climate*, **27**, 57–75, https://doi.org/10.1175/JCLI-D-12-00837.1.

Huang, B., P. W. Thorne, V. F. Banzon, T. Boyer, G. Chepurin, J. H. Lawrimore, M. J. Menne, T. M. Smith, R. S. Vose, and H.-M. Zhang, 2017: Extended Reconstructed Sea Surface Temperature, Version 5 (ERSSTv5): Upgrades, Validations, and Intercomparisons. *Journal of Climate*, **30**, 8179–8205, https://doi.org/10.1175/JCLI-D-16-0836.1.

Iwakiri, T., and M. Watanabe, 2021: Mechanisms linking multi-year La Niña with preceding strong El Niño. *Sci Rep*, **11**, 17465, https://doi.org/10.1038/s41598-021-96056-6.

Iwakiri, T., and M. Watanabe, 2022: Multiyear ENSO Dynamics as Revealed in Observations, Climate Model Simulations, and the Linear Recharge Oscillator. *Journal of Climate*, **35**, 7625–7642, https://doi.org/10.1175/JCLI-D-22-0108.1.

Jeong, H., H.-S. Park, M. F. Stuecker, and S.-W. Yeh, 2022: Distinct impacts of major El Niño events on Arctic temperatures due to differences in eastern tropical Pacific sea surface temperatures. *Science Advances*, **8**, eabl8278, https://doi.org/10.1126/sciadv.abl8278.

Jiang, F., W. Zhang, F.-F. Jin, M. F. Stuecker, A. Timmermann, M. J. McPhaden, J. Boucharel, and A. T. Wittenberg, 2023: Resolving the Tropical Pacific/Atlantic Interaction Conundrum. *Geophysical Research Letters*, **50**, e2023GL103777, https://doi.org/10.1029/2023GL103777.

Jo, H.-S., Y.-G. Ham, J.-S. Kug, T. Li, J.-H. Kim, J.-G. Kim, and H. Kim, 2022: Southern Indian Ocean Dipole as a trigger for Central Pacific El Niño since the 2000s. *Nat Commun*, **13**, 6965, https://doi.org/10.1038/s41467-022-34721-8.

Kang, I.-S., and J.-S. Kug, 2002: El Niño and La Niña sea surface temperature anomalies: Asymmetry characteristics associated with their wind stress anomalies. *Journal of Geophysical Research: Atmospheres*, **107**, ACL 1-1-ACL 1-10, https://doi.org/10.1029/2001JD000393.

Kim, J.-W., and J.-Y. Yu, 2022: Single- and multi-year ENSO events controlled by pantropical climate interactions. *npj Clim Atmos Sci*, **5**, 1–11, https://doi.org/10.1038/s41612-022-00305-y.

Kim, J.-W., J.-Y. Yu, and B. Tian, 2023: Overemphasized role of preceding strong El Niño in generating multi-year La Niña events. *Nat Commun*, **14**, 6790, https://doi.org/10.1038/s41467-023-42373-5.

Köhl, A., 2020: Evaluating the GECCO3 1948–2018 ocean synthesis – a configuration for initializing the MPI-ESM climate model. *Quarterly Journal of the Royal Meteorological Society*, **146**, 2250–2273, https://doi.org/10.1002/qj.3790.

Levine, A. F. Z., and M. J. McPhaden, 2015: The annual cycle in ENSO growth rate as a cause of the spring predictability barrier. *Geophysical Research Letters*, **42**, 5034–5041, https://doi.org/10.1002/2015GL064309.

Nnamchi, H. C., J. Li, F. Kucharski, I.-S. Kang, N. S. Keenlyside, P. Chang, and R. Farneti, 2015: Thermodynamic controls of the Atlantic Niño. *Nature Communications*, **6**, 8895, https://doi.org/10.1038/ncomms9895.

Okumura, Y. M., M. Ohba, C. Deser, and H. Ueda, 2011: A Proposed Mechanism for the Asymmetric Duration of El Niño and La Niña. *Journal of Climate*, **24**, 3822–3829, https://doi.org/10.1175/2011JCLI3999.1.

Park, J.-H., S.-I. An, J.-S. Kug, Y.-M. Yang, T. Li, and H.-S. Jo, 2021: Mid-latitude leading double-dip La Niña. *International Journal of Climatology*, **41**, E1353–E1370, https://doi.org/10.1002/joc.6772.

Rayner, N. A., D. E. Parker, E. B. Horton, C. K. Folland, L. V. Alexander, D. P. Rowell, E. C. Kent, and A. Kaplan, 2003: Global analyses of sea surface temperature, sea ice, and night marine air temperature since the late nineteenth century. *Journal of Geophysical Research: Atmospheres*, **108**, https://doi.org/10.1029/2002JD002670.

Richter, I., M. F. Stuecker, N. Takahashi, and N. Schneider, 2022: Disentangling the North Pacific Meridional Mode from tropical Pacific variability. *npj Clim Atmos Sci*, **5**, 1–9, https://doi.org/10.1038/s41612-022-00317-8.

Rodrigues, R. R., E. J. D. Campos, and R. Haarsma, 2015: The Impact of ENSO on the South Atlantic Subtropical Dipole Mode. *Journal of Climate*, **28**, 2691–2705, https://doi.org/10.1175/JCLI-D-14-00483.1.

Saji, N. H., B. N. Goswami, P. N. Vinayachandran, and T. Yamagata, 1999: A dipole mode in the tropical Indian Ocean. *Nature*, **401**, 360–363, https://doi.org/10.1038/43855.

Stein, K., A. Timmermann, N. Schneider, F.-F. Jin, and M. F. Stuecker, 2014: ENSO Seasonal Synchronization Theory. *J. Climate*, **27**, 5285–5310, https://doi.org/10.1175/JCLI-D-13-00525.1.

Trenberth, K. E., 1997: The Definition of El Niño. *Bulletin of the American Meteorological Society*, **78**, 2771–2778, https://doi.org/10.1175/1520-0477(1997)078<2771:TDOENO>2.0.CO;2.

Xie, P. P., and P. A. Arkin, 1997: Global precipitation: A 17-year monthly analysis based on gauge observations, satellite estimates, and numerical model outputs. *Bull. Amer. Meteor. Soc.*, **78**, 2539–2558, https://doi.org/10.1175/1520-0477(1997)078<2539:Gpayma>2.0.Co;2.

Xie, S.-P., K. M. Hu, J. Hafner, H. Tokinaga, Y. Du, G. Huang, and T. Sampe, 2009: Indian Ocean capacitor effect on Indo-Western Pacific climate during the summer following El Niño. *J. Climate*, **22**, 730–747, https://doi.org/10.1175/2008jcli2544.1.

Yin, Y., O. Alves, and P. R. Oke, 2011: An Ensemble Ocean Data Assimilation System for Seasonal Prediction. *Mon. Wea. Rev.*, **139**, 786–808, https://doi.org/10.1175/2010MWR3419.1.

Zhang, H., A. Clement, and P. D. Nezio, 2014: The South Pacific Meridional Mode: A Mechanism for ENSO-like Variability. *Journal of Climate*, **27**, 769–783, https://doi.org/10.1175/JCLI-D-13-00082.1.

Zhao, S., F.-F. Jin, and M. F. Stuecker, 2021: Understanding Lead Times of Warm Water Volumes to ENSO Sea Surface Temperature Anomalies. *Geophysical Research Letters*, **48**, e2021GL094366, https://doi.org/10.1029/2021GL094366.

Zuo, H., M. A. Balmaseda, S. Tietsche, K. Mogensen, and M. Mayer, 2019: The ECMWF operational ensemble reanalysis–analysis system for ocean and sea ice: a description of the system and assessment. *Ocean Science*, **15**, 779–808, https://doi.org/10.5194/os-15-779-2019.